Title
Extending Time-Resolved Photoelectron Spectroscopy to the Extreme Ultraviolet

Author
Erickson, Blake Alexander

Publication Date
2021

Peer reviewed|Thesis/dissertation

Extending Time-Resolved Photoelectron Spectroscopy to the Extreme Ultraviolet

by

Blake Alexander Erickson

A dissertation submitted in partial satisfaction of the

requirements for the degree of

Doctor of Philosophy

in

Chemistry

in the

Graduate Division

of the

University of California, Berkeley

Committee in charge:

Professor Daniel M. Neumark, Chair
Professor Ronald C. Cohen
Professor Roger W. Falcone

Fall 2021

Extending Time-Resolved Photoelectron Spectroscopy to the Extreme Ultraviolet

Abstract

Extending Time-Resolved Photoelectron Spectroscopy to the Extreme Ultraviolet

by

Blake Alexander Erickson

Doctor of Philosophy in Chemistry

University of California, Berkeley

Professor Daniel M. Neumark, Chair

The interaction of ultraviolet (UV) light with cellular media is a problem of fundamental interest in a wide variety of fields. Specifically, this thesis focuses on the elucidation of the electronic dynamics of nucleobases (NBs), the building blocks of DNA, after they have absorbed UV light. Understanding the different photochemical and photophysical pathways that lead to DNA damage, and those that prevent it, is the primary focus of this thesis work. These processes are monitored via time-resolved photoelectron spectroscopy (TRPES) applied to a water microjet. In these experiments, a UV pump pulse is used to excite valence electrons in the NBs, and a time-delayed probe pulse is used to photoionize the excited species. The arrival time of the ejected electrons is detected by a magnetic bottle time-of-flight spectrometer. By varying the time delay between the pump and probe pulse the electronic dynamics occurring on the excited state surface(s) are mapped out.

The NB thymine (T) and its derivatives thymidine (Thd) and thymidine-5'-monophosphate (TMP) are studied by TRPES using two UV pulses, one tuned over 4.74 – 5.17 eV and the other at 6.2 eV. The tunable UV pulse excites valence electrons into the lowest lying $\pi\pi^*$ state which is found to decay back into the ground state in $\sim$400 fs in both T and Thd independent of pump photon energy, and in 670 – 840 fs in TMP with a small amount of pump energy dependence. The longer lifetime of TMP compared to T and Thd is found to be a result of the conformational differences between the molecules in solution by QM/MM calculations done at the XMS-CASPT2//CASSCF/AMBER level. Notably, no signal in any of the three molecules is found to persist for longer than a few ps, contradicting previous experiments that claimed a portion of the initially excited electron population is trapped in an intermediate state for tens of ps before decaying. When using the 6.2 eV pulse as the pump pulse, a band of multiple $\pi\pi^*$ states is populated and found to decay into the lowest lying $\pi\pi^*$ state within the cross correlation of our laser pulses before decaying back into the ground state.

A major drawback of the previous study is the relatively low energy of the probe pulse. While photoionization signal is observed from the excited $\pi\pi^*$ states, no signal is observed from the ground state as it is bound in excess of the probe photon energy. To remedy this problem a new light source was designed and built to generate probe photons in the XUV regime with sufficient energy to ionize both the ground and any excited states in these molecules. XUV pulses are generated at 21.7 eV with very high flux (up to 100 nJ/pulse). This XUV light has been applied to a wide variety of gaseous, liquid, and solvated species as discussed in Chapter 4 of this thesis. The laser-assisted photoelectric effect (LAPE) has been utilized to characterize the temporal profile of the XUV beam. This new source is now being applied to NBs, and a variety of other systems, to further elucidate the dynamics described above and to explore other ultrafast phenomena in solution.

To Alyssa

Contents

List of Figures

List of Tables

Acknowledgments

The words on the following pages are grossly insufficient in describing my intense gratitude to the people who made this work possible. Each of you have been indispensable in the completion of my PhD, either academically, socially, or most commonly, a combination of the two. I appreciate every one of you.

First, I want to acknowledge my advisor Dan Neumark. Your scientific rigor is unmatched by anyone I've met. You taught me to hold high standards for myself and my work. You also possessed the insight to understand when I needed support and guidance and when I needed to figure things out on my own. I am forever grateful to you for taking me on as your student these past years.

There are so many staff members who provided support through the years. Michelle Haskins, thank you for making my administrative problems disappear; you've saved me countless hours of work. The group dearly misses you. To Doug Scudder and Clint Jessel at the machine shop, thank you for your excellent work helping me design and build our instrument. I hope you enjoy your well-earned retirement in the next few years. Thank you to Doug Kresse and Brian Molesky at Coherent for keeping my laser running nearly flawlessly the past 4 years. Having a reliable laser has allowed me to dedicate more time to actually doing science. Thank you to all of the janitorial, HVAC, and other support staff who I didn't get the privilege of knowing personally, but who kept everything running behind the scenes.

I have had the immense privilege of working alongside many great scientists during graduate school. Holly Williams was one of my first scientific mentors. I can never thank you enough for tolerating my sass the first couple of years of grad school (not that you had much choice). I learned so much from you on how to run a research project, set realistic goals, and hold myself accountable for progress (or lack thereof, at times).

Zachary Heim has been my partner in crime for most of graduate school. Thank you for sharing with me both the immense joy and frustration, probably not in that order, that are a part of research. You taught me to make science fun, whether it be doing side projects that frequently involve electrocuting yourself, blasting music so loud that we get complaints from our lame neighbors (SEVI), or knowing when to step away from lab and grab a beer. I've been incredibly lucky to call you my colleague and my friend.

I have also had the opportunity to mentor two undergraduate students during my time here, Erica Liu and Negar Baradaran. Thank you both for your help in lab. Erica, thank you for being a morning person so I didn't have to be. Your bright mind and attention to detail were a great help to the project. Negar, you're quickly becoming an incredible scientist. You are extremely sharp and perceptive, and I can't wait to see where the next few years take you.

Finally, best of luck to our newest member of LPES – Leonardo Coello. It's nice to leave Berkeley knowing the lab will be in good hands.

Thank you to everyone who helped me during my build. It was a huge and overwhelming process that was made achievable thanks to your guidance. In no particular order: Hugo Marroux, Lou Barreau, Romain Géneaux, Andrew Attar, Kristina Chang, Ilana Porter, and Andrew Ross.

I would also like to thank all of the Neumark group members who shared the Latimer D-level with me. I could always count on you guys for a coffee break, an extra set of hands in lab, or giving me a second opinion. Special thanks to Isaac Ramphal for being one of the zaniest people I've ever met, Chin Lee for always being such a kind presence in our group, and Steve Saric for teaching me how to take my homebrew to the next level.

While I did spend a lot of time in the dungeons of Latimer Hall, when I could escape work I was always surrounded by my friends. Eugene, thank you for being my first friend in Berkeley, my video game duo, and for helping me land a job. I'm super excited to be your neighbor up in Portland. Chuck, thank you for always being down to go to literally any concert with me. Screaming our lungs out to mid-2000's pop-punk music was always a blast. Mark, thank you for experiencing every part of grad school alongside me. From struggling through quals and attending conferences in the both the highest and lowest quality beach towns this country has to offer, each step of the way was made better with you by my side.

Lou and Romain, thank you for being both incredibly good at what you do and being so down to earth. You are some of the kindest people I've ever met and I sincerely hope our paths cross again soon. Katherine, thank you for being such a supportive friend, especially in our first year of grad school. I'm not sure I would have survived it without you. Nathan, thank you for including me in your board game night many years ago. Sunday night board games were frequently a much needed bright spot in otherwise tough weeks. Carlos, thank you for always being such an uplifting presence. Your optimism is contagious and you never fail to make me laugh.

Thank you to my pets, Florence and Margaret, for being incredibly grounding. Having responsibilities and routine outside of lab was crucial to my success.

Next, I want to thank my parents. From a young age you've instilled a standard of excellence in me. You loved and supported me in everything I did, whether I was good at it or not. You taught me that hard work beats talent and that I could do anything I set my mind to. Mom, I specifically want to thank you for teaching me how to approach everything I do with kindness. No matter where life takes me, I am guided by this. Dad, thank you for teaching me to have a never-ending curiosity of the world around me. The world is truly a beautiful place if you take the time to appreciate it.

Thank you to the rest of my family. There are so many people who have supported me these past 6 years, so I can't thank you all individually. I want to specifically thank my sisters: Carley, Alisa, Alexis, and Alayna. You have all had such a tremendous impact on my life, and I love you all.

Finally, I want to thank my fiancée, Alyssa. There are no words to express how much I appreciate you. Despite the cliché, I really don't think I would have made it through graduate school without you. Thank you for being there to celebrate my successes and support me after my failures. You've seen me at my highest highs and lowest lows and loved me through it all. I can't wait to marry you and show you how much I appreciate you every day for the rest of our lives.

Chapter 1

Introduction

1.1 Overview

The interaction of ultraviolet (UV) radiation with cellular media is a problem of significant interest due to the potential formation of genotoxic photoproducts [1–7]. This interest is highly interdisciplinary, having implications in photobiology, fundamental physical chemistry, and even evolutionary sciences. A full mapping of the various deactivation pathways, as well as the pathways leading to bond breakage/formation, is desired to fully explain this phenomenon. The interaction of UV radiation with DNA is known to be carcinogenic, however the mechanism of this damage is not fully understood. For example, the most common photoproduct, pyrimidine dimerization, can happen up to 50 – 100 times per second in a skin cell and is the primary cause of melanoma, the most dangerous type of skin cancer [8]. Understanding the pathways that lead to this damage, as well as those that prevent it, are crucial in fully unraveling the physics occurring in our cells.

Extensive work has been done to explore these processes in isolated gas-phase molecules [3, 9–11], but surrounding water molecules are found to have a significant impact on these processes in both static and time-resolved experiments [2, 4, 12]. It is thus necessary to study these systems in solution to fully understand the processes involved. DNA is incredibly complicated, so a bottom-up approach has been taken to reduce the complexity of the problem by starting with single subunits of DNA: nucleic acid constituents (NACs). From this foundation, additional subunits can then be added to increase the resemblance to polymeric DNA.

To increase the wealth of information extracted from these experiments an extreme ultraviolet (XUV) light source was constructed. This higher energy light allows the detection of all of the states that are involved in these dynamic processes that occur after photoexcitation. This will be discussed more in the chapters that follow.

The remainder of this chapter provides the principles of the experiment and a brief

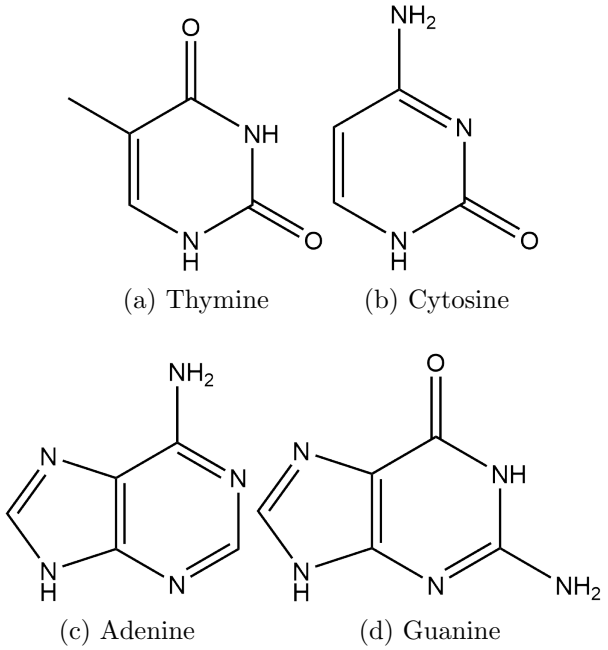

(a) Thymine (b) Cytosine

(c) Adenine (d) Guanine

Figure 1.1: The chemical structure of the four DNA nucleobases. a-b) pyrimidines and c-d) purines.

overview of the techniques that are used. Chapter 2 describes the experimental apparatus: the liquid microjet, the photoelectron spectrometer, and the beamline. In Chapter 3, the deactivation pathways of thymine, thymidine, and thymidine-5'-monophosphate (TMP) are explored subsequent to UV irradiation. Finally, the progress in coupling an XUV light source to the experiment is outlined and planned future experiments are presented in Chapter 4.

1.2 DNA Photochemistry

DNA is a double stranded helix composed of nucleobases (NBs) which are connected together via a sugar-phosphate backbone. The NBs are where the information is stored in DNA, providing a blueprint for the production of proteins. The four DNA NBs are shown in Figure 1.1, note that uracil is omitted because it is only present in RNA. Each NB has a complementary base pair, adenine with thymine and cytosine with guanine, which allows them to hydrogen bond. This hydrogen bonding links two single-stranded DNA molecules and turns them into one double stranded helix.

The NBs are all very efficient at absorbing light in the UV with strong absorption bands

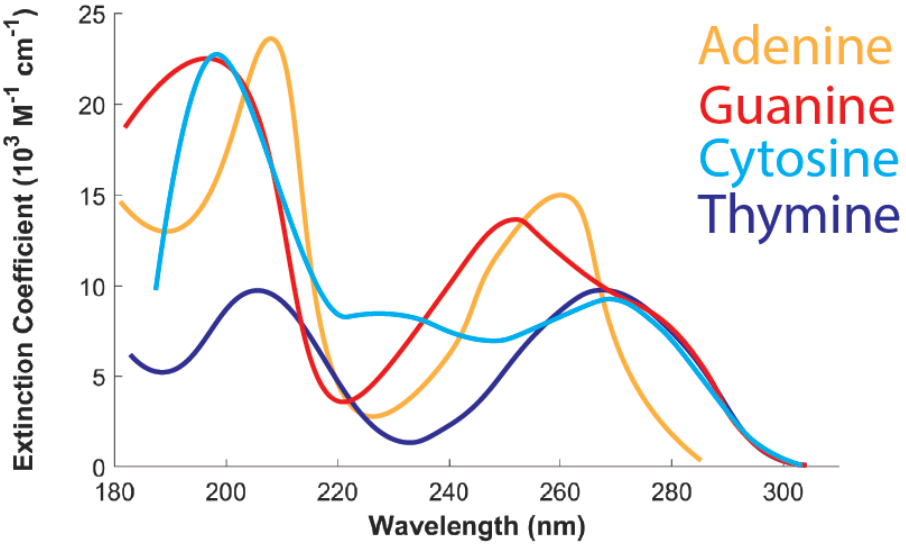

Figure 1.2: Absorption curve for the four DNA nucleobases in the ultraviolet. The absorption features shown at ∼260 nm were taken from References [1, 4, 13, 14] and features at ∼200 nm were taken from References [13, 14].

located at around 260 nm and 200 nm [1, 4, 13, 14]. The UV absorption spectrum of the NBs is shown in Figure 1.2. The absorption peaking at 240-260 nm is attributed to a $S_0 \rightarrow \pi\pi^*$ transition. After electronic excitation there are various deactivation processes that can occur, and in some cases these pathways can lead to genotoxic species [1]. Thankfully, the potential energy surfaces allow a very efficient transfer of energy from the excited state back into the ground state through a series of conical intersections (CIs) [3, 15–21]. A description of these CIs is covered later in this chapter, but it is important to understand that these processes occur non-radiatively and on ultrafast timescales making them difficult to study. The photostability of NBs is thought to be a key factor in why these molecules are used in genetic material. Due to the high levels of UV light in the early biotic periods on earth, resistance to damage from UV light was likely a significant source of evolutionary pressure [22].

Various other excited states have been implicated in the relaxation processes of both gaseous and hydrated NBs including optically dark $n\pi^*$, $^3\pi\pi^*$, and $\pi\sigma^*$ states.[1] These states tend to be longer lived than the $\pi\pi^*$ due to trapping in potential energy wells. The $\pi\pi^*$ states, on the other hand, are all relatively flat, allowing rapid propagation of the electron wavepacket towards CIs.

[1]Note that "$\pi\pi^*$" and "$n\pi^*$" are used in place of "$^1\pi\pi^*$" and "$^1n\pi^*$" for brevity. If not explicitly stated, any states without a designator can be assumed to be singlets.

1.3 Principles of Photoelectron Spectroscopy

If a photon of high enough energy interacts with a molecule, it can eject an electron. This can only occur if the energy of the photon is in excess of the energy that binds the electron[2]. The electron is then ejected with kinetic energy to satisfy the following equation:

$$eKE = h\nu - eBE \tag{1.1}$$

where eKE is the kinetic energy of the photoejected electron, $h\nu$ is the energy of the photon, and eBE is the binding energy of the electron before photoejection.

By controlling the photon energy experimentally and measuring the kinetic energy of the ejected electrons, the binding energy of the electron prior to ejection can be determined. Electrons in different states can then be distinguished by their unique binding energies given sufficient energy resolution. This allows for the exploration of the electronic structure of molecules at the time of ionization.

The selection rules for photoelectron spectroscopy are explained below. We first start by assuming the Born-Oppenheimer approximation [23–25]. This assumes that during a vibronic transition the nuclei are fixed, allowing the separability of the electronic and vibrational wavefunctions for the molecule which we can write as

$$|\Psi\rangle = |\psi_{elec}\rangle\,|\psi_{nuc}\rangle \tag{1.2}$$

where $|\Psi\rangle$ is the total wavefunction, $|\psi_e\rangle$ is the electronic wavefunction, and $|\psi_n\rangle$ is the nuclear wavefunction. Treating the light field as a perturbation to the system, we can write the Hamiltonian using first-order perturbation theory as

$$\hat{H} = \hat{H}^{(0)} + \hat{H}^{(1)}(t) \tag{1.3}$$

and the time-dependent electric field as

[2]This is true assuming that this occurs through a one photon process

$$\mathbf{E}(t) = \mathbf{E_0} cos(\omega t) \tag{1.4}$$

where $\mathbf{E_0}$ is the electric field vector, ω is the angular frequency of the light used, and t is time. Using the electric dipole approximation allows us to ignore higher order interactions and we can write the interaction of this field with the electric dipole moment of the molecule, $\boldsymbol{\mu}$, as the following perturbation Hamiltonian

$$\hat{H}^{(1)}(t) = -\boldsymbol{\mu} \cdot \mathbf{E_0} cos(\omega t) \tag{1.5}$$

We can then write a transition from an initial state, $|\Psi_i\rangle$, to a final state, $|\Psi_f\rangle$ as

$$\langle \Psi_f | \, \hat{H}^{(1)}(t) \, | \Psi_i \rangle \propto \langle \Psi_f | \, \boldsymbol{\mu} \cdot \mathbf{E}(t) \, | \Psi_i \rangle \tag{1.6}$$

Under the Born-Oppenheimer approximation, we can separate the electronic and nuclear wavefunctions as shown above.

$$\langle \psi_{f,elec} | \, \langle \psi_{f,nuc} | \, \boldsymbol{\mu} \cdot \mathbf{E}(t) \, | \psi_{i,elec} \rangle \, | \psi_{i,nuc} \rangle \tag{1.7}$$

Using Fermi's Golden Rule and skipping a few steps of simplification, we can then approximate the transition rate from the initial state to the final state as

$$\Gamma_{i \rightarrow f} \propto | \, \langle k, \psi_{f,elec} | \, \boldsymbol{\mu_e} \, | \psi_{i,elec} \rangle \, \langle \psi_{f,nuc} | \psi_{i,nuc} \rangle \, |^2 \tag{1.8}$$

where $|k\rangle$ is the wavefunction for the ejected electron and can be described as a free particle in a momentum eigenstate with momentum $\hbar k$. The first term of this equation represents the orbital overlap selection rule. In a bound-bound transition this rule expresses that the initial and final states of the molecule must have opposite parity. More generally, the representation of the product $\langle \psi_{f,elec} | \, \boldsymbol{\mu_e} \, | \psi_{i,elec} \rangle$ has to contain the totally symmetric representation of the symmetry group of the molecule. However, the final state in photoionization also includes the ejected electron which can leave the molecule with a wavefunction of any parity, so this

condition is not usually relevant in photoionization. There can also be final states that have multiple unbound photoelectrons, however these are rare in our experiments and are ignored.

The Franck-Condon factor, $|\langle\psi_{f,nuc}|\psi_{i,nuc}\rangle|^2$, is the square of the amplitude of the second term in Equation 1.8 [26, 27]. In essence, this is a geometric overlap consideration. If there is no overlap between the nuclear wavefunctions of the two states, then no transition will occur. Additionally, the intensity of a given transition is weighted by how much overlap there is between the two states.

There is one final selection rule that motivates a large portion of this thesis. The energy of the photon used must exceed the energy difference between the initial and final states, under the assumption of a one photon process. If the energy is insufficient, then no ionization will occur and there will be no signal, at least in the perturbative regime where multi-photon effects can be ignored.

1.4 Time-Resolved Photoelectron Spectroscopy

One color photoelectron spectroscopy is a powerful technique in studying equilibrium states in molecular systems, but a lot of chemistry happens in systems out of equilibrium [28]. Using the principles of photoelectron spectroscopy described above, we can now develop a framework for adding time-dependence. First, a qualitative understanding of how these experiments are performed will be presented followed by a theoretical description.

While many energy regimes and timescales have chemical relevance, this thesis focuses on dynamics subsequent to electronic excitation occurring on the 10s of fs to multiple ps timescale. Briefly, a pump photon interacts with the molecule of interest causing an electronic excitation. A probe photon then interacts with the molecule ejecting an electron into vacuum, leaving behind a cationic species according to the selection rules described in the previous section. By varying the time between when the pump and probe pulses interact with the molecule, accomplished by simply changing their relative pathlengths using a delay stage, spectra can be obtained at different points along the process. Given sufficient energy and time resolution, the entire photochemical pathway can be observed allowing the quantitative extraction of the energetics and timescales of the process [28–33].

While a rigorous theoretical treatment of TRPES is not necessary for understanding this work, a brief outline is presented below. For a rigorous treatment of this process, see Reference [34]. Consider a three-state system with an initial state, $|i\rangle$, intermediate state, $|j\rangle$, and final state, $|f\rangle$. Assume that the pump photon couples $|i\rangle$ to $|j\rangle$ irreversibly and the probe photon couples $|j\rangle$ to $|f\rangle$ in the same manner. Also assume that $|i\rangle$ cannot couple directly

to $|f\rangle$ without going through an intermediate state.

We start with the time-dependent Schrodinger equation

$$i\hbar\frac{\partial}{\partial t}|\Psi(t)\rangle = \hat{H}|\Psi(t)\rangle \tag{1.9}$$

where $|\Psi(t)\rangle$ can be expanded into its eigenstates, $|n\rangle$, as

$$|\Psi(t)\rangle = \sum_n c_n(t)|n\rangle \tag{1.10}$$

By using second order time-dependent perturbation theory, we can calculate the time-dependent coefficients as

$$\begin{aligned} c_n(t) = \delta_{if} &- \frac{1}{i\hbar}\int_0^t dt' \langle f| H'(t')_{pump} |i\rangle e^{i\omega_{fi}t'} \\ &- \frac{1}{\hbar^2}\int_0^t \int_0^{t'} dt'dt'' \langle f| H'(t')_{pump} |j\rangle \langle j| H''(t'')_{probe} |i\rangle e^{i\omega_{fj}t'} e^{i\omega_{ji}t''} + \cdots \end{aligned} \tag{1.11}$$

where $H(t)_{pump}$ and $H(t)_{probe}$ are the perturbation Hamiltonians induced by the respective light fields. Note that the first term is zero because $|i\rangle \neq |f\rangle$ and the second term is zero because the pump pulse cannot directly couple $|i\rangle$ and $|f\rangle$ as stated above.

Under the Born-Oppenheimer approximation, the wavefunction for each state can be written as a product of its electronic, $|\phi\rangle$, and nuclear, $|\chi\rangle$, components and in the case of $|f\rangle$, the photoejected electron $|e\rangle$

$$\begin{aligned} |i\rangle &= |\phi_i\rangle|\chi_i\rangle \\ |j\rangle &= |\phi_j\rangle|\chi_j\rangle \\ |f\rangle &= |e\rangle|\phi_f\rangle|\chi_f\rangle \end{aligned} \tag{1.12}$$

The perturbation Hamiltonians are of the form

$$H'(t) = -\vec{\mu}\cdot\vec{\epsilon} \tag{1.13}$$

where $-\vec{\mu}$ is the dipole moment of the molecule and $\vec{\epsilon}$ is the electric field applied by the laser.

In the Born-Oppenheimer approximation, the light can only interact with the electronic wavefunctions as the nuclear wavefunctions are unchanged during this perturbation. The coefficient can then be written as

$$c_2(t) \propto \frac{1}{\hbar^2}\int_0^t\int_0^{t'} dt'dt'' \langle e|\langle\phi_f|\vec{\mu}\cdot\vec{\epsilon}_{probe}|\phi_j\rangle\langle\phi_j|\vec{\mu}\cdot\vec{\epsilon}_{pump}|\phi_i\rangle\times e^{-i\omega_f t'-\omega_i t''/\hbar}\langle f|e^{iH'_{probe}(t'-t'')/\hbar}|j\rangle \tag{1.14}$$

From this expression, the probability for a transition in time t, $P_{f\leftarrow i}(t)$, and the transition rate, $\Gamma_{f\leftarrow i}(t)$, can be calculated using the following relations

$$P_{f\leftarrow i}(t) \propto |c_2(t)|^2 \tag{1.15}$$

$$\Gamma_{f\leftarrow i}(t) = \frac{dP_{f\leftarrow i}(t)}{dt} \tag{1.16}$$

1.5 Non-adiabatic Dynamics in Molecules

The previous few sections have all been written making use of the Born-Oppenheimer approximation. This approximation is incredibly useful and serves as a guide to visualizing how chemistry occurs. Many chemical processes that occur on only one potential energy surface (PES) are accurately treated by this approximation. However, in situations with high degrees of coupling between the nuclear and electronic degrees of freedom, it is inaccurate to simply picture nuclei as existing on a static potential energy surface created by the motion of electrons. This typically occurs when two PESs become very close to one another, allowing the wavefunction of the system to jump from one PES to another. This means that the electronic wavefunction defined by the PES is directly dependent on the nuclear movements of the molecule on that surface. The degrees of freedom that were previously treated as independent now depend upon each other in this regime and we must consider their coupling [35–42].

While the discussion of using a PES is inaccurate when there is coupling, this description is still widely used to understand the system. The vibronic wavefunction as described by the product of the adiabatic electronic and nuclear states of the molecule still form a complete basis for the system, and it is convenient to describe the diabatic states in this basis. The first thing we can write is the coupling between the two PESs (now referred to as the adiabatic states).

$$\mathbf{f_{ij}} = \frac{\langle\psi_{i,elec}|\nabla\hat{H}_{elec}|\psi_{j,elec}\rangle}{E_j - E_i} \tag{1.17}$$

where $|\psi_{i,elec}\rangle$ and $|\psi_{j,elec}\rangle$ are the initial and final adiabatic electronic wavefunctions, respectively, and E_i and E_j are their respective energies. This coupling is inversely proportional to

the difference in energy between the two states. The further apart the states are in energy, the weaker the coupling is between them.

An interesting case occurs when these two states become degenerate, known as a conical intersection (CI). As can be seen by Equation 1.17, if the two states have the same energy then their coupling diverges to infinity. This coupling allows for an extremely efficient and fast transfer of energy between two adiabatic surfaces in this region. As will be shown later, CIs cannot occur in diatomic molecules, but are ubiquitous to the chemistry that occurs in polyatomic molecules.

Let us consider a two state system to describe these CIs. We can represent the Hamiltonian of this system with the following matrix

$$\mathbf{H} = \begin{pmatrix} H_{11} & H_{12} \\ H_{21} & H_{22} \end{pmatrix} \tag{1.18}$$

where $H_{nm} = \langle \phi_n | \hat{H} | \phi_m \rangle$ and ϕ_i are the diabitic states of the system.

To move from the diabatic states to the adiabatic states, an orthonormal transformation of the form $\mathbf{S}^\dagger\mathbf{HS}$ is required where

$$\mathbf{S} = \begin{pmatrix} \cos(\alpha/2) & \sin(\alpha/2) \\ -\sin(\alpha/2) & \cos(\alpha/2) \end{pmatrix} \tag{1.19}$$

The angle α is such that it diagonalizes the matrix shown in Equation 1.18. The eigenvalues of this matrix are the energies of the adiabatic states and are

$$E_{1,2} = \frac{H_{11} + H_{22}}{2} \pm \sqrt{\left(\frac{H_{11} - H_{22}}{2}\right)^2 + H_{12}^2} \tag{1.20}$$

So far this discussion has been general for any two state system. If we specify these two states as existing at a conical intersection, the energy of the two states must be equal, this is only true when the two following conditions are met:

$$H_{11} - H_{12} = 0 \tag{1.21}$$
$$H_{12} = H_{21} = 0 \tag{1.22}$$

In a molecular system with N degrees of freedom, the CI exists in an $N-2$ subspace. This means that conical intersections cannot occur in diatomic molecules, only polyatomic. In diatomic molecules, an avoided crossing occurs when two PESs get too close together due to their limited dimensionality, however in polyatomics the additional nuclear degrees of freedom allow the existence of conical intersections.

1.6 XUV Generation

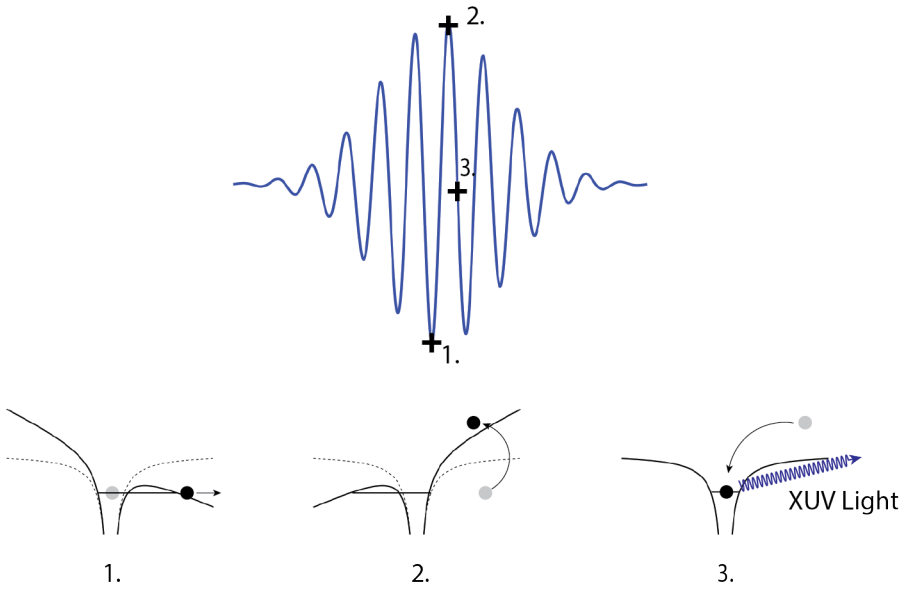

Figure 1.3: Schematic diagram of the three step model for HHG. Adapted from Reference [43]

Ultrashort Extreme Ultraviolet (XUV) light, typically defined as ranging from 10 – 124 eV, can be generated using high harmonic generation (HHG). HHG can be described semi-classically using Paul Corkum's 3 Step Model [44], shown in Figure 1.3. Briefly, a driving laser field is focused into a noble gas medium[3]. The large field strength distorts the Coulomb

[3]Other gases, or even solids and liquids can be used as well, but this thesis will focus only on noble gases

Gas	He	Ne	Ar	Kr	Xe
$\mathbf{I_P}$ **(eV)**	24.58	21.56	15.76	13.99	12.13

Table 1.1: The ionization potential of the noble gases

potential felt by the valence electrons allowing an electron to tunnel ionize out of the potential (Step 1). The electron is then driven away from the parent ion, gaining kinetic energy along the way. After a half cycle of the laser pulse, the distortion of the field changes sign and the electron is accelerated back towards the nucleus (Step 2). At the zero crossing of the electric field, the electron can then, with some probability, recombine with the ion causing the emission of a photon to conserve energy (Step 3). The energy of this photon is equal to the ionization potential of the gas, I_P, plus the kinetic energy gained on its trajectory, KE, shown in Equation 1.23

$$E = I_P + KE \tag{1.23}$$

The maximum allowable energy for this process is given by Equation 1.24

$$E_{max} = I_P + 3.17U_P \tag{1.24}$$

where U_P is the ponderomotive energy. The latter term is equivalent to the kinetic energy the free electron gains while in the continuum and is defined as

$$U_P = \frac{q^2 E_0^2}{4 m_e \omega_0^2} \tag{1.25}$$

where q is the charge of an electron, E_0 is the electric field amplitude, m_e is the mass of an electron, and ω_0 is the center frequency of the driving laser beam. The XUV light generated is not continuous, but is composed of odd harmonics of the fundamental laser frequency. This is due to interference effects between light generated during different half cycles of the electric field oscillations.

The parameters we can vary to adjust the energy of the harmonics generated are then the density and identity of the noble gas medium, the intensity of the driving laser beam in

the region of XUV generation, and the frequency of light used to generate harmonics. While many laboratories are pushing the limits on producing higher and higher pulse energies, our experiment only requires the pulse energy to be higher than the binding energy of the states we wish to study.

For the first set of experiments performed, we only need enough energy to eject valence electrons, so tens of eV photon energy is sufficient. Our requirements for generation are two-fold. (1) We want to have a high enough flux that we can see signal from dilute solvated species in water and (2) we need to have harmonics that are well separated in energy.

Since we are using the XUV beam as a probe for photoelectron spectroscopy experiments it is important to have a well-defined probe energy, otherwise multiple signals will arise from the same state. The spacing of the adjacent harmonics is 2ω since only odd harmonics are produced. This means that if we produce harmonics using light at a shorter wavelength, we will produce more widely spaced harmonics. Additionally, the efficiency of HHG goes as $\lambda^{-5.5}$ [45–47], so using a shorter wavelength gives a better conversion efficiency. Using a shorter wavelength driving pulse also lowers the maximum achievable photon energy in HHG (see Equation 1.24), but this is not particularly relevant to us as mentioned above.

1.7 Summary of Systems Studied

In Chapter 3 of this thesis, the relaxation dynamics of solvated thymine (T) and its derivatives thymidine (Thd) and thymidine-5'-monophosphate (TMP) are uncovered using femtosecond time-resolved photoelectron spectroscopy. This is done by coupling two ultraviolet laser pulses to a water microjet containing the NAC. The dynamics are monitored after absorption into two electronic regions, the first a $\pi\pi^*$ state which is pumped at 4.74 – 5.17 eV, and the second a higher lying band of states pumped at 6.20 eV.

It was found that the lower lying $\pi\pi^*$ state decays with a lifetime of $\sim$400 fs for both T and Thd. TMP, on the other hand, exhibited much longer decay times of around 670 – 840 fs depending on the energy of the pump pulse. The large increase in lifetime for TMP compared to T or Thd is found to be due to conformational differences between the molecules in solution leading to topological differences in the potential energy surfaces involved in relaxation.[4]

Another notable result was the lack of a long-lived signal. Previous studies on T and its derivatives have seen a signal that persists for tens of ps which has been attributed to a range of different states, most commonly the nearby optically dark $n\pi^*$ state. Our experiment has sufficient probe energy to monitor this state should it be populated, however all of the signal decays in $\sim$4 ps indicating that there is no involvement of the $n\pi^*$ state in the

[4]These findings were uncovered using XMS-CASPT2//CASSCF/AMBER calculations.

relaxation process. Finally, dynamics after excitation into the higher lying band at 6.20 eV were measured. It was found that there is an ultrafast transfer of the electron population back into the lower lying $\pi\pi^*$ state within the cross correlation of our laser pulses and then back into the ground state. More investigation into this higher lying band is needed for its full characterization.

One of the major drawbacks to the experiment described above is that it is blind to any dynamics occurring on the ground electronic state. The ground state of thymine is bound by 9.2 eV, in excess of our higher energy probe pulse of 6.2 eV. To solve this problem a femtosecond XUV light source was designed and built to allow a more complete tracking of these dynamics.

Chapter 2 describes the entire instrument as well as the design and build of our new XUV source which is capable of producing well isolated pulses at 21.7 eV using high harmonic generation. Chapter 4 then presents some of the preliminary results on the application of the XUV light to gaseous, liquid, and solvated species as well as future directions for the project.

References

(1) Barbatti, M., *Photoinduced Phenomena in Nucleic Acids I*; 1; Springer: 2015; Vol. 355, pp 1–65.

(2) Crespo-Hernández, C. E.; Cohen, B.; Hare, P. M.; Kohler, B. Ultrafast excited-state dynamics in nucleic acids. *Chemical Reviews* **2004**, *104*, 1977–2019.

(3) Shukla, M. K.; Leszczynski, J. Electronic spectra, excited state structures and interactions of nucleic acid bases and base assemblies: A review. *Journal of Biomolecular Structure and Dynamics* **2007**, *25*, 93–118.

(4) Middleton, C. T.; de La Harpe, K.; Su, C.; Law, Y. K.; Crespo-Hernández, C. E.; Kohler, B. DNA Excited-State Dynamics: From Single Bases to the Double Helix. *Annual Review of Physical Chemistry* **2009**, *60*, 217–239.

(5) Improta, R.; Santoro, F.; Blancafort, L. Quantum Mechanical Studies on the Photophysics and the Photochemistry of Nucleic Acids and Nucleobases. *Chemical Reviews* **2016**, *116*, 3540–3593.

(6) Pfeifer, G. P.; You, Y.-H.; Besaratinia, A. Mutations induced by ultraviolet light. *Mutation research* **2005**, *571*, 19–31.

(7) De Gruijl, F. R. Skin cancer and solar UV radiation. *European Journal of Cancer* **1999**, *35*, 2003–2009.

(8) Goodsell, D. S. The Molecular Perspective: Ultraviolet Light and Pyrimidine Dimers. *The Oncologist* **2001**, *6*, 298–299.

(9) Kleinermanns, K.; Nachtigallová, D.; de Vries, M. S. Excited state dynamics of DNA bases. *International Reviews in Physical Chemistry* **2013**, *32*, 308–342.

(10) De Vries, M. S.; Hobza, P. Gas-Phase Spectroscopy of Biomolecular Building Blocks. *Annual Review of Physical Chemistry* **2007**, *58*, 585–612.

(11) Fischer, I. Time-resolved photoionisation of radicals, clusters and biomolecules: relevant model systems. *Chemical Society Reviews* **2003**, *32*, 59–69.

(12) Kohler, B. Nonradiative decay mechanisms in DNA model systems. *Journal of Physical Chemistry Letters* **2010**, *1*, 2047–2053.

(13) Voet, D.; Gratzer, W. B.; Cox, R. A.; Doty, P. Absorption spectra of nucleotides, polynucleotides, and nucleic acids in the far ultraviolet. *Biopolymers* **1963**, *1*, 193–208.

(14) Shugar, D.; Fox, J. J. Spectrophotometric studies op nucleic acid derivatives and related compounds as a function of pH: I. Pyrimidines. *Biochimica et Biophysica Acta* **1952**, *9*, 199–218.

(15) Hare, P. M.; Crespo-Hernández, C. E.; Kohler, B. Internal conversion to the electronic ground state occurs via two distinct pathways for pyrimidine bases in aqueous solution. *Proceedings of the National Academy of Sciences* **2007**, *104*, 435–440.

(16) Pecourt, J. M. L.; Peon, J.; Kohler, B. Ultrafast internal conversion of electronically excited RNA and DNA nucleosides in water. *Journal of the American Chemical Society* **2000**, *122*, 9348–9349.

(17) Ismail, N.; Blancafort, L.; Olivucci, M.; Kohler, B.; Robb, M. A. Ultrafast Decay of Electronically Excited Singlet Cytosine via a π,π^* to n ,π^* State Switch. *Journal of the American Chemical Society* **2002**, *124*, 6818–6819.

(18) Langer, H.; Doltsinis, N. L.; Marx, D. Excited-State Dynamics and Coupled Proton–Electron Transfer of Guanine. *ChemPhysChem* **2005**, *6*, 1734–1737.

(19) Barbatti, M.; Lischka, H. Can the Nonadiabatic Photodynamics of Aminopyrimidine Be a Model for the Ultrafast Deactivation of Adenine? *Journal of Physical Chemistry A* **2007**, *111*, 2852–2858.

(20) Hudock, H. R.; Levine, B. G.; Thompson, A. L.; Satzger, H.; Townsend, D.; Gador, N.; Ullrich, S.; Stolow, A.; Martínez, T. J. Ab Initio molecular dynamics and time-resolved photoelectron spectroscopy of electronically excited uracil and thymine. *Journal of Physical Chemistry A* **2007**, *111*, 8500–8508.

(21) Groenhof, G.; Schä, L. V.; Boggio-Pasqua, M.; Goette, M.; Grubmü, H.; Robb, M. A. Ultrafast Deactivation of an Excited Cytosine-Guanine Base Pair in DNA. *Journal of the American Chemical Society* **2007**, *129*, 6812–6819.

(22) Sagan, C. Ultraviolet selection pressure on the earliest organisms. *Journal of Theoretical Biology* **1973**, *39*, 195–200.

(23) McQuarrie, D., *Quantum Chemistry*, 2nd ed.; University Science Books: 2007.

(24) McIntyre, D. H., *Quantum Mechanics*, 1st ed.; Pearson: 2012.

(25) Schatz, G. C.; Ratner, M. A., *Quantum Mechanics in Chemistry*, 1st ed.; Dover Publications: 2002.

(26) Franck, J.; Dymond, E. G. Elementary Processes of Photochemical Reactions. *Transactions of the Faraday Society* **1926**, *21*, 536–542.

(27) Condon, E. A Theory of Intensity Distribution in Band Systems. *Physical Review* **1926**, *28*, 1182.

(28) Neumark, D. M. Time-Resolved Photoelectron Spectroscopy of Molecules and Clusters. *Annual Review of Physical Chemistry* **2001**, *52*, 255–277.

(29) Stolow, A. Femtosecond Time-Resolved Photoelectron Spectroscopy of Polyatomic Molecules. *Annual Review of Physical Chemistry* **2003**, *54*, 89–119.

(30) Suzuki, T. Time-resolved photoelectron spectroscopy of non-adiabatic electronic dynamics in gas and liquid phases. *International Reviews in Physical Chemistry* **2012**, *31*, 265–318.

(31) Stolow, A.; Bragg, A. E.; Neumark, D. M. Femtosecond time-resolved photoelectron spectroscopy. *Chemical Reviews* **2004**, *104*, 1719–1757.

(32) Stolow, A.; Underwood, J. G. In *Advances in Chemical Physics*, 2008; Vol. 139, pp 497–583.

(33) Fischer, I.; Villeneuve, D. M.; Vrakking, M. J. J.; Stolow, A. Femtosecond wave-packet dynamics studied by time-resolved zero-kinetic energy photoelectron spectroscopy. *The Journal of Chemical Physics* **1998**, *102*, 5566.

(34) Batista, V. S.; Zanni, M. T.; Jefferys Greenblatt, B.; Neumark, D. M.; Miller, W. H. Femtosecond photoelectron spectroscopy of the I 2 anion: A semiclassical molecular dynamics simulation method. *Journal of Chemical Physics* **1999**, *110*, 3736–3747.

(35) Blanchet, V.; Zgierski, M. Z.; Seideman, T.; Stolow, A. Discerning vibronic molecular dynamics using time-resolved photoelectron spectroscopy. *Nature* **1999**, *401*, 52–54.

(36) Dilthey, S.; Hahn, S.; Stock, G. Approximate calculation of femtosecond pump–probe spectra monitoring nonadiabatic excited-state dynamics. *The Journal of Chemical Physics* **2000**, *112*, 4910.

(37) Tully, J. C. Perspective: Nonadiabatic dynamics theory. *The Journal of Chemical Physics* **2012**, *137*, 22A301.

(38) Havinga, E.; de Kock, R. J.; Rappoldt, M. P. The photochemical interconversions of provitamin D, lumisterol, previtamin D and tachysterol. *Tetrahedron* **1960**, *11*, 276–284.

(39) Havinga, E.; Schlatmann, J. L. Remarks on the specificities of the photochemical and thermal transformations in the vitamin D field. *Tetrahedron* **1961**, *16*, 146–152.

(40) Worth, G. A.; Cederbaum, L. S. Beyond Born-Oppenheimer: Molecular Dynamics Through a Conical Intersection. *Annu. Rev. Phys. Chem* **2004**, *55*, 127–158.

(41) Matsika, S.; Krause, P. Nonadiabatic Events and Conical Intersections. *Annual Review of Physical Chemistry* **2011**, *62*, 621–643.

(42) Domcke, W.; Yarkony, D. R. Role of Conical Intersections in Molecular Spectroscopy and Photoinduced Chemical Dynamics. *Annual Review of Physical Chemistry* **2012**, *63*, 325–352.

(43) Pfeifer, T.; Spielmann, C.; Gerber, G. Femtosecond x-ray science. *Rep. Prog. Phys* **2006**, *69*, 443–505.

(44) Corkum, P. B. Plasma perspective on strong field multiphoton ionization. *Physical Review Letters* **1993**, *71*, 1994–1997.

(45) Tate, J.; Auguste, T.; Muller, H. G.; Salières, P.; Agostini, P.; Dimauro, L. F. Scaling of Wave-Packet Dynamics in an Intense Midinfrared Field. *Physical Review Letters* **2007**, *98*, 013901.

(46) Shiner, A. D.; Trallero-Herrero, C.; Kajumba, N.; Bandulet, H.-C.; Comtois, D.; Légaré, F.; Giguère, M.; Kieffer, J.-C.; Corkum, P. B.; Villeneuve, D. M. Wavelength Scaling of High Harmonic Generation Efficiency. *Physical Review Letters* **2009**, *103*, 073902.

(47) Popmintchev, T. et al. Bright Coherent Ultrahigh Harmonics in the keV X-ray Regime from Mid-Infrared Femtosecond Lasers. *Science* **2012**, *336*, 1287–1291.

Chapter 2

Experimental Methods

2.1 Overview

This chapter will explore the experimental methods used to generate the data presented in this thesis, including hardware and software. Previously built equipment will be presented alongside newly made improvements, but more emphasis will be placed on the new aspects of the experiment.

2.2 Liquid Microjets

Photoelectron spectroscopy relies on measuring the arrival time of photoelectrons after they have been removed from a sample and have traveled through a time-of-flight tube. To prevent inelastic collisions from occurring during this process, it is necessary to perform these experiments under high vacuum conditions as the mean free path of the electrons is on the order of μm at atmospheric pressure. This makes studying volatile liquid samples particularly challenging.

To solve this problem, a liquid microjet is used in our experiments. Developed by Faubel et al. [1, 2] a liquid microjet is formed by forcing a liquid through an orifice small enough to satisfy the Knudsen condition, $\lambda > d$, where λ is the molecular mean free path and d is the diameter of the liquid jet [1, 3]. This condition is only satisfied for sufficiently small jet diameters. The use of thin jets is also beneficial in that it allows us to maintain relatively low pressures in our sample chamber using fairly traditional pumping techniques.

An important consideration in these experiments is the evaporation of the liquid jet. Although we are able to get chamber pressures in the range of $10^{-4} - 10^{-5}$ torr, local pressures around the jet in the so called vapor jacket are typically much higher. This vapor region is where collisions are most likely to occur so sampling the electrons close to the surface of the jet is the best way to limit inelastic scattering of our photoelectrons. This is accomplished by

maintaining a small jet diameter and sampling our photoelectrons before they have traveled through the entire vapor jacket. The gas density in the vapor region falls as r_0/r where r_0 is the jet diameter and r is the distance from the jet, so minimizing r_0 reduces the gas density. By placing a skimmer $\sim$1 mm away from the liquid jet we effectively change the gas source from a line source to a point source, changing the gas density scaling from $1/r$ to $1/r^2$ [1]. This allows the transition out of the vapor region (high pressure) to vacuum (low pressure) to occur over a much shorter distance. The skimmer also has the added benefit of lowering the pressure in the detector region allowing safe operation of our detector (described in the next section).

Our liquid microjet is based on the design of the Saykally group at UC Berkeley [3, 4] and is described in completion in the thesis of Alexander Shreve [5]. A brief description of the important components and some changes made to the jet assembly are described below.

The jet nozzle is created by pinching a fused-silica capillary (20 - 30 μm ID and 363 - 375 μm OD, PolyMicro) in a short length of PEEK tubing using a 1/16" Swagelok fitting (Swagelok, SS-100-6). This is coupled upstream to an in-line 2 μm stainless steel FRIT filter (Idex Health and Science, a-100). The PEEK tubing travels to our syringe pump (Teledyne Isco, 500D) which can either apply a constant backing pressure or a constant flow of the liquid through our jet. We have found that running the sample in the constant flow mode produces a more stable liquid jet.

Most of our previous work, and the work on thymine and its derivatives, was done using a 20 μm jet. These jets were typically run on constant flow mode at 0.2 mL/min. Stable jets exhibited backing pressures of between 80 – 100 atm for pure water and nucleobase solutions. More recent work has been done using 30 μm jets. Pure water jets were found to run nicely at 0.45 mL/min and around 40 atm of backing pressure, however depending on what is dissolved in the solution this number changes drastically, a phenomenon we have not observed with 20 μm jets. We have found flow rates ranging from 0.45 – 0.65 mL/min and pressures of 40 – 75 atm to all produce stable and well-behaved jets. It is typically best to experiment with jet conditions outside of vacuum before placing it in the sample chamber.

Our syringe pump has a 500 mL capacity and is equipped with two 2-stem needle valves (Vindum Engineering, MV-210-HC) to open and close the input and output ports. This pump provides a very stable jet, however the pump cannot be refilled while it is operating and cannot recirculate solution. Due to the age of this pump as well as these limitations it is recommended that it be upgraded to an HPLC pump in the next few years. Depending on what solution is being ran through the pump, it is important to rinse with appropriate solvents afterwards. When encountering jet problems, solutions of water, HCl, methanol, or isoproponal have all been useful in clearing out debris in the pump.

A few changes have been made to the jet since it was last described to allow it to couple

to our new catcher assembly which will be briefly discussed later in this thesis and more thoroughly in the upcoming thesis of Zachary Heim. Functionally, the assembly has the same features, only small changes have been made to enable this coupling.

2.3 Photoelectron Spectrometer

Our vacuum system is comprised of two main parts: the trap and the detector. This entire assembly is a series of three 10" CF vacuum chambers and is mounted on a custom built xy translation frame that has 2" of movement in both directions. The height of this rack can be manually adjusted by extending the feet individually. These manipulations are important as the XUV light cannot be steered while under vacuum so the chambers must be adjusted to align the XUV beam to the detector.

The trap is made up of the central 6-way cross chamber where our experiments are performed and an adjoining 4-way cross where we attach our pumps. The interaction region of the trap chamber is shown in Figure 2.1. The jet enters the trap chamber from above and is caught by a newly designed catcher assembly on the bottom. The laser intersects the jet orthogonal to its direction of travel and exits the chamber after passing through the jet. The final two directions feature a strong magnet that steers the ejected electrons into a 900 μm skimmer to our detector chamber. This will be described further in the next section.

This series of chambers is pumped by a 450 L/s turbo pump (Leybold 450i) and a 150 L/s turbo pump (Leybold 151) backed by an Edwards E2M18 mechanical pump. Our mechanical pump is equipped with a liquid nitrogen trap to protect it from water. Additionally, when using the liquid jet, cryogenic pumping is used by filling a 7L dewar with liquid nitrogen. This pump collects the water that evaporates from our liquid jet. This pumping scheme maintains pressures in the mid 10^{-5} torr range while running a 30 μm jet, sufficient for doing our experiments.

The jet is held in place on a custom designed mount that has a small 500 μm copper skimmer attached (see Figure 2.2). The jet shoots directly into this skimmer to minimize the amount of water vapor in our vacuum chambers. The skimmer is heated to 75 °C using a DC heater to prevent freezing of the liquid jet on the surface. The liquid that goes into the skimmer then travels down a tube into a collection bottle that is held at 0 °C by an ice bath. This collection bottle is backed out by an Edwards E2M28 mechanical pump to maintain an internal pressure of a few torr. This pump is also protected by a large cryogenic trap. This new jet assembly has increased our long term stability tremendously, allowing for continuous operation for as long as the entirety of a day. For a more detailed description of this assembly, refer to the upcoming thesis of Zachary Heim.

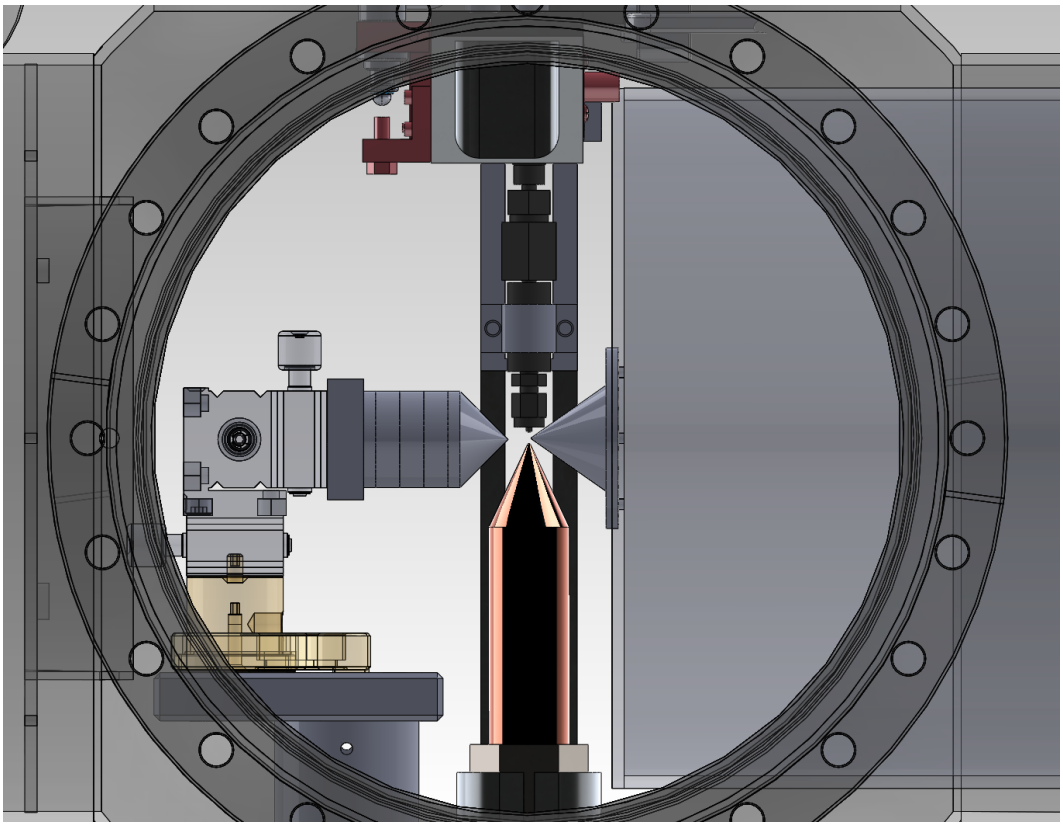

Figure 2.1: The jet assembly in the trap chambers. The jet travels from the top of the chamber into the catcher in the bottom. On the left is the strong permanent magnet and on the right is the skimmer leading to the detector. The laser travels through the jet orthogonal to both the jet axis and magnet axis.

The detector chamber is connected in vacuum to our trap chambers by the aforementioned 900 μm skimmer. This allows for differential pumping between the trap and detector chambers allowing the detector to operate at lower pressures, in the high 10^{-6} torr range. This chamber is pumped by one 1000 L/s (Leybold 1000C) and two 150 L/s (Leybold 151) turbo pumps which are backed by an Edwards E2M12 mechanical pump. This line also has a cryogenic trap between the mechanical pump and turbo pumps. At the end of this tube is a series of 2 microchannel plates (MCPs) (Photonis, Imaging Quality Long-Life MCP 25/12/10/12 I 40:1 TC) and a phosphor screen (Beam Imaging Solutions, PN-25-008). Low pressures in the detector are essential for operating our MCP assembly. Operating the detector at higher pressures has been found to crack the MCPs leading to arcing and random, high-ringing events to occur.

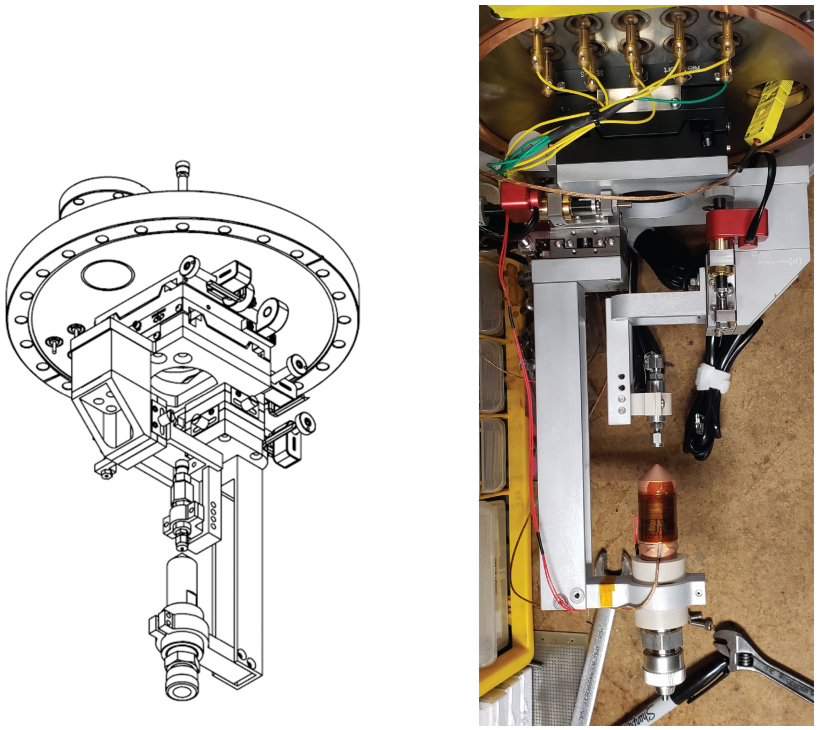

(a) Machine drawing of jet assembly (b) Photo of jet assembly

Figure 2.2: Machine drawing and photo of the jet and catcher assembly.

Magnetic Bottle

A magnetic bottle spectrometer is used in place of a traditional time-of-flight spectrometer to increase the electron collection efficiency from <1% to a theoretical limit of 50% [6, 7]. This means that any electrons ejected with a velocity component in the direction of the time-of-flight tube can be measured. In the first region, a strong inhomogeneous magnetic field is applied to the system. This field acts on the photoejected electrons via the Lorentz Force [8]

$$\vec{F} = q\vec{v} \times \vec{B}_i = qvB_i \sin(\theta_i) \tag{2.1}$$

where q is the charge of the electron, $\vec{v}_i$ is the velocity of the electron, $\vec{B}_i$ is the magnetic field applied by the magnet, and θ_i is the angle between the magnetic field vector and the velocity vector of the electron. This field causes the electrons to undergo helical motion, circling the field lines with an angular frequency, ω_i, given by

$$\omega_i = eB_i/m_e \tag{2.2}$$

where m_e is the mass of an electron. The radius of the orbit[1], r, is given by

$$r = v \sin\theta_i / \omega_i \tag{2.3}$$

In the second region a weak magnetic field (around 1000 times weaker) is applied to the time-of-flight tube. This weak field works to convert the helical motion of the electrons into on-axis translational motion. The angle of the helical motion of these electrons changes by the following relation

$$\frac{\sin\theta_f}{\sin\theta_i} = \left(\frac{B_f}{B_i}\right)^{1/2} \tag{2.4}$$

This tells us that as long as the field strength is lower in the second region, the angle will decrease. Since momentum is conserved in the process, this means that the angular momentum orthogonal to the time-of-flight axis is converted into momentum parallel to that axis.

Since the trajectory of every electron is not the same, it is reasonable to worry about a broadening of our signals since electrons of the same initial velocity will take different paths to reach the detector. Luckily, this effect is incredibly small. Assuming an isotropic distribution of photoelectrons, the spread in the arrival times given by $\Delta T/T$ is only $\sim 0.5\%$ and the resolving power in energy space, $\Delta E/E$, is $\sim 1\%$ [6]. These changes are small enough to be unnoticed even when measuring photoelectron spectra of systems with narrow peak widths such as the noble gases. If the strong magnet is misaligned, a significant broadening and decrease in intensity are seen providing a useful method for magnet alignment.

This technique is implemented by placing a rare earth magnet stack composed of Ni-coated SmCo (McMaster Carr, 57325K93) and Nd (McMaster Carr, 58605K85) disk magnets with an iron cone (Ed Fagan Inc., Hiperco 50A) on a 3-axis translation stage (Newport, 9064-XYZ) in front of the jet. The magnet provides a 1.1 T field at the interaction region and can be moved relative to the jet and the detector while under vacuum using picomotors (Newport, 8302) allowing for in vacuum alignment. The detector is surrounded by a 26" long solenoid which is 14 gauge copper wire wrapped at 10 turns per inch. A current of 1.5 A is applied to this wire producing a calculated field strength of 10 Gauss in the time-of-flight region.

Detector Assembly

The detector used for these experiments is an MCP stack with a phosphor screen. An MCP is a highly resistive flat plate with a series of channels [9, 10]. If an electron, or a photon of

[1]This is also referred to as the cyclotron radius

high enough energy, hits one of these channels it starts an electron cascade down the channel effectively acting as an electron multiplier. A bias voltage is applied across the plates to accelerate electrons from the front to the back. Stray fields are eliminated by having a grounded Ni mesh sit directly in front of the detector assembly. These detectors are highly sensitive both spatially and temporally and thus make great detectors for the experiments performed in this thesis.

The channels in the MCPs are not perpendicular to the face of the plate, but are angled relative to the surface normal. By putting two plates in an opposing configuration, called a chevron stack, we minimize the occurrence of after pulses generated by positive ions creating a second electron cascade. Having two plates also increases the gain of the detector. If needed, a third plate can be installed in a "Z" configuration to further this gain, but that has not been necessary for our experiment thus far. Our detector currently has an empty spot where a third MCP could be installed if necessary with only minor modifications to the detector circuit.

The two MCP plates are coupled to a phosphor screen in our detector. This entire assembly in housed in a home-built holder described in the thesis of Alexander Shreve [5]. A bias voltage of 2.25 kV is applied by a high voltage power supply (Bertran, 205B-05R) to the back MCP plate which is resistively coupled to the front plate reducing the voltage by half. The phosphor screen is held at 3.25 kV by another high voltage power supply of the same type. Having an increasing voltage across each set of plates accelerates the electrons through the detector and ensures that electrons are replenished, preventing charging. The overall gain of our detector is $\sim 10^8$. Electrons hitting the phosphor screen cause it to glow providing an image of the electrons that we are measuring. This can be used as an alignment tool for the magnetic bottle as a well-aligned magnet produces a small and circular spot on the detector.

The signal is measured off of the back MCP by sending the current through a 1000 pF capacitor to a digitizer card installed in our PC. The complete circuit diagram can be found in the theses of Alexander Shreve [5] and Madeline Elkins [11], but this is the first description of the ADC card. This card acts as an analog to digital converter (ADC). The card converts the current off of the MCP into voltage vs. time of arrival, giving us our spectra. Sometimes, an amplifier (Ortec, 9301) is installed after the capacitor and before the card to amplify the signal 10-fold. This can be advantageous when working with weak signals, but has often lead to more ringing in our counts.

A useful measurement to make sure our detector is working properly is to measure what single electron events look like. These are called "dark counts". Dark counts on our detector are typically around 8 mV in intensity and 8 ns long. These counts can be distorted by a variety of different factors and can be a diagnostic tool if the signals off of the detector look odd. There is always ringing present in the dark counts with a period of around 8 ns. This

ringing should be minimized as much as possible, but does not usually impact the quality of the data measured as the signals are significantly wider than 8 ns. In the future, it may be important to reduce this further when measuring very fast photoelectrons.

Due to the generation of much faster photoelectrons than previous experiments, a new decelerator has been designed for the detector chamber. This decelerator is currently being integrated into our detector as this thesis is being written. This decelerator works in the manner of Wörner et al. [12] where a negative DC field is introduced to the detector, repelling photoelectrons. This allows for a static offset to the kinetic energy of the electrons that hit our detector. This has two advantages: 1) this can be used to reject slow photoelectrons from liquid water. Liquid water produces a huge photoionization signal (see Chapter 4). By setting the voltage of the decelerator just above the kinetic energy of these peaks, we can stop them from hitting our detector and prevent saturation. 2) Since our detector detects in ToF, not eKE, slower electrons lead to better resolution. By slowing down the electrons that we are measuring we can hopefully resolve features that currently overlap in our spectrum.

A schematic diagram of this is shown in Figure 2.3 where the two dotted lines each represent an electroformed Ni mesh with 88.6% transmission (Precision Eforming, MN49). The black mesh is grounded to the ToF tube and the red one is floating at a variable negative voltage. This floating mesh is welded onto another tube (approximately 24" long and 3.25" OD) inside of the detector and is electrically isolated from the rest of the detector. This tube is then in electrical connection with the mesh in front of the detector; instead of being grounded it will now be floating at the set voltage to prevent the reacceleration of the electrons.

2.4 Data Acquisition

Signal is capacitively coupled off of the back MCP[2] and sent to an Acqiris U5309A digitizer card. This card acts as an analog-to-digital converter and can act in many different acquisition modes (see Appendix E for detailed information on the software currently used). This card is triggered by a delay generator that is set to trigger 16ns before a laser pulse hits our detector. This delay generator sets the timing of the experiment relative to the generation of laser pulses, described later in this chapter.

At some point during the past decade a lot of source code was lost due to improper data storage — only the executables were found. The code used for data acquisition in the previous theses was largely lost, although an older but nonfunctional version was recovered

[2]The phosphor screen was used previously, but was damaged and gave large amounts of ringing. Now that it has been replaced we can switch back to this orientation, but it has not seemed necessary.

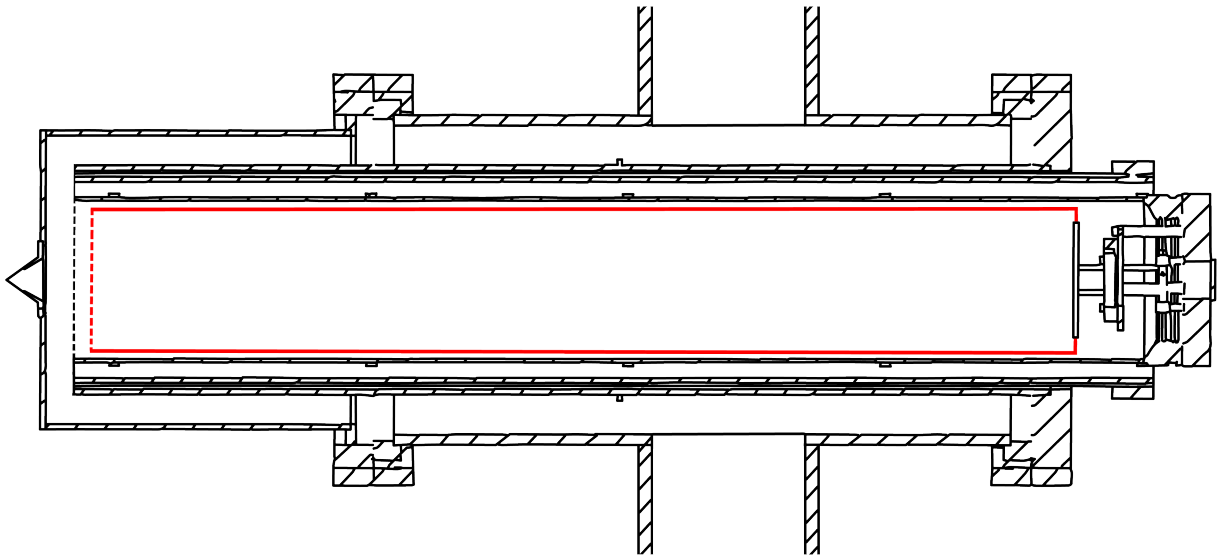

Figure 2.3: Schematic diagram of the electron decelerator to be installed in our detector. Red lines indicate that it is held at a floating voltage while black lines are grounded.

from a CD backup. This code was fixed to allow time-resolved data to be taken on the oscilloscope described in the thesis of Holly Williams [13]. That code was then updated to allow time-resolved data acquisition on the new ADC card.

The time-resolved data acquisition code allows for averaged data to be collected as a function of time-delay. The program can take any number of shots at a given stage position (this number is typically 1000 – 2000). Historically, after the program has sampled every stage position it would set the stage delay to 0 and take one-color backgrounds before repeating the scan. Now, the user can take one-color backgrounds at every delay position for one or two of the laser pulses. Additionally, a manual time delay is built in to delay the program after taking background scans as the XUV line takes a few seconds to stabilize in power after being blocked. This could be mitigated by installing a shutter in vacuum rather than using the flag before the harmonic generation line.

New codes have been written to acquire both static and time-resolved data in averager, single shot, peak detection, and counting modes. These are described in more detail in Appendix E. Additionally, more thorough backups have been put in place to prevent the loss of this code. Both physical and cloud storage backups are now being used.

2.5 Post-Processing

There are two main methods used by our lab to analyze time-resolved data, both of which have been covered thoroughly in the theses of Madeline Elkins [11] and Holly Williams [13]. For that reason, only a brief description is provided below.

Lane Integration

When spectral features are energetically separated from other features, the simplest technique to use is lane integration. Briefly, a summation of all of the data that are in the eKE range of the feature is taken and plotted against delay time. This feature can then be fit against various functions to find the minimum number of kinetic components required to accurately reproduce the data. The form of this fit is typically a sum of exponential decay functions convoluted with a Gaussian function (the cross correlation of our laser pulses). Each exponential decay is multiplied by a Heaviside function at $t = 0$. The fitting function is written as [14]

$$f(t - t_0) = \frac{I_0}{2} e^{(\sigma^2/(2\tau^2) - (t-t_0)/\tau)} \left[erf\left(\frac{t - t_0}{\sigma\sqrt{2}} - \frac{\sigma}{\tau\sqrt{2}} \right) + 1 \right] \tag{2.5}$$

where $t - t_0$ is the time relative to the beginning of the process (when the pump pulse interacts with our system), I_0 is the initial intensity of the feature, σ is the cross correlation of the pulses used in the experiment, and τ is the lifetime of the state which is the fitted parameter.

Global Lifetime Analysis

The second method we use of fitting data is Global Lifetime Analysis (GLA) [14–19]. This technique is especially powerful when there is spectral congestion, a very common feature in condensed phase systems. First we must assume that the data can be accurately separated into two components; one of which depends only on energy, $S_j(eKE)$, and another which depends only on time delay, $S_j(\Delta t)$. This means that the complete data set, $S(eKE, \Delta t)$, can be written as a summation of all of the components which are each made up of the product of these two terms

$$S(eKE, \Delta t) = \sum_{j=1}^{n} \sigma_n S_j(eKE) S_j(\Delta t) \tag{2.6}$$

where n is the total number of spectral components and σ_n is the relative weighting of each component. As stated in the previous section, our data takes the form of a sum of monoexponential functions convoluted with the the instrument response function. The data can then be represented as

$$S(eKE, \Delta t) = \sum_{k=1}^{m} DAS_{\tau_k}(eKE)[e^{-t/\tau_k} \times IRF] \tag{2.7}$$

We can then fit this equation using a least squares fitting algorithm. The parameters fit are: $DAS_{\tau_k}(eKE)$, time zero, IRF, and a static vertical offset parameter. The value for IRF can also be fixed if it is directly measured in another experiment. One should always try to fit the data with as few kinetic components as possible as this model cannot predict the actual kinetics of a process. A very nice visualization of GLA can be found in the thesis of Holly Williams [13].

2.6 Beamline

One of the more complicated aspects of this experiment is the formation and manipulation of ultrashort laser pulses. Our laser system is Coherent Astrella which outputs 800 nm light with a 35 fs pulse duration. At install this laser system gave 7 mJ per pulse at a 1 kHz repetition rate, however typical operating conditions give around 6.25 mJ per pulse.[3] This laser is a Ti:Sapph amplifier pumped by a Revolution Nd:YLF laser and seeded by a Vitara diode laser which is pumped by a Verdi-G oscillator. Large portions of this laser system are enclosed in hemetically sealed regions, the only thing available to manipulate is the Ti:Sapph amplifier cavity and the steering into the stretcher and compressor. The power of the Verdi-G and Revolution systems can also be changed by a nearby PC. A complete description of how this laser system works, as well as install and alignment notes, can be found in the thesis of Holly Williams [13].

After the beam exits the Astrella, it is split into three separate parts. A 1.2 mJ portion of the beam is sent into a β-Barium Borate (BBO) based sum frequency generation line which is used to frequency upconvert the 800 nm light to the second (400 nm), third (266 nm), or fourth harmonic (200 nm) of the laser frequency. 4.75 mJ of the beam is used to pump a BBO crystal for second harmonic generation, producing around 0.9 - 1.1 mJ of 400 nm light. This light is then used to drive our new XUV beamline. The final 1.05 mJ of the beam is sent into our OPA system to produce tunable ultraviolet light in the range of 235 – 260 nm. All three of these pulses can be aligned onto our sample depending on our experimental requirements. The following sections will describe the operation of these elements with particular focus on the XUV line as this is its first description. An overview of this beamline is shown in Figure 2.4

[3] All values for power are listed as if the laser is outputting 7 mJ per pulse.

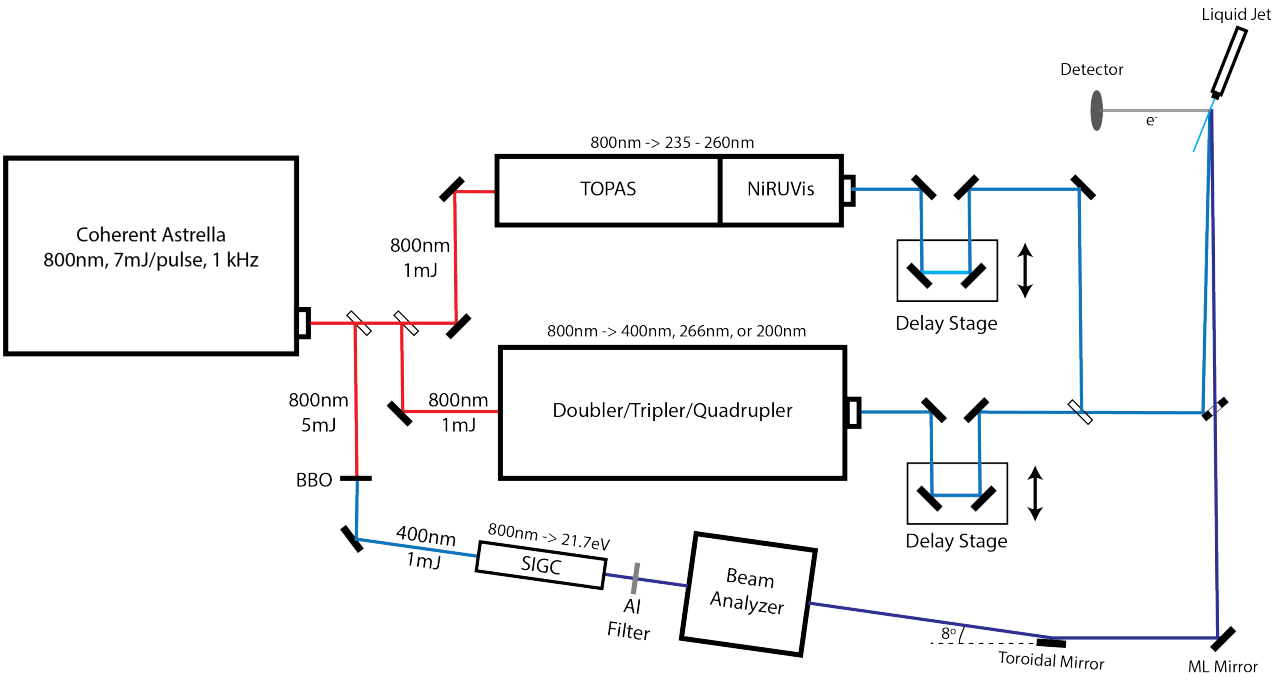

Figure 2.4: A simplified diagram of our beamline. Note that any combination of the three beams can be used during our experiments.

Sum Frequency Generation Line

Ultraviolet pulses of 400 nm, 266 nm, and 200 nm are produced by sum frequency generation (SFG) in BBO crystals. Below is a brief description with some of the more important results from Boyd [20]. A complete derivation and more detailed treatment can be found in that text.

We start by defining the polarization, $\mathbf{P}(t)$, as a Taylor series of the dipole moment.

$$\mathbf{P}(t) = \epsilon_0 \chi^{(1)} \mathbf{E}(t) + \epsilon_0 \chi^{(2)} \mathbf{E^2}(t) + \epsilon_0 \chi^{(3)} \mathbf{E^3}(t) + \cdots \tag{2.8}$$

where $\mathbf{E}(t)$ is the applied electric field vector, ϵ_0 is the permittivity of free space, and $\chi^{(n)}$ is the nth order susceptibility of the medium. A linear optical response allows us to ignore any high order terms and we find that the polarization is linearly dependent on the electric field strength. However, when the field strength is very high, as is the case for many ultrashort laser pulses, the higher order terms become quite large. It is also important to note, but will not be derived, that the second order susceptibility goes to zero in centrosymmetric materials. This means second order polarization responses are only seen in noncentrosymmetric materials. This does not apply for third order responses but, for this section, we will focus

only on the second order term, $\mathbf{P}^{(2)}(t)$.

$$\mathbf{P}^{(2)}(t) = \epsilon_0 \chi^{(2)} \mathbf{E^2}(t) \tag{2.9}$$

If we first start with the simple case of second harmonic generation, we can write the electric field as

$$\mathbf{E}(t) = E(e^{-i\omega t} + e^{i\omega t}) \tag{2.10}$$

where ω is the center frequency of the field incident on the material. If we substitute Equation 2.10 into Equation 2.9 and simplify we get

$$\mathbf{P}^{(2)}(t) = 2\epsilon_0 E E^* + \epsilon_0 \chi^{(2)} E^2 e^{-2i\omega t} + \epsilon_0 \chi^{(2)} E^2 e^{2i\omega t} \tag{2.11}$$

Using Maxwell's Equations we can derive the following wave equation that describes how the time-dependent polarization can cause the creation of electromagnetic fields

$$\bigtriangledown^2 \mathbf{E} - \frac{n^2}{c^2} \frac{\partial^2 \mathbf{E}}{\partial t^2} = \frac{1}{\epsilon_0 c^2} \frac{\partial^2 \mathbf{P}^{NL}}{\partial t^2} \tag{2.12}$$

where n is the refractive index, c is the speed of light in vacuum, and $\mathbf{P}^{NL}$ is the non-linear portion of the induced polarization. This makes sense physically as it relates the creation of electromagnetic waves to the acceleration of charged particles in the medium ($\frac{\partial^2 \mathbf{P}^{NL}}{\partial t^2}$). Using this relation, the first term of Equation 2.11 vanishes due to its lack of time-dependence and we create a new field with frequency 2ω, the second harmonic of the driving light, ω.

If two beams of different frequencies, ω_1 and ω_2, are applied to the medium instead, we can follow the same steps as above to describe second harmonic generation, sum frequency generation, and difference frequency generation (and a technique known as optical rectification which will not be described). We first start by defining the applied field as

$$\mathbf{E}(t) = E_1 e^{-i\omega_1 t} + E_2 e^{-i\omega_2 t} + cc \tag{2.13}$$

where we have adopted the truncated notation where cc is the complex conjugate of the prior terms. We can then substitute this expression into Equation 2.9 as we did before to get

$$\begin{aligned}\mathbf{P}^{(2)}(t) = \epsilon_0 \chi^{(2)} [E_1^2 e^{-2i\omega_1 t} + E_2^2 e^{-2i\omega_2 t} + 2E_1 E_2 e^{-1(\omega_1+\omega_2)t} + 2E_1 E_2^* e^{-1(\omega_1-\omega_2)t} + cc] \\ + 2\epsilon_0 \chi^{(2)} [E_1 E_1^* + E_2 E_2^*]\end{aligned} \tag{2.14}$$

This is more conveniently expressed as a series expansion over the polarizations at different frequencies

$$\mathbf{P}^{(2)}(t) = \sum_n P(\omega_n) e^{-i\omega_n t} \tag{2.15}$$

Nonlinear process	**wavelengths**	**crystal angle**
SHG	800 nm + 800 nm $\rightarrow$ 400 nm	29.2°
SFG	400 nm + 800 nm $\rightarrow$ 266 nm	45.0°
SFG	266 nm + 800 nm $\rightarrow$ 200 nm	65.0°

Table 2.1: Description of the SHG and SFG processes used in our lab.

We find the following frequency components of the polarization:

$$\begin{aligned} P(2\omega_1) &= \epsilon_0 \chi^{(2)} E_1^2 \\ P(2\omega_2) &= \epsilon_0 \chi^{(2)} E_2^2 \end{aligned} \tag{2.16}$$

which correspond to second harmonic generation of ω_1 and ω_2.

$$\begin{aligned} P(\omega_1 + \omega_2) &= 2\epsilon_0 \chi^{(2)} E_1 E_2 \\ P(\omega_1 - \omega_2) &= 2\epsilon_0 \chi^{(2)} E_1 E_2^* \end{aligned} \tag{2.17}$$

which correspond to sum frequency generation and difference frequency generation, respectively. And finally,

$$P(0) = 2\epsilon_0 \chi^{(2)} (E_1 E_1^* + E_2 E_2^*) \tag{2.18}$$

which is the optical rectification mentioned earlier. We have shown that four separate frequencies can be generated by the $\chi^{(2)}$ susceptibility of a material, but typically only one is seen in the laboratory. The reason for this is because we did not include phase matching conditions in the previous section. Typically a media will only allow for one of these processes to occur in a given material/orientation. The phase matching condition is given by

$$\Delta k = \vec{k_1} + \vec{k_2} - \vec{k_3} = 0 \tag{2.19}$$

where $\vec{k_n}$ is the wave vector for an applied field, E_n, given by $k_n = 2\pi/\lambda_n$. k_1 and k_2 are the input beams and k_3 is the newly created beam. This phase matching condition is specific for each input wave vector and therefore can be controlled to allow only one non-linear process to occur in the medium. In our experiments, we use BBO crystals (Eksma Optics, THATSHIGH Photoelectric Technology Co., or Crystech, 10mm x 10mm p-coated) cut at different angles to dictate which process occurs. Table 2.1 shows the crystal angles we use for different nonlinear processes.

Our sum frequency line has an input of 1.2 mJ of 800 nm light. Table 2.2 shows typical efficiencies and powers of each of the processes outlined above. The crystals used have a

wavelength	efficiency	power
400 nm	25%	300 mW
266 nm	5%	60 mW
200 nm	1%	1.2 mW

Table 2.2: Typical efficiencies and powers of SHG/SFG processes done in our lab.

thickness of 200 μm. Typically, a thicker crystal gives a longer distance for phase matching to occur, increasing the conversion efficiency. However, due to the wavelength-dependent index of refraction of the crystal, it also will also apply chirp to the pulse leading to an increased pulse duration[4]. It was found that decreasing the thickness below 200 μm is not beneficial to decreasing the pulse duration as most companies will mount crystals below this thickness with a thick support that also stretches the pulse, defeating the purpose of using thinner crystals. Depending on the desired final pulse energy thicker crystals can be used, but the powers listed above have proved more than sufficient for our experiments thus far.

XUV Line

The most significant change made to the experiment during this thesis work was the design and fabrication of a new XUV beam line. This section will go through the entire beamline and describe each element. The beamline is divided into 3 regions: the semi-infinite gas cell chamber, the beam analyzer chamber, and the beam manipulation chambers. All of these regions are held under vacuum to avoid absorption of the generated XUV light. There are 2-3/4" CF gate valves (MDC Vacuum Products, 303001-01) between each of these regions as well as between the last region and the sample chamber to allow isolation for venting individual chambers and leak testing.

The driving pulse used for generating harmonics can be either 800 nm or 400 nm, although we solely generate harmonics with 400 nm currently. 4.75 mJ of the Astrella output is put into a 1 mm thick doubling BBO crystal (Eksma Optics, BBO-1004H) to generate 0.9 – 1.1 W of 400 nm light via SHG (see previous section for details on this process). This light is focused using a 1.0 m lens into our semi-infinite gas cell. The focus quality is assessed by a DFK USB camera equipped with an ND 4.0 filter on the outside of the gas cell. This is best done with very weak powers to avoid burning the camera. Imaging of the focus can also be accomplished elsewhere in the line by placing a cheap webcam that has its IR filter

[4]SHG and SFG always lengthen the temporal duration of an ultrafast pulse even ignoring chirp due to the time-energy uncertainty principle, but this is unavoidable.

removed into the focus.

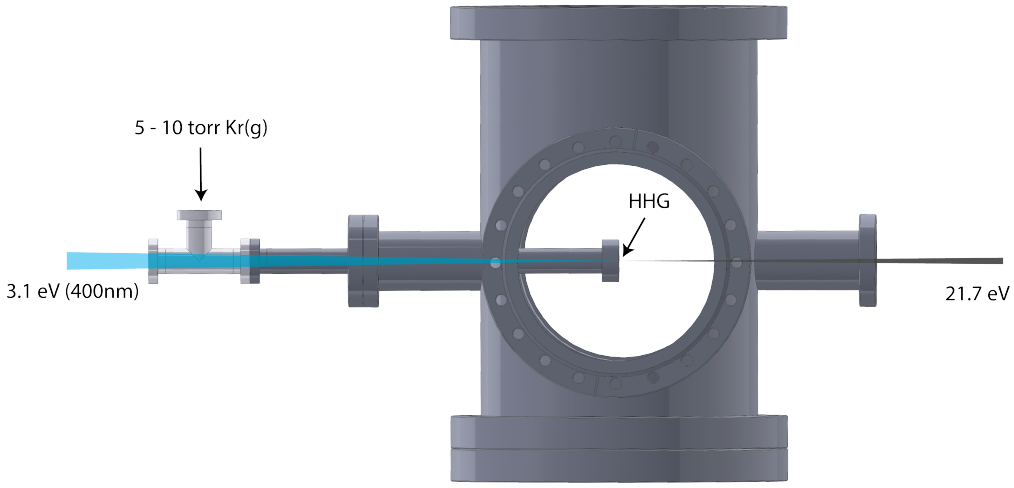

Figure 2.5: SIGC chamber

Semi-Infinite Gas Cell Chamber

The semi-infinite gas cell is seated in a custom designed vacuum chamber. It comprises a 27 cm long tube, shown in Figure 2.5. The end leading to atmosphere is further extended with two 1-1/3" CF tees (Duniway, TE-0133) and two 1-1/3" CF full nipples (Duniway, NP-0133) to prevent burning of the window that allows the driver into the chamber. This extends the SIGC to a total length of 57.5 cm. The gas cell is supplied with noble gases (99.9999% purity) through a needle valve on one of the CF tees. The positive pressure in the gas cell is monitored by a Baratron gauge (MKS Instruments, 622C13TBE) and pressure meter (MKS Instruments, 660C12) on the other CF tee to provide repeatable and stable conditions for generating harmonics.

The laser is focused at the exit of the gas cell where it is capped with two 0.005" stainless steel caps cut from a large sheet (McMaster Carr, 3254k93) to circles of 3/4" by the machine shop. A hole in these caps is laser drilled by our driving pulse to make a small hole that allows the harmonics to exit the cell into the vacuum chamber. These caps need to be replaced about every month or whenever the laser is realigned upstream. This is readily accomplished by removing the o-ring flange on the front of the chamber and removing the cap on the SIGC. If the XUV flux is anomalously low, this is usually the first action to take.

High pumping speeds are necessary for this chamber as the gas load leaving the cell is relatively high. This chamber is pumped by a 1000 L/s turbo pump (Leybold 1000C) backed

by an Edwards E2M18 mechanical pump. Typical gas cell pressures range from 5 – 10 torr and are optimized daily to maximize XUV flux. The pressure in the chamber is typically around 10^{-3} torr even with the relatively high pumping speed.

At the exit of this chamber, there is a 2-3/4" CF blank gasket (Duniway, BG-0275) that has a 3/16" hole drilled in it to prevent the high semi-infinite gas cell pressures from reaching the other chambers. This hole size was determined by estimating the XUV spot size[5] at that point and experimentally iterating different sized holes to get the smallest hole that did not clip the beam. These gaskets prove useful as alignment tools when outside of vacuum, as well.

Bean Analyzer Chamber

The beam analyzer chamber is connected to the semi-infinite gas cell through a 85 cm long defocusing tube. This tube ensures that the beam has expanded enough to avoid burning the optical elements in this chamber. This chamber is a 10" CF 6-way cross that was previously used as the sample chamber. It has slightly larger dimensions than a standard 6-way cross which can be found in the thesis of Alexander Shreve [5]. This chamber is pumped by a 450 L/s turbo pump (Leybold 450i) and backed by a Pfeiffer Duo 11M mechanical pump, allowing it to reach chamber pressures of around 10^{-6} torr during operation. When roughing this chamber it is necessary to do so very slowly to avoid breaking the foil filters in the chamber. This is done by slowly opening a butterfly valve which is on the bellows connecting the mechanical pump to the chamber.

The beam first encounters a 200 nm thick Al foil (Lebow Company, 0.2Al-M-L1.0) which acts to filter out the driving laser, see Figure 2.6 for the transmission of this filter. Various other foils can be used instead to cut off different harmonic energies for future experiments. The custom designed foil holder is on a linear manipulator (MDC, BLM-133-6) with 6" of travel so that the foil can be changed while under vacuum. There are four slots available. One slot is usually left empty, allowing the driver to pass through the chamber for alignment purposes. Care needs to be taken not to allow high power driver light through this region, especially while at atmosphere, as it can burn downstream optics.

After the Al foil filter, the transmitted XUV light is sent through a beam enclosure and onto a 50 μm x 3 μm slit (Lenox Laser, mounted A-SLIT-3/8-DISC) to form a thin vertical beam. The light that passes through the slit then goes onto a 100 nm periodicity transmission nanograting (LumArray Inc.) which separates the different harmonics horizontally based on their energy according to the following relation

$$dSin\theta = n\lambda \tag{2.20}$$

[5]A good first order approximation is that the XUV beam defocuses at about 1/3 the rate as the driving pulse.

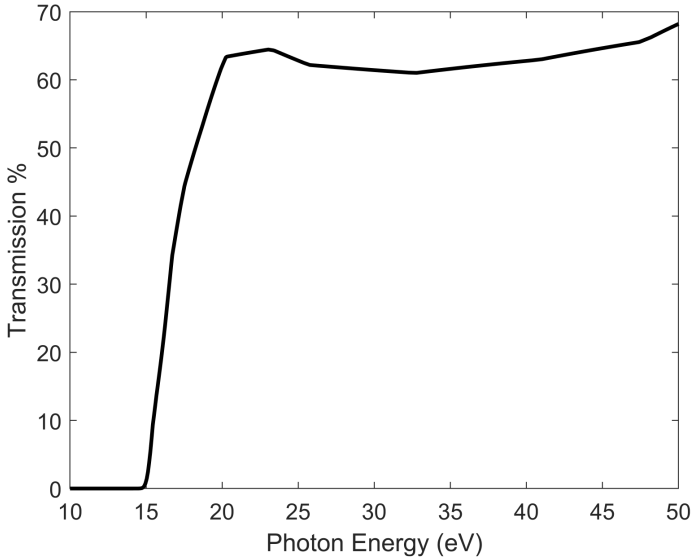

Figure 2.6: 200 nm thick Al foil transmission calculated from the CXRO filter transmission database [21].

where θ is the angle of diffraction, d is the spacing of the lines in the grating, n is the order of diffraction[6], and λ is the wavelength of light. As is seen, a unique angle will be observed for each unique wavelength, leading to spatially separated harmonics.

The diffracted light then travels onto a 2" diameter MCP stack and a phosphor screen. This setup is almost identical to that of our detector which has been described previously and operates under the same principle except that XUV light is used to start the electron cascade instead of photoelectrons. Additionally, this detector is used for spatial imaging rather than temporal analysis, so the detector is larger (2" vs 1" in diameter). The same power supplies are used for this MCP stack as our detector as they are never operated simultaneously. To image off of the phosphor, the voltage applied to it is usually increased by $\sim$ 500V. The light emitted by the phosphor screen is then reflected by an Al mirror to a viewport on the outside of the chamber where it is imaged by a CMOS USB Camera (Edmund Optics, EO-1312M) and a zoom lens (JH Technologies Inc., ZOOM 7000) and read out on a nearby PC.

This whole assembly is on a custom vacuum compatible translation stage with 2" of linear movement (Newport Corp., 07SI25007) that is mounted onto a custom designed flange. By moving the stage a second mode of operation is enabled. Instead of a slit and a diffraction grating, the beam will travel through a tube directly onto the MCP stack and phosphor

[6]We have only observed first order diffraction, so this is equal to 1

screen. This enables us to see the beam profile. Finally, when running our experiment this stage can be translated so that the beam travels directly through this chamber, bypassing all of these elements.

While this analyzer is not used on a day-to-day basis, it is incredibly useful when first characterizing what harmonics are being generated prior to the next region in our vacuum chambers. This gives a good qualitative measure of the relative intensity of the harmonics as well. Brighter spots generally mean there are more incident photons, which can help when choosing which harmonic to select and use for our experiment.

Beam Manipulation Chambers

The final section of the XUV line is a series of three 10" CF 6-way crosses that are used to manipulate the generated XUV beam. These chambers are connected through large ports allowing only one 450 L/s turbo pump (Leybold 450i) backed by an Edwards E2M28 mechanical pump to pump this whole region, achieving operating pressures of around 10^{-6} torr.

The first of the three chambers has a gold toroidal mirror from ARW Corporation[7] which is used to focus the XUV beam. This mirror has a focal length of 992 cm.[8] The mirror sits on top of two linear translation stages with 1" of travel (Newport Corp., 07SI25008) that can manipulate the stage in the x and y directions. On top of the linear stages is a rotation stage (Newport Corp., 07SI26049) which allows for the angle of the mirror relative to the XUV beam, the yaw, to be changed. The mirror is designed to be used at a 4° incident angle and is highly sensitive to this degree of freedom. The mirror is mounted in a custom holder that can control both the height of the mirror (the z axis) and the pitch by using threaded bolts. The only degree of freedom this mount cannot control is the roll, but we have been able to achieve very good beam profiles even without this. These parameters are manipulated to achieve the smallest circular beam profile at the focus. Small changes to the alignment will cause oval beam profiles which should be avoided. Since the XUV beam travels the same beam path as the driving beam, this mirror can be aligned outside of vacuum but care should be taken to minimize the intensity of light put onto the mirror. This can be done through lowering delay 2 on the signal delay generator and by using multiple neutral density filters. We try to limit the driving pulse to 10 mW (10 μJ/pulse) or lower during alignment.

The second chamber is used for selecting a single harmonic. In photoelectron spectroscopy it is important to have a well-defined probe energy. If multiple harmonics are impinging on a sample, the same state will lead to multiple peaks in the spectrum and cause spectral

[7] **Radii (Concave)**: $R_1 = 12322.8 \pm 1\%, R_2 = 93.6mm \pm 1\%$ **Dimensions**: $160.0mm(R_1) \pm 0.10mm \times 30.0mm(R_2) \pm 0.10mm,\ 20.0mm \pm 0.15mm$ center thickness

[8] It is very important to note that the distance from the toroidal mirror to the spot you are imaging (and consequently, the distance from the mirror to the focal point) is 2f, not f.

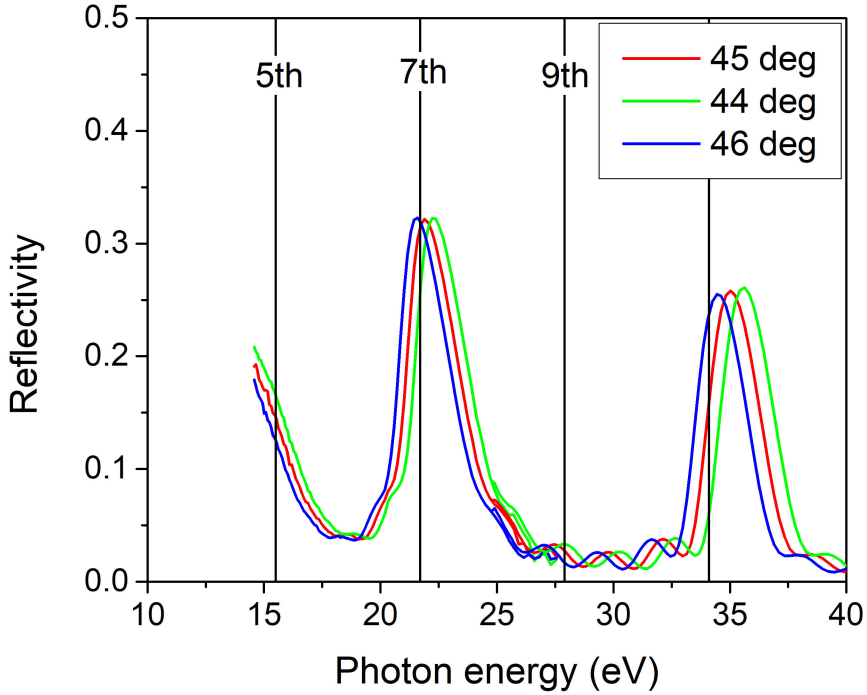

Figure 2.7: Multilayer mirror reflectivity

congestion (see Chapter 1 for a more thorough discussion). Selection of a single harmonic is done by using a multi-layer mirror.

Multi-layer mirrors work by using alternating layers of dielectric coatings to effectively reflect only a specific bandwidth. For our applications, we want this bandwidth to include only one harmonic with an efficient suppression of neighboring harmonics. The mirror in our beamline was designed by Eric Gullikson at LBNL and is made of alternating Mg/SiC layers. The reflection curve is shown in Figure 2.7 with the 5th, 7th, and 9th harmonic of 400 nm shown as vertical lines. This mirror was designed to specifically reflect the 7th harmonic at 21.7 eV and suppress the 5th and the 9th. As is shown, this mirror has relatively high reflectance at the 7th harmonic and almost complete suppression of the 9th harmonic. The 5th harmonic has a non-negligible reflectance, but is largely suppressed by our Al foil filter upstream (see Figure 2.6). This results in an isolated XUV beam at 21.7 eV.

The final chamber before the sample is the annular mirror chamber. This chamber is used to recombine the XUV beam with our pump beam(s). An annular mirror is centered in this chamber which was made by drilling a 5 mm hole into the center of a polished UV fused

silica substrate to which a UV-enhanced aluminum coating is then added (PALU-B-1025-5mmD-Hole-S1/45, Lattice Electro Optics). This mirror was chosen as it has relatively high reflectivity over a broad range of wavelengths, allowing us to change wavelengths without replacing this optic. The XUV beam passes through the center of this optic and the other beams reflect off of the top after entering vacuum through a window. This non-colinearly recombines the beams onto the jet. Care must be taken to make sure all of the XUV beam is making it through the hole as it can otherwise significantly limit the flux. It is estimated that the beam will have an 3.6 mm beam waist at this point, so the alignment procedure is quite sensitive.

After the annular mirror, a retractable XUV photodiode (Opto Diode, 507-065) is installed in the beamline. This can be used for measuring total XUV flux just before entering the jet chamber, a useful measurement since there are multiple optics after the beam analyzer. When everything is aligned well, we get approximately 100 nJ of 21.7 eV light incident onto our sample.

White Light TOPAS and NirUVis

The last portion of the Astrella output, around 1.05 W, is coupled to a Light Conversion White-Light TOPAS-Prime system with a NirUVis extension. This can generate a wide variety of wavelengths, but we primarily use it to produce UV light in the 235 – 260 nm range. Optical parametric amplification will be described briefly below; many of the ideas covered require a knowledge of how nonlinear optics work which is provided in the previous sections.

The first step of optical parametric amplification is optical parametric generation (OPG). The input beam (called the pump) first undergoes a non-linear process to generate two new beams, the signal and the idler[9]. This process involves one photon downconverting into two new photons and follows energy conservation.

$$\omega_p = \omega_s + \omega_i \tag{2.21}$$

where the subscripts p, s, and i stand for pump, signal, and idler, respectively. The idler is the pulse with the longer wavelength by convention. The exact energy of these two beams is tunable and can be controlled by changing the axis of the nonlinear crystal.

The second stage is then optical parametric amplification. This is done by putting the pump beam and the signal beam through a non-linear crystal. This process weakens the pump beam and amplifies the signal beam, producing more idler beam as well. The signal beam from OPG is usually quite weak and not collimated, so this amplification process is

[9]Note that this process is slightly different in our TOPAS, as described later in this section

wavelength	optimized power
235 nm	2 mW
240 nm	6 mW
245 nm	9 mW
250 nm	9 mW
255 nm	10 mW
260 nm	8 mW

Table 2.3: Optimized powers of UV light generated in our TOPAS.

necessary to create a useful beam.

In our experimental setup, we generate the initial signal beam using white-light generation instead of OPG. A small portion of the input beam is split into two parts; one travels through a sapphire plate to generate a white light continuum, and the other is time delayed and then non-colinearly recombined with the white light onto a BBO crystal, generating the desired IR wavelength that we want to amplify. This signal is then recombined with the pump beam and amplified as described above. All non-linear crystals and delay stages are controlled by a computer and are optimized for the generation of different signal wavelengths.

Once the signal beam is amplified it is sent into the NirUVis extension and encounters another BBO crystal along with the pump beam to generate visible light through sum frequency generation. After appropriate filtering, the visible beam passes through another BBO crystal where the second harmonic is generated, making the UV light we use in our experiment. The final UV wavelength is controlled by changing the wavelength of the initially generated signal beam by moving delay stages and rotating crystals in the TOPAS unit. This is all done with a nearby PC that controls these parameters. Optimized (maximum) powers for the wavelength range of 235 – 260 nm are given in Table 2.3. In practice, we get around 70 – 80% of this power due to low Astrella output. Additionally, since the SFG line, the TOPAS line, and the XUV line all have different beam paths, the optimal compression from the Astrella is different for each of them. The compression is set to a compromise between the compression that maximizes the power of each of the beams used in a given experiment. This could be fixed by installing chirped mirrors in two of the beam lines, but it is largely just adding complexity for little gain since all of our beamlines have more than sufficient flux.

References

(1) Faubel, M.; Schlemmer, S.; Toennies, J. P. A molecular beam study of the evaporation of water from a liquid jet. *Zeitschrift für Physik D Atoms, Molecules and Clusters* **1988**, *10*, 269–277.

(2) Faubel, M.; Siefermann, K. R.; Liu, Y.; Abel, B. Ultrafast soft X-ray photoelectron spectroscopy at liquid water microjets. *Accounts of Chemical Research* **2012**, *45*, 120–130.

(3) Smith, J. D.; Cappa, C. D.; Drisdell, W. S.; Cohen, R. C.; Saykally, R. J. Raman Thermometry Measurements of Free Evaporation from Liquid Water Droplets. *Journal of the American Chemical Society* **2006**, *128*, 12892–12898.

(4) Wilson, K. R.; Rude, B. S.; Smith, J.; Cappa, C.; Co, D. T.; Schaller, R. D.; Larsson, M.; Catalano, T.; Saykally, R. J. Investigation of volatile liquid surfaces by synchrotron x-ray spectroscopy of liquid microjets. *The Journal of Chemical Physics* **1997**, *106*, 174506.

(5) Shreve, A. Photoelectron Spectroscopy of Solvated Electrons in Liquid Microjets, Ph.D. Thesis, Berkeley: UC Berkeley, 2012.

(6) Kruit, P.; Read, F. H. Magnetic field paralleliser for 2π electron-spectrometer and electron-image magnifier. *J. Phys. E: Sci. Instrum* **1983**, *16*, 313–324.

(7) Rijs, A. M.; Backus, E. H.; De Lange, C. A.; Westwood, N. P.; Janssen, M. H. 'Magnetic bottle' spectrometer as a versatile tool for laser photoelectron spectroscopy. *Journal of Electron Spectroscopy and Related Phenomena* **2000**, *112*, 151–162.

(8) Griffiths, D. J., *Introduction to Electrodynamics*, 4th ed.; Cambridge University Press: 2017.

(9) Gys, T. Micro-channel plates and vacuum detectors. *Nuclear Instruments and Methods in Physics Research Section A: Accelerators, Spectrometers, Detectors and Associated Equipment* **2015**, *787*, 254–260.

(10) Ladislas Wiza, J. Microchannel plate detectors. *Nuclear Instruments and Methods* **1979**, *162*, 587–601.

(11) Elkins, M. Dynamics of Electron Relaxation Studied Using Time-Resolved Photoelectron Spectroscopy in Liquid Microjets, Ph.D. Thesis, Berkeley: UC Berkeley, 2015.

(12) Jordan, I.; Jain, A.; Gaumnitz, T.; Ma, J.; Jakob, H.; Orner, W. ¨. Photoelectron spectrometer for liquid and gas-phase attosecond spectroscopy with field-free and magnetic bottle operation modes. *Review of Scientific Instruments* **2018**, *89*, 53103.

(13) Williams, H. Ultrafast Dynamics of Adenine Derivatives Studied by Time-Resolved Photoelectron Spectroscopy in Water Microjets, Ph.D. Thesis, Berkeley: UC Berkeley, 2017.

(14) Van Stokkum, I. H.; Larsen, D. S.; Van Grondelle, R. Global and target analysis of time-resolved spectra. *Biochimica et Biophysica Acta - Bioenergetics* **2004**, *1657*, 82–104.

(15) Knutson, J. R.; Walbridge, D. G.; Brand, L. Decay-Associated Fluorescence Spectra and the Heterogeneous Emission of Alcohol Dehydrogenase1. *Biochemistry* **1982**, *21*, 4671–4679.

(16) Elkins, M. H.; Williams, H. L.; Neumark, D. M. Dynamics of electron solvation in methanol: Excited state relaxation and generation by charge-transfer-to-solvent. *Journal of Chemical Physics* **2015**, *142*, 234501.

(17) Hendler, R. W.; Shrager, R. I. Deconvolutions based on singular value decomposition and the pseudoinverse: a guide for beginners. *Journal of Biochemical and Biophysical Methods* **1994**, *28*, 1–33.

(18) Marciniak, H.; Lochbrunner, S. On the interpretation of decay associated spectra in the presence of time dependent spectral shifts. *Chemical Physics Letters* **2014**, *609*, 184–188.

(19) Shlens, J. A Tutorial on Principal Component Analysis. *arXiv:1404.1100v1* **2014**.

(20) Boyd, R. W., *Nonlinear Optics*, 3rd ed.; Academic Press: 2008.

(21) Center for X-ray Optics filter transmission.

Chapter 3

Relaxation Dynamics of Hydrated Thymine, Thymidine, and Thymidine Monophosphate Probed by Liquid Jet Time-Resolved Photoelectron Spectroscopy

Blake A. Erickson, Zachary N. Heim, Elisa Pieri, Erica Liu, Todd J. Martinez, and Daniel M. Neumark. J. Phys. Chem. A 2019, 123, 50, 10676–10684.

The relaxation dynamics of thymine and its derivatives thymidine and thymidine monophosphate are studied using time-resolved photoelectron spectroscopy applied to a water microjet. Two absorption bands are studied; the first is a bright $\pi\pi^*$ state which is populated using tunable-ultraviolet light in the range 4.74 – 5.17 eV and probed using a 6.20 eV probe pulse. By reversing the order of these pulses, a band containing multiple $\pi\pi^*$ states is populated by the 6.20 eV pulse and the lower energy pulse serves as the probe. The lower lying $\pi\pi^*$ state is found to decay in ∼400 fs in both thymine and thymidine independent of pump photon energy, while thymidine monophosphate decays vary from 670 to 840 fs with some pump energy dependence. The application of a computational quantum mechanical/molecular mechanical scheme at the XMS-CASPT2//CASSCF/AMBER level of theory suggests that conformational differences existing between thymidine and thymidine monophosphate in solution account for this difference. The higher lying $\pi\pi^*$ band is found to decay in ∼600 fs in all three cases, but it is only able to be characterized when the 5.17 eV probe pulse is used. Notably, no long-lived signal from an $n\pi^*$ state can be identified in either experiment on any of the three molecules.

3.1 Introduction

DNA strongly absorbs ultraviolet (UV) light, but shows very small rates of damage subsequent to this absorption. [1–5] Understanding the mechanism by which DNA disposes of this excess energy is a crucial element of photobiology. Because of the complexity of DNA strands, many laboratories have undertaken a "bottom-up" approach to the elucidation of these dynamics by investigating smaller nucleic acid (NA) constituents such as nucleobases, nucleosides, and nucleotides. [6] While many of these studies have been performed on isolated gas phase molecules [7], the ability of NA constituents to dissipate excess energy into the surrounding solvent environment (namely, water) is of particular interest. [8] To this end, we have investigated the relaxation dynamics of aqueous thymine (T), thymidine (Thd), and thymidine monophosphate (TMP) by time-resolved photoelectron spectroscopy (TRPES) of liquid water microjets, focusing on excitation of absorption bands at 4.74 – 5.17 and 6.20 eV.

T and its derivatives show strong absorption features at ∼265 and ∼205 nm (4.68 and 6.05 eV) in water. [9–11] These bands exhibit little change going from the nucleobase to the nucleotide, indicating these excitations are likely localized to the nucleobase itself. [12] The assignment of the absorption spectrum has been considered in numerous studies on the electronic structure of thymine [13–16] that are well-reviewed by Improta et al. [5] This body of work shows that, in isolated T, the lower energy absorption band corresponds to a $\pi\pi^*$ highest occupied molecular orbital (HOMO) $\rightarrow$ lowest unoccupied molecular orbital (LUMO) transition while the optically dark $n\pi^*$ (HOMO – 1) $\rightarrow$ LUMO transition lies lower in energy. In water, the $\pi\pi^*$ state is stabilized while the $n\pi^*$ state is destabilized [17], causing the $\pi\pi^*$ and $n\pi^*$ states to be neardegenerate. The higher lying absorption band at ∼205 nm also appears to be of $\pi\pi^*$ character based on comparison to gas phase results [5], and recent calculations indicate that multiple $\pi\pi^*$ transitions contribute to this band in liquid water.[11] For convenience, the ground state will be referred to as S_0 and the higher lying band will be referred to as S_n to distinguish it from the lower lying $\pi\pi^*$ state.

Photodeactivation of the first $\pi\pi^*$ state has been studied in T in the gas phase using time-resolved photoionization [18–20], photoelectron spectroscopy (TRPES) [21, 22], and X-ray transient absorption. [23] These experiments find a subpicosecond decay component that is most often attributed to relaxation through a conical intersection (CI) connecting the initially populated $\pi\pi^*$ state and the lower energy $n\pi^*$ state. A recent TRPES experiment using an extreme ultraviolet (XUV) probe energy [24] has found that the population in the $n\pi^{**}$ state is then transferred to a $^3\pi\pi^*$ state in a few picoseconds, although there is still some contention on this point. Theoretical investigations largely agree on this mechanistic picture of relaxation for isolated T. [22, 25, 26]

Since the relative energies of the states change upon solvation such that the $n\pi^*$ state is similar to or higher in energy than the $\pi\pi^*$ state, it remains to be seen whether this state is still involved in the relaxation process when solvated. The relaxation mechanism of T and,

in some cases, Thd and TMP, have been studied in liquid water by fluorescence upconversion (FU) [27, 28], ultraviolet/visible and infrared transient absorption (TA) [29–33], and TRPES. [34] FU studies have fit the decays of all three species to a single lifetime attributed to direct relaxation from $\pi\pi^* \rightarrow S_0$. In contrast, the TA studies generally find two decay lifetimes: a subpicosecond decay that corresponds to direct repopulation of the ground state, and an additional multiple picosecond decay that has most often been attributed to the $n\pi^*$ state. A bifurcation is seen in the signal with the majority directly going from $\pi\pi^* \rightarrow S_0$, with the remainder proposed to be relaxing by $\pi\pi^* \rightarrow n\pi^* \rightarrow S_0$. Although this discrepancy is far from settled, a recent calculation suggests that population transfer from $\pi\pi^* \rightarrow n\pi^*$ is significantly weaker in water than in isolated T and changes drastically with small changes in the energy gap between the two states. [35]

The relaxation dynamics of nucleic acid constituents in aqueous solution have recently been addressed in a series of TRPES experiments on liquid water microjets. [34, 36–38] These jets enable the study of bulk aqueous solutions under vacuum using single photon [39, 40] and time-resolved [41, 42] photoelectron spectroscopies, techniques that were previously restricted to gas-phase studies. Lübcke and co-workers [34] have carried out liquid jet TRPES on T and Thd. They find biexponential decay on two subpicosecond time scales and attribute both of these decay channels to $\pi\pi^* \rightarrow S_0$ direct relaxation along different pathways on the $\pi\pi^*$ surface. Notably, no long-lived signal was seen, which could indicate the absence of the $n\pi^*$ state being on the decay pathway or insufficient probe energy to photoionize the state. Calculations in that work suggested that the probe energy (5.20 eV) should have been high enough to see photoemission from the $n\pi^*$ state, but there are other excited states, such as the $^3\pi\pi^*$ state, that have binding energies greater than 5.20 eV that would not be visible to their experiment. [17]

In this work, TMP is studied by liquid microjet TRPES for the first time, along with T and Thd. A higher probe energy of 6.20 eV is used, compared to previous liquid jet work on T and Thd where the maximum probe energy was 5.20 eV. [34] As will be discussed, this ensures that ionization from all singlet excited states is energetically accessible and provides more insight into the possible role of the $n\pi^*$ state in the relaxation of T, Thd, and TMP. Finally, relaxation from the second absorption band at 6.20 eV is studied for the first time in all three molecules by reversing the pump pulse and the probe pulse, showing new decay pathways along multiple excited state surfaces for the first time. Interpretation of the results, particularly differences between TMP and the other two molecules, is aided by molecular dynamics simulations.

3.2 Methods

The apparatus used in these experiments has been described in detail previously. [38, 43–47] Briefly, two femtosecond laser pulses cross a liquid water microjet in which the species of interest is dissolved. Photoelectrons ejected from the jet are analyzed using a magnetic bottle time-of-flight (ToF) analyzer. The overall experiment is summarized as follows:

$$T \xrightarrow{h\nu_1} T^* \xrightarrow{\Delta t, h\nu_2} T^+ + e^-(eKE) \tag{3.1}$$

In the positive delay direction, a tunable UV pump pulse (4.74 – 5.17 eV), $h\nu_1$, electronically excites the nucleic acid constituent and a 6.20 eV probe pulse, $h\nu_2$, photoionizes the excited species. A variable delay time Δt is applied between the two pulses which allows the collection of time-resolved data. In the negative delay direction, the 6.20 eV pulse arrives first and the tunable UV serves as the probe. Thymine (Sigma-Aldrich, 10 mM), thymidine (United States Biochemical Corp., 10 mM), and thymidine monophosphate (Sigma-Aldrich, 7 mM) were dissolved in water buffered at pH 8 with Trizma HCl (2 mM, Sigma-Aldrich), and NaCl (100 mM, Sigma-Aldrich) was added to reduce the streaming potential. These samples were introduced to a vacuum through a 20 μm capillary with a flow rate of 0.2 mL/min. At the point of probing, our jet is calculated to be ∼280 K based on Faubel's evaporative cooling model for liquid microjets. [48] The solutions of Trizma HCl and NaCl provided no time-resolved signal as is shown in Figure A4 in the Supporting Information.

A Ti:sapphire laser (Coherent Astrella) generated 35 fs, 7 mJ pulses centered at 800 nm at a 1 kHz repetition rate. Approximately 1 mJ of this beam was directed into a Light Conversion TOPAS-Prime optical parametric amplifier with an NIRUVis extension to generate the tunable UV pulses (4.74 – 5.17 eV). Also, 1 mJ was sent into a β–barium borate (BBO) based sum frequency generation line to generate the fourth harmonic of the fundamental laser output (6.20 eV). The energy of each pulse was set between 20 and 50 nJ as measured directly before entering the liquid jet vacuum chamber. The pulse durations were measured as a cross-correlation, or instrument response function (IRF), between the two pulses that was found to be ∼160 fs by 2 + 1 resonantly enhanced multiphoton ionization of Xe using 5.00 and 6.20 eV pulses, respectively. The actual IRF for each experiment was fit with the data as it was found to change daily and with tunable UV energy. The cross-correlation is dependent on the photon energy produced by the optical parametric amplifier as no compression is done after generation. The tunable UV light passed through a delay stage (Newport, ILS150PP) that was variably delayed from the other pulse from –3.0 to 4.5 ps. Scans were performed taking 1000 shots at each delay before moving the stage and static two-photon, one-color backgrounds were taken after each scan of delays with the stage set to a 0 ps delay.

The ejected photoelectrons were directed into the magnetic bottle ToF spectrometer through a 900 μm diameter skimmer located 1 mm from the jet by a 1.1 T rare earth magnet stack composed of SmCo/Nd disk magnets, and then guided through a 66 cm flight tube

by an axial 10 G field from a solenoid. Photoelectrons were detected by a microchannel plate (MCP) stack with a phosphor screen. The arrival times of the electrons were recorded by capacitively coupling the current off of the back MCP as a function of time after the probe pulse hits the jet. The phosphor screen image was used for alignment of the magnetic bottle.

The spectrum measured at each delay was background subtracted from the one-color, two-photon spectra. The ToF distribution measured by the spectrometer was converted to electron kinetic energy (eKE). Global lifetime analysis (GLA) was used to fit the spectra and lifetimes using a minimum number of kinetic components. [46, 49, 50]

In brief, GLA can fit a time-resolved data set according to the following equation:

$$S(eKE, \Delta t) = \sum_{i=1}^{n} DAS_{\tau_i}(eKE)[e^{-t/\tau_i} L(t - \Delta t)] \tag{3.2}$$

Equation 3.2 permits the determination of spectra and lifetimes of time-resolved data. Two assumptions are involved. (1) Spectral components shift only in intensity, not in energy. This allows the separability of the components dependent on eKE and the kinetics of the corresponding component which depend on pump-probe delay. (2) The kinetics can be expressed as a simple sum of monoexponential decays, thereby enabling data to be represented as a sum of exponentials and the IRF mentioned earlier, $L(t - \Delta t)$, multiplied by an energy dependent term called the decay associated spectrum (DAS_{τ_i}) and a time constant $\tau_i = 1/k_i$.

Numerical simulations were performed to elucidate the mechanism behind the observed signals. For all three of the target species (T, Thd, TMP), we carried out 100 ns of molecular dynamics including the aqueous solvent at 300 K with the AMBER FF14SB and SPC force fields (see the Supporting Information for full details). For each of the three target species, a clustering analysis based on root-mean-square deviation of the solute was used to obtain the most likely solute geometries and to guide further sampling. We then extracted 1000 snapshots from each molecular dynamics trajectory, under the constraint that the relative population of different clusters followed that found in analysis of the 100 ns trajectory. Absorption spectra were calculated by histogramming the energy gaps obtained from these 1000 snapshots using quantum mechanics/molecular mechanics (QM/MM) with CASSCF(8/6) and the 6-31G* basis set for the solute and the SPC force field for surrounding water molecules. We further selected 100 snapshots for each molecule to compute the QM/MM absorption spectra with XMS-CASPT2(8/7) in the 6-31G* basis set for the solute. Details on the computational methods can be found in the Supporting Information.

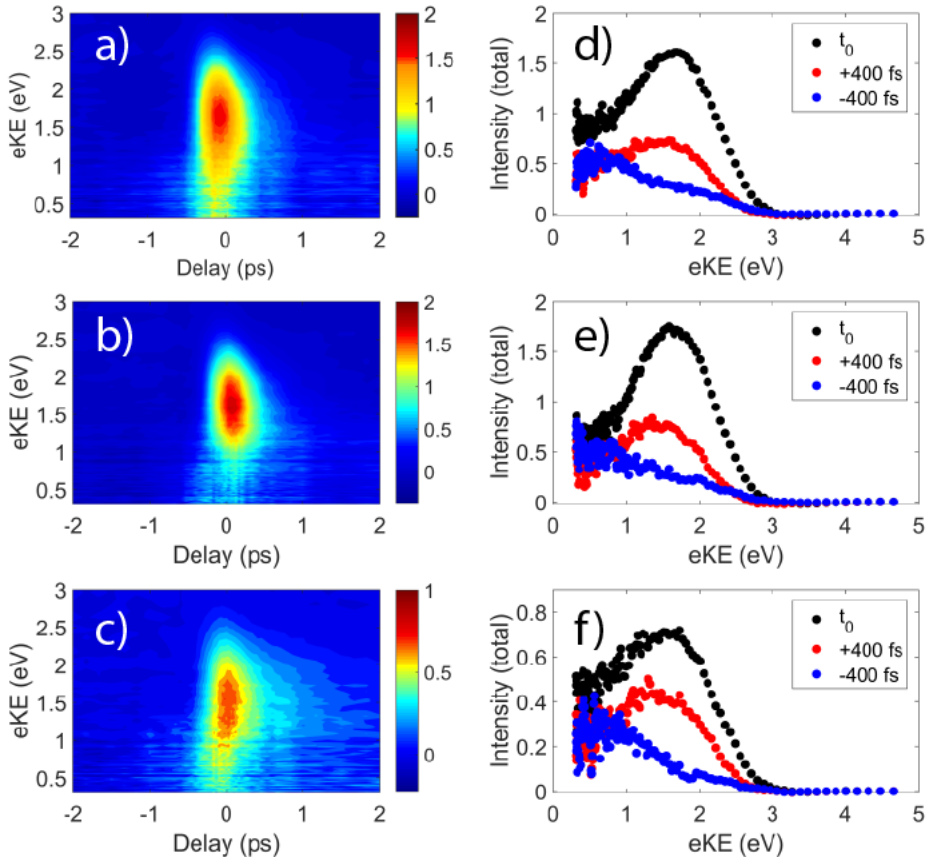

Figure 3.1: Processed data for 4.95/6.20 eV (positive delays) and 6.20/4.95 eV (negative delays) experiments. (a – c) Filled contour plots for T, Thd, and TMP. (d – f) Select lineouts to show the two features. Peak A is in red and peak B is in blue. The black trace shows when the two pulses are overlapped in time.

3.3 Results

Time-resolved photoelectron spectra of T, Thd, and TMP are presented in Figures 1a – c and 2a – c. The data presented were taken at pump photon energies of 4.95 and 5.17 eV, respectively, and a 6.20 eV probe photon energy. Results at 4.74 eV pump photon energy, which are quite similar to the spectra in Figure 3.1, are shown in Figure A1. The role of the pump and probe pulses is reversed at negative times, in which case the pump photon energy is 6.20 eV.

The spectra in Figure 3.1 are asymmetric with respect to t_0, showing decays in the positive delay direction and very little signal in the negative delay direction. All three of the spectra are peaked at eKE ∼1.5 eV. For T and Thd, most of the signal decays completely

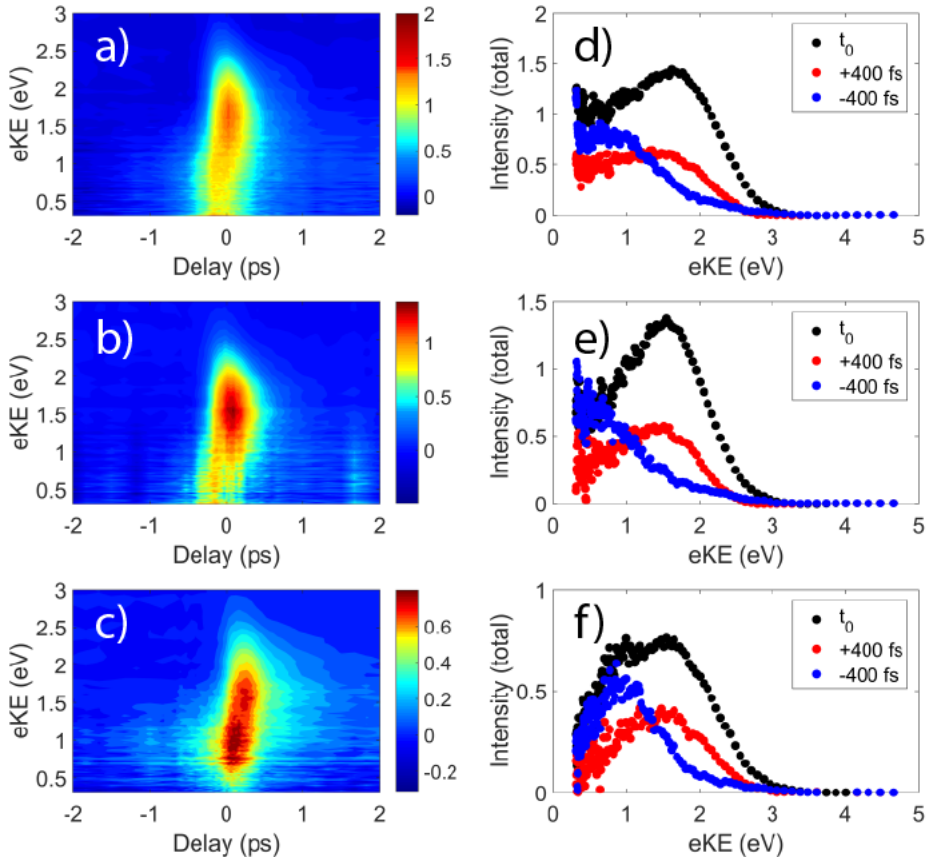

Figure 3.2: Processed data for 5.17/6.20 eV (positive delays) and 6.20/5.17 eV (negative delays) experiments. (a – c) Filled contour plots for T, Thd, and TMP. (d – f) Select lineouts to show the two features. Peak A is in red and peak B is in blue. The black trace shows when the two pulses are overlapped in time.

within ∼0.75 ps, while TMP shows a longer lived signal that persists until ∼1.5 ps. The spectra of T, Thd, and TMP in Figure 3.2 are similar to those in Figure 3.1 for positive time delays but show significantly different behavior for negative time delays, with a signal peaked below 1 eV persisting beyond –0.5 ps. As in Figure 3.1, signal from TMP lasts noticeably longer compared to T or Thd; in Figure 3.2 this occurs in both the positive and negative directions.

To analyze these features further, spectral lineouts were taken at selected delays and are shown in Figures 1d – f and 2d – f. Lineouts were taken at t_0 (i.e., zero pump-probe delay) as well as at +400 and –400 fs, where any contributions from pump-probe overlap should be negligible. In the positive direction, there is a peak located at ∼1.5 eV (referred to as peak A and shown in red) for all three species, whereas in the negative direction there is

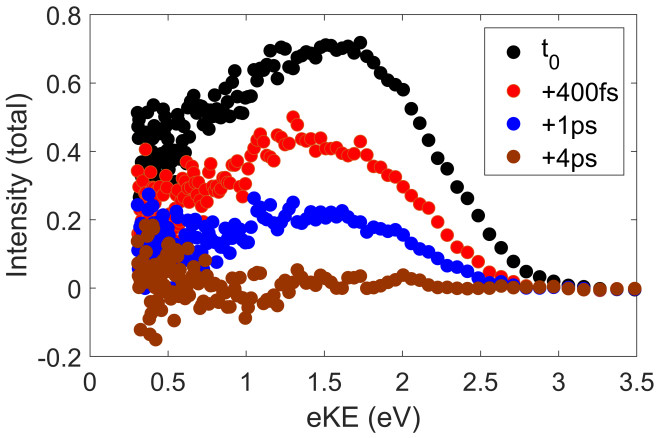

Figure 3.3: Select lineouts shown for the 4.95/6.20 eV experiment in TMP. The signal is found to decay completely within a few picoseconds with no emergence of a new signal at long times.

a peak located at ∼0.8 eV (referred to as peak B and shown in blue). Peak B is stronger and persists much longer when probing at 5.17 eV compared to 4.95 eV, and is particularly noticeable for TMP at 5.17 eV. Select lineouts out to 4 ps for the 4.95/6.20 eV experiment on TMP are shown in Figure 3.3. These lineouts show the evolution of peak A in the long time limit.

The maxima in the eKE distributions for features A and B are ∼1.5 and ∼0.8 eV, respectively, and are the same for each of the three species studied. The vertical detachment energies (VDEs) of features A and B, calculated as the difference between the probe photon energy and the peak of the eKE distribution measured, are found to be ∼4.7 and ∼4.4 eV, respectively. These values are quite close, indicating that both features reflect photodetachment from the same state: the lowest energy $\pi\pi^*$ state. Features A and B do not shift significantly on the time scale of the experiment, but they do overlap around t_0.

Because of the overlap, the results for T, Thd, and TMP were fit using the GLA routine described under Methods. The comparison between the GLA fit and the total integrated signal is shown in parts a and b of Figure 3.4 for TMP for 4.95 and 5.17 eV, respectively, plotted as a function of the delay. For 4.74/6.20 and 4.95/6.20 eV experiments, only one kinetic component in the positive direction was needed to fit the data. There is some signal that is not reproduced in the negative direction, but it is too weak to fit reliably. For the 5.17/6.20 eV experiments, two kinetic components were required to fit the data, one in the positive delay direction andone in the negative delay direction.

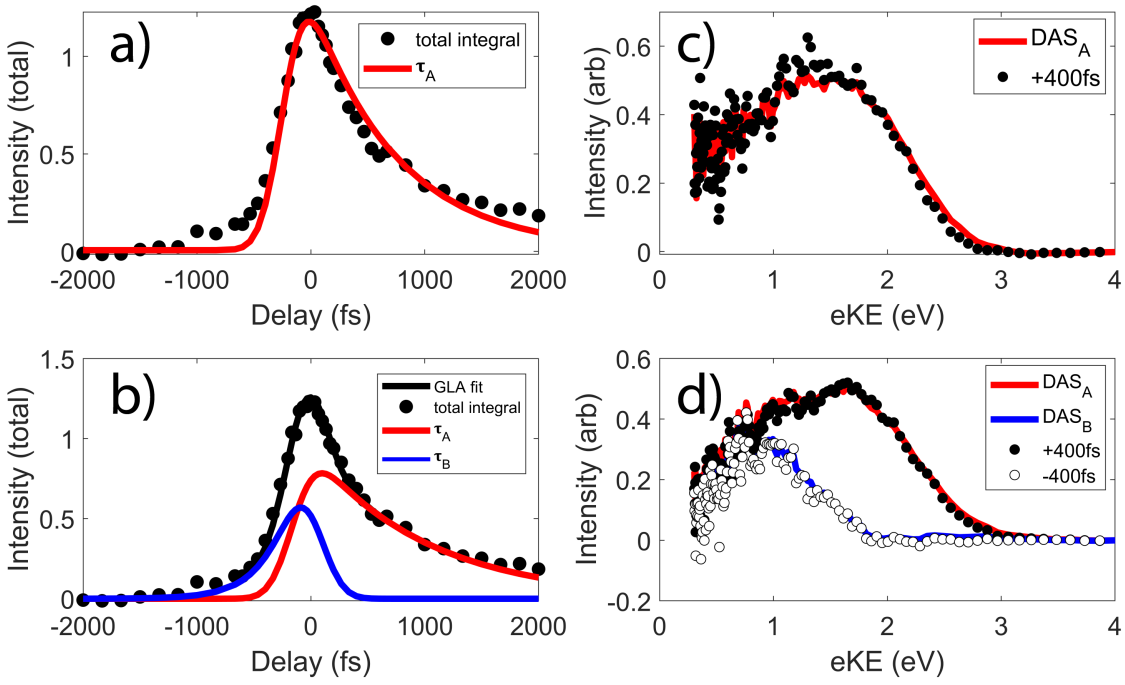

Figure 3.4: (a, b) Comparison between the GLA fits for the 4.95/6.20 and 5.17/6.20 eV experiments for TMP, respectively. In the 4.95/6.20 eV experiment only one decay is found in the positive direction, while two decays are found in the 5.17/6.20 eV experiment. (c, d) Comparison between the DAS and lineouts at +400 fs in the 4.95/6.20 eV experiment and ±400 fs in the 5.17/6.20 eV experiments.

The normalized DAS are shown in Figure 3.4c,d for TMP. These DAS are compared to scaled lineouts at +400 fs in the case of the 4.95 eV pump and ±400 fs in the case of the 5.17 eV pump. These lineouts are chosen as they are representative of the VDEs of the states from which relaxation is occurring as they lie significantly outside of the IRF, but still within the lifetime of the state. Since the DAS match well with the lineouts, the GLA routine accurately fits the decay components in both directions.

GLA was used to extract fitted lifetimes which are shown in Table 3.1 for T, Thd, and TMP. For each kinetic component, the functional form used was a single exponential decay convolved with a Gaussian IRF and a Heaviside function. The form of this expression is shown in the Supporting Information (Equation A1). Error bars were generated with the use of a support plane analysis and are reported at the 95% confidence interval.

QM/MM CASSCF calculations in solution (see Figure A5 in the Supporting Information) of the vertical excitation energies of the two lowest lying excited states show that the nature

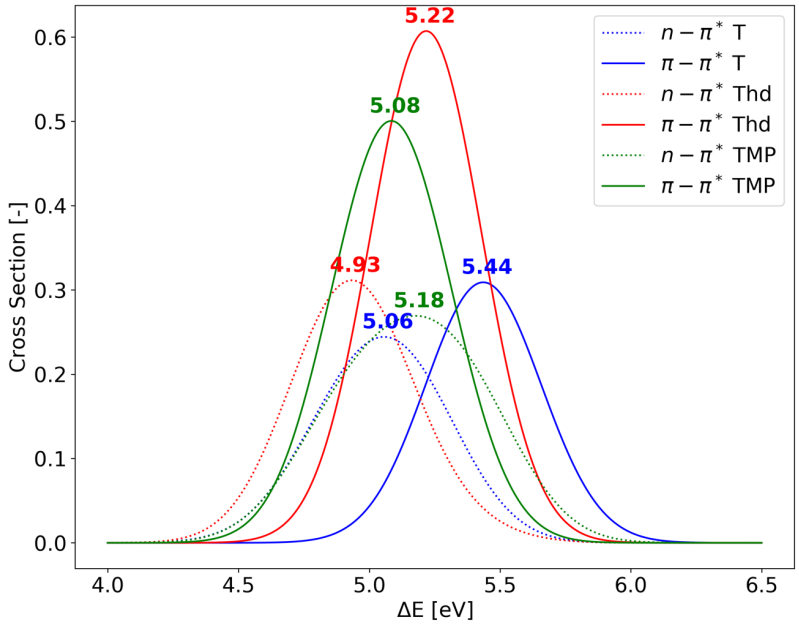

Figure 3.5: Absorption spectra of T (in blue), Thd (in red), and $TMP^{(-1)}$ (in green) calculated using QM/MM with XMS-CASPT2-(8/7)/6-31G*. The spectra were obtained through the procedure described in the Supporting Information; since the $n\pi^*$ oscillator strength is close to zero, it has been multiplied by 500 in order to compare the two excited state energies (the predicted absorption spectrum would consist only of the solid lines). The experimental absorption maxima are 4.68 eV for both T and Thd, compared to 5.02 and 5.08 eV from the calculations, respectively.

of the first excited state is $n\pi^*$, with an oscillator strength close to zero. The lowest bright state is the second excited state, featuring a $\pi\pi^*$ character. At the CASSCF level, the energy difference between these two states is quite large: 2.04 eV for T, 1.88 eV for Thd, and 1.90 eV for TMP. After including dynamic correlation with XMS-CASPT2 (see Figure 3.5), the $n\pi^*$ and $\pi\pi^*$ states become near-degenerate. The average $n\pi^*/\pi\pi$ energy difference is found to be 0.46 eV in T and 0.28 eV in Thd, but the two states get so close in TMP that we observe a swap in ∼55% of the cases, and the average $n\pi^*/\pi\pi$ energy difference falls to 0.15 eV.

3.4 Discussion

Relaxation from the $\pi\pi^*$ State. The first $\pi\pi^*$ state is accessed through direct absorption by the tunable-UV pulses used in this experiment (4.74 – 5.17 eV) and decays within ∼400

		τ (fs)		
pump (eV)	**probe (eV)**	T	Thd	TMP
4.74	6.20	360^{+60}_{-60}	390^{+70}_{-60}	870^{+180}_{-130}
4.95	6.20	390^{+60}_{-70}	410^{+70}_{-110}	840^{+60}_{-190}
5.17	6.20	410^{+140}_{-20}	430^{+20}_{-130}	610^{+140}_{-50}
6.20	5.17	650^{+470}_{-300}	590^{+260}_{-390}	550^{+290}_{-100}

Table 3.1: Fitted Lifetimes of DAS_A (Tunable UV Pump) and DAS_B (6.20 eV Pump) for T, Thd, and TMP with Energies Ranging from 4.74 to 6.20 eV[1]

fs for both T and Thd while showing no pump energy dependence and almost no difference between the two molecules. We can directly compare our 4.74/6.20 eV experiments to those of Lübcke and co-workers at 4.66/5.21 eV. [34] Our lifetimes of 360^{+60}_{-60} and 390^{+70}_{+60} fs for T and Thd, respectively, are within error of the previous lifetimes of 410 ± 80 and 390 ± 20 fs. Note that the error bars here have been extended to the 95% confidence interval for Lübcke's work for a direct comparison. Extending the probe photon energy from the previous TRPES study clarifies that the measured time constants in that work were not limited by the accessibility of the Franck-Condon window; otherwise we would observe a longer $\pi\pi^*$ lifetime at our higher probe photon energy. Interestingly, the lifetimes in both TRPES experiments are somewhat shorter than those measured by TA (540 ± 40 fs) [29] or FU (470 ± 10 or 633 ± 18 fs). [28, 51]

Although the lifetimes in T and Thd reported here appear to increase as the pump energy is raised, these differences are not significant in light of the error bars. A similar situation was seen in liquid jet studies of adenosine (Ado), where there was a slight decrease in lifetime with increasing pump energy that was also within error bars.[36, 38] However, what does differ from adenine and its derivatives are the lifetimes themselves, which are notably longer for T (Thd) than for A (Ado): ∼360 (390) fs compared to ∼200 (250) fs. [29, 36, 38, 52–54] This difference may arise simply from a flatter reaction coordinate leading to the CI for the thymine compounds, or from differing dynamics at the relevant CIs.

Despite the similarities in the absorption spectra of the three molecules, relaxation from the $\pi\pi^*$ state is quite different in TMP than in T and Thd. We find that TMP shows $\pi\pi^*$ lifetimes between 610 and 870 fs compared to ∼400 fs in T and Thd. Moreover, the TMP lifetime drops considerably (from 840 to 610 fs) when the pump energy is increased from 4.95 to 5.17 eV. Our values are close to those of Onidas et al. [28], who measured lifetimes of 680

[1]Note that the lifetime in the experiments with a 6.20 eV pump and 4.74 and 4.95 eV probes was unable to be fit and was not included in this table. The error bars presented represent the 95% confidence interval.

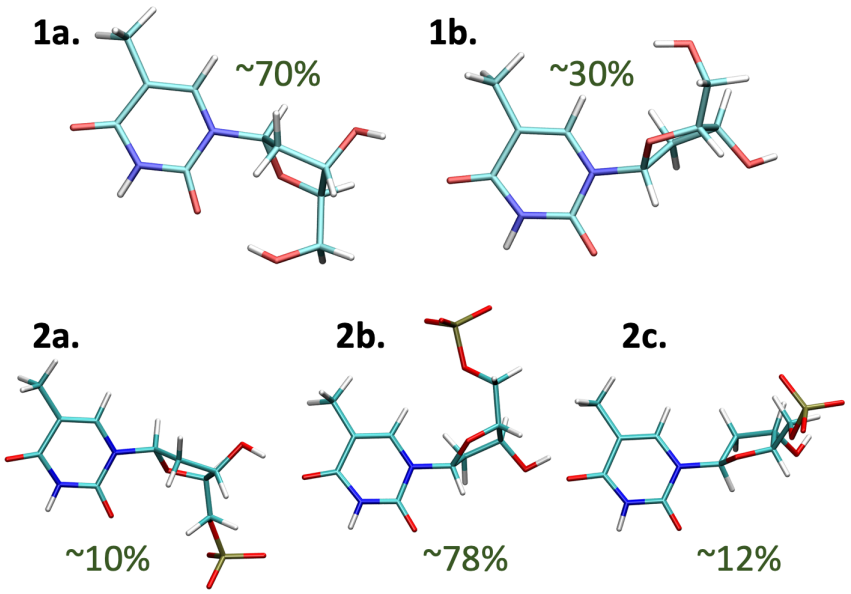

Figure 3.6: Main conformations of Thd (1a and 1b) and TMP (2a, 2b, and 2c) along a 100 ns MM trajectory, with the corresponding percentage of occupation.

$\pm$ 20 fs for TMP and 470 $\pm$ 10 fs for Thd at pump energies of 4.64 and 4.59 eV, respectively. Peon et al.[27] found lifetimes of 980 $\pm$ 120 fs for TMP and 700 $\pm$ 120 fs for Thd, although it is worth noting that all of their measured lifetimes are systematically longer than more recent measurements. [28, 30–34] Nonetheless, the trend that TMP has a longer lifetime than T or Thd seems consistent across several experiments.

Indeed, the differences between molecules observed from the analysis of the computed absorption spectrum are too small to justify a remarkably longer excited state lifetime for TMP, especially since the absorption spectra of Thd and TMP are very similar. However, a closer inspection of the molecular conformation along the MM trajectories (using clustering analysis as described in the Supporting Information) reveals a different behavior for Thd and TMP. Two main conformations exist for Thd, which differ in the orientation between the thymine and deoxyribose rings: the molecule spends ~70% of the time in a conformation featuring the $O'_5 - H_{O'_5}$ bond pointing toward O_2 (syn conformation, see 1a in Figure 3.6; for the full atom nomenclature, see Figure A8 in the Supporting Information), while an ~180° rotation around the bond connecting the two rings leads to the conformation that is occupied for the remaining time (anti conformation, 1b in Figure 3.6). The ground state energy difference between the two conformations, according to PBE0/6-31G* calculations using PCM [55], is 2 kcal/mol, with 1a being more stable than 1b, independent of the solvent

dielectric constant (see the Supporting Information for details). The dominance of 1a was also seen in theoretical work by Pepino et al. [11] and is explained by the existence in the syn conformation of the aforementioned hydrogen bond between $O'_5 - H_{O'_5}$ and O_2.

Due to the replacement of the OH group with a phosphate group in TMP, the situation is reversed. The conformation analogous to 1a (i.e., 2a), now featuring no intramolecular hydrogen bonds, is occupied only ∼10% of the time, while the large majority of the trajectory is spent in conformations similar to 1b and differentiated only by the orientation of the phosphate group with respect to the thymine ring (2b and 2c). Indeed, 2c does not correspond to a local minimum on the ground state potential energy surface: optimizing this geometry leads to 2b, i.e., the anti conformation. At the PBE0/6-31G* level of theory, 2b is ∼7 kcal/mol more stable than 2a (see the Supporting Information); these energy results are in agreement with the relative population of the respective conformations obtained from empirical force field based molecular dynamics, both for Thd and for TMP. The energy difference between conformations 2a and 2b increases in an apolar solvent, due to the net charge of the molecule.

These conformational transitions are unlikely to be of relevance in the excited state dynamics, since the simulated time scale of syn – anti conversion is in the tens-of-picoseconds range for both Thd and TMP (see Table A2 for details). This isomerization time scale is much longer than the excited state lifetime for both molecules. Since the isomerization time scales are derived from ground state dynamics, conformational transitions in the excited state dynamics cannot be completely excluded. Nevertheless, we find this possibility unlikely and suggest that any influence of the different conformations is restricted to the dependence of the ensuing excited state dynamics on the initial geometry (syn vs anti). This deserves further exploration, and future studies will concentrate on the influence of the starting conformation on photoexcitation dynamics. We expect that the classical description of intramolecular and solvent-solute hydrogen bonding should be accurate in our simulations, as the employed force field has been chosen for its capacity to optimally describe thermodynamic, structural, and kinetic bulk properties introducing flexibility in the water molecule. [56]

The longer-time dynamics of TMP, displayed in Figure 3.3 for a pump photon energy of 4.95 eV, show that the signal decays substantially in the positive direction and, by 4 ps, all of the signal is gone. This result is also seen for T and Thd, as shown in Figures A2 and A3. The absence of signal beyond 4 ps is of interest in light of previous work based on TA that found a decay component that persists on the order of tens of picoseconds in addition to the subpicosecond decay. [29–32] This long-lived signal has been attributed to trapping in an intermediate $n\pi^*$ state before reaching S_0. As previously mentioned, long-lived signal was also not seen in the previous liquid jet TRPES study on T and Thd [34]; based on calculations indicating that ionization from the $n\pi^*$ state would be accessible at the highest probe energy (5.20 eV) used in that work, the authors concluded that the $n\pi^*$ state did not participate in the dynamics.

Recent gas phase work using TRPES on thymine using an XUV probe at 14 eV has located the $n\pi^*$ state experimentally, showing a feature covering an electron binding energy range of 6 – 7 eV with a vertical ionization energy around 6.5 eV. [24] In water, one expects these values to decrease by about 1 eV owing to favorable hydration of the cation. [40] Under these circumstances, it is possible that the probe energy of 5.20 eV used previously was insufficient to ionize the $n\pi^*$ state (note that ionization from this state to the cation ground state is not possible via a one-electron transition), but the higher probe energy of 6.20 eV used here would certainly be sufficient. Hence there is no evidence for a long-lived $n\pi^*$ in our work, either. It is possible that the photoionization cross section of the $n\pi^*$ state is very small, in which case no signal would be seen from this state in our experiment.

While earlier TA studies [30–32] were fairly confident in their assignment of the $n\pi^*$ state as the reason for a multiple picoseconds signal, a recent experiment [33] instead proposed two long-lived states; a $^3\pi\pi^*$ state and a state of unknown character. The energetics of this triplet state in liquid water have been considered by Pepino et al. [17] They predict the binding energy of the $^3\pi\pi^*$ state to be 5.6 eV, which would enable ionization by our probe laser, but produce low energy (0.6 eV) photoelectrons that are near the lower limit of our detection efficiency. Also, in this same paper, the $^3\pi\pi^*$ state is calculated to lie $\sim$1.3 eV below the $n\pi^*$ state, which would put it out of range of our probe laser based on the estimate of the $n\pi^*$ ionization energy given above. Hence, it is possible that the $^3\pi\pi^*$ state is involved in the overall mechanism but cannot be seen in our experiment. The possible role of the intermediate electronic states in the relaxation of thymine will be explored in planned experiments using higher probe photon energies.

The role of the $n\pi^*$ state in nucleobase relaxation is crucial to understanding DNA damage as this state has been implicated in the formation of unwanted photoproducts and as an intermediate in the formation of the $^3\pi\pi^*$ state. [57] For example, one of the most prominent pathways of DNA damage, thymine dimerization, occurs when covalent bonds are formed between adjacent thymine nucleobases in DNA strands, most commonly as cyclobutane pyrimidine dimers or 6 – 4 photoproducts which are both likely formed through a long-lived intermediate state. [1, 30] Because these long-lived excited states are not observed here in the relaxation of single subunits of T, Thd, or TMP, this excited state trapping process may likely be the result of or enhanced by interaction between bases. This result specifically warrants the study of the TpT dinucleotide, and such studies are planned in the near future.

Relaxation from S_n. Using pump photons at 6.20 eV, the higher lying electronic band of T and its derivatives was populated. Multiple overlapping $\pi\pi^*$ transitions are predicted to contribute to this band [11], and no dynamical studies resulting from its excitation have been carried out prior to this work. Relaxation from this higher lying band is shown in the negative delay direction in all data sets, but can only be fit in the case of the 5.17 eV probe photon energy for all three molecules. As can be seen in comparing Figures 1 and

2, the signal in the negative direction is more intense and persists for longer delays. This likely indicates that probe photon energies below 5.17 eV do not yield sufficiently high eKE for S_n dynamics to be reliably characterized; due to the transformation from ToF to eKE, features below ∼0.5 eV can be quite noisy and hard to fit. In our previous study of Ado and adenosine monophosphate (AMP), relaxation from S_n was seen only for AMP. [38] However, the highest probe energy used in that work was 4.97 eV, the probe energy corresponding to Figure 3.1 in this work.

For T, Thd, and TMP, decay of the S_n signal occurs in ∼600 fs. The decay of S_n for T and Thd appears to be longer than the decay of the lower lying $\pi\pi^*$ state (∼400 fs vs ∼600 fs) although the error bars for the S_n lifetimes are large. A similar trend was seen in AMP. [38] In all cases, the VDEs of the state observed by pumping either the S_n band or the lower $\pi\pi^*$ state are similar, which suggests that excitation at 6.20 eV promotes electrons to S_n, followed by relaxation into the lower lying $\pi\pi^*$ state within the IRF of the pulses used. Photoionization then occurs from the lower lying $\pi\pi^*$ surface. The absence of photoionization signal from the upper band may reflect a lower ionization cross section and/or an extremely short lifetime, as has been observed in other highly excited $\pi\pi^*$ states in TRPES. [58]

Signal from upper band excitation is notably stronger from TMP than from T and Thd, although its lifetime is within error of that from T and Thd. Hence, the relaxation pathway is likely to be similar, but the origin of the stronger upper band signal for TMP (and for AMP) requires additional investigation.

3.5 Conclusions

The relaxation dynamics of thymine (T) and its derivatives thymidine (Thd) and thymidine monophosphate (TMP) were studied using time-resolved photoelectron spectroscopy on a water microjet. Two states are directly populated by ultraviolet absorption in the range 4.74 – 6.20 eV. As confirmed by XMSCASPT2//CASSCF/AMBER calculations, the first absorption band is populated using light in the range 4.74 – 5.17 eV, which corresponds to the lowest lying bright state of $\pi\pi^*$ character, while the 6.20 eV light populates a higher lying band which contains multiple states of $\pi\pi^*$ character. Relaxation from the lower lying $\pi\pi^*$ state occurs in ∼400 fs for both T and Thd and ∼670 – 840 fs in TMP, in general agreement with previous studies. The computational analysis suggests that this difference is linked to conformational differences existing between Thd and TMP, which might influence the topology of the excited state potential energy surface. Notably, no long-lived signal was seen to persist past ∼1.5 ps, indicating that the $n\pi^*$ does not participate in the relaxation process. Excitation to the S_n band appears to result in rapid decay to the lower lying $\pi\pi^*$ state within the duration of the pulses used in the experiment and then back into the ground state.

References

(1) Crespo-Hernández, C. E.; Cohen, B.; Hare, P. M.; Kohler, B. Ultrafast excited-state dynamics in nucleic acids. *Chemical Reviews* **2004**, *104*, 1977–2019.

(2) Shukla, M. K.; Leszczynski, J. Electronic spectra, excited state structures and interactions of nucleic acid bases and base assemblies: A review. *Journal of Biomolecular Structure and Dynamics* **2007**, *25*, 93–118.

(3) Middleton, C. T.; de La Harpe, K.; Su, C.; Law, Y. K.; Crespo-Hernández, C. E.; Kohler, B. DNA Excited-State Dynamics: From Single Bases to the Double Helix. *Annual Review of Physical Chemistry* **2009**, *60*, 217–239.

(4) Barbatti, M., *Photoinduced Phenomena in Nucleic Acids I*; 1; Springer: 2015; Vol. 355, pp 1–65.

(5) Improta, R.; Santoro, F.; Blancafort, L. Quantum Mechanical Studies on the Photophysics and the Photochemistry of Nucleic Acids and Nucleobases. *Chemical Reviews* **2016**, *116*, 3540–3593.

(6) Stavros, V. G.; Verlet, J. R. Gas-Phase Femtosecond Particle Spectroscopy: A Bottom-Up Approach to Nucleotide Dynamics. *Annual Review of Physical Chemistry* **2016**, *67*, 211–232.

(7) Kleinermanns, K.; Nachtigallová, D.; de Vries, M. S. Excited state dynamics of DNA bases. *International Reviews in Physical Chemistry* **2013**, *32*, 308–342.

(8) Kohler, B. Nonradiative decay mechanisms in DNA model systems. *Journal of Physical Chemistry Letters* **2010**, *1*, 2047–2053.

(9) Fox, J. J.; Shugar, D. Spectrophotometric studies on nucleic acid derivatives and related compounds as a function of pH. II. Natural and synthetic pyrimidine nucleosides. *BBA - Biochimica et Biophysica Acta* **1952**, *9*, 369–384.

(10) Wilson, W. Some 2:4-diamino-5-acylamido-6-hydroxypyrimidines. *Journal of the Chemical Society* **1948**, 1157–1161.

(11) Pepino, A. J.; Segarra-Martí, J.; Nenov, A.; Improta, R.; Garavelli, M. Resolving Ultrafast Photoinduced Deactivations in Water-Solvated Pyrimidine Nucleosides. *Journal of Physical Chemistry Letters* **2017**, *8*, 1777–1783.

(12) Voet, D.; Gratzer, W. B.; Cox, R. A.; Doty, P. Absorption spectra of nucleotides, polynucleotides, and nucleic acids in the far ultraviolet. *Biopolymers* **1963**, *1*, 193–208.

(13) Schreiber, M.; Silva-Junior, M. R.; Sauer, S. P.; Thiel, W. Benchmarks for electronically excited states: CASPT2, CC2, CCSD, and CC3. *Journal of Chemical Physics* **2008**, *128*, 134110.

(14) Zechmann, G.; Barbatti, M. Photophysics and deactivation pathways of thymine. *Journal of Physical Chemistry A* **2008**, *112*, 8273–8279.

(15) Barbatti, M.; Aquino, A. J. A.; Lischka, H. The UV absorption of nucleobases: semi-classical ab initio spectra simulations. *Physical Chemistry Chemical Physics* **2010**, *12*, 4959.

(16) Szalay, P. G.; Watson, T.; Perera, A.; Lotrich, V. F.; Bartlett, R. J. Benchmark studies on the building blocks of DNA. 1. Superiority of coupled cluster methods in describing the excited states of nucleobases in the Franck-Condon region. *Journal of Physical Chemistry A* **2012**, *116*, 6702–6710.

(17) Pepino, A. J.; Segarra-Martí, J.; Nenov, A.; Rivalta, I.; Improta, R.; Garavelli, M. UV-induced long-lived decays in solvated pyrimidine nucleosides resolved at the MS-CASPT2/MM level. *Physical Chemistry Chemical Physics* **2018**, *20*, 6877–6890.

(18) Kang, H.; Lee, K. T.; Jung, B.; Ko, Y. J.; Kim, S. K. Intrinsic lifetimes of the excited state of DNA and RNA bases. *Journal of the American Chemical Society* **2002**, *124*, 12958–12959.

(19) He, Y.; Wu, C.; Kong, W. Decay pathways of thymine and methyl-substituted uracil and thymine in the gas phase, 2003.

(20) Canuel, C.; Mons, M.; Piuzzi, F.; Tardivel, B.; Dimicoli, I.; Elhanine, M. Excited states dynamics of DNA and RNA bases: Characterization of a stepwise deactivation pathway in the gas phase. *Journal of Chemical Physics* **2005**, *122*, 074316.

(21) Ullrich, S.; Schultz, T.; Zgierski, M. Z.; Stolow, A. Electronic relaxation dynamics in DNA and RNA bases studied by time-resolved photoelectron spectroscopy. *Physical Chemistry Chemical Physics* **2004**, *6*, 2796–2801.

(22) Hudock, H. R.; Levine, B. G.; Thompson, A. L.; Satzger, H.; Townsend, D.; Gador, N.; Ullrich, S.; Stolow, A.; Martínez, T. J. Ab Initio molecular dynamics and time-resolved photoelectron spectroscopy of electronically excited uracil and thymine. *Journal of Physical Chemistry A* **2007**, *111*, 8500–8508.

(23) Wolf, T. J. A. et al. Probing ultrafast $\pi\pi/n\pi$ internal conversion in organic chromophores via K-edge resonant absorption. *Nature Communications* **2017**, *8*, 1–7.

(24) Wolf, T. J. A.; Parrish, R. M.; Myhre, R. H.; Martínez, T. J.; Koch, H.; Gühr, M. Observation of Ultrafast Intersystem Crossing in Thymine by Extreme Ultraviolet Time-Resolved Photoelectron Spectroscopy. *The Journal of Physical Chemistry A* **2019**, *123*, 6897–6903.

(25) Barbatti, M.; Aquino, A. J.; Szymczak, J. J.; Nachtigallová, D.; Hobza, P.; Lischka, H. Relaxation mechanisms of UV-photoexcited DNA and RNA nucleobases. *Proceedings of the National Academy of Sciences* **2010**, *107*, 21453–21458.

(26) Picconi, D.; Lami, A.; Santoro, F. Hierarchical transformation of Hamiltonians with linear and quadratic couplings for nonadiabatic quantum dynamics: Application to the $\pi\pi^*/n\pi^*$ internal conversion in thymine. *Journal of Chemical Physics* **2012**, *136*, DOI: 10.1063/1.4729049.

(27) Peon, J.; Zewail, A. H. DNA/RNA nucleotides and nucleosides: Direct measurement of excited-state lifetimes by femtosecond fluorescence up-conversion. *Chemical Physics Letters* **2001**, *348*, 255–262.

(28) Onidas, D.; Markovitsi, D.; Marguet, S.; Sharonov, A.; Gustavsson, T. Fluorescence properties of DNA nucleosides and nucleotides: A refined steady-state and femtosecond investigation. *Journal of Physical Chemistry B* **2002**, *106*, 11367–11374.

(29) Pecourt, J. M.; Peon, J.; Kohler, B. DNA excited-state dynamics: Ultrafast internal conversion and vibrational cooling in a series of nucleosides. *Journal of the American Chemical Society* **2001**, *123*, 10370–10378.

(30) Hare, P. M.; Crespo-Hernández, C. E.; Kohler, B. Internal conversion to the electronic ground state occurs via two distinct pathways for pyrimidine bases in aqueous solution. *Proceedings of the National Academy of Sciences* **2007**, *104*, 435–440.

(31) Xue, B.; Yabushita, A.; Kobayashi, T. Ultrafast dynamics of uracil and thymine studied using a sub-10 fs deep ultraviolet laser. *Physical Chemistry Chemical Physics* **2016**, *18*, 17044–17053.

(32) Prokhorenko, V. I.; Picchiotti, A.; Pola, M.; Dijkstra, A. G.; Miller, R. J. New Insights into the Photophysics of DNA Nucleobases. *Journal of Physical Chemistry Letters* **2016**, *7*, 4445–4450.

(33) Pilles, B. M.; Maerz, B.; Chen, J.; Bucher, D. B.; Gilch, P.; Kohler, B.; Zinth, W.; Fingerhut, B. P.; Schreier, W. J. Decay Pathways of Thymine Revisited. *Journal of Physical Chemistry A* **2018**, *122*, 4819–4828.

(34) Buchner, F.; Nakayama, A.; Yamazaki, S.; Ritze, H. H.; Lübcke, A. Excited-state relaxation of hydrated thymine and thymidine measured by liquid-jet photoelectron spectroscopy: Experiment and simulation. *Journal of the American Chemical Society* **2015**, *137*, 2931–2938.

(35) Cerezo, J.; Liu, Y.; Lin, N.; Zhao, X.; Improta, R.; Santoro, F. Mixed Quantum/Classical Method for Nonadiabatic Quantum Dynamics in Explicit Solvent Models: The $\pi\pi/\mathrm{n}\pi$ Decay of Thymine in Water as a Test Case. *Journal of Chemical Theory and Computation* **2018**, *14*, 820–832.

(36) Buchner, F.; Ritze, H. H.; Lahl, J.; Lübcke, A. Time-resolved photoelectron spectroscopy of adenine and adenosine in aqueous solution. *Physical Chemistry Chemical Physics* **2013**, *15*, 11402–11408.

(37) Buchner, F.; Heggen, B.; Ritze, H.-H.; Thiel, W.; Lübcke, A. Excited-state dynamics of guanosine in aqueous solution revealed by time-resolved photoelectron spectroscopy: experiment and theory. *Physical Chemistry Chemical Physics* **2015**, *17*, 31978–31987.

(38) Williams, H. L.; Erickson, B. A.; Neumark, D. M. Time-resolved photoelectron spectroscopy of adenosine and adenosine monophosphate photodeactivation dynamics in water microjets. *Journal of Chemical Physics* **2018**, *148*, 194303.

(39) Winter, B.; Faubel, M. Photoemission from liquid aqueous solutions. *Chemical Reviews* **2006**, *106*, 1176–1211.

(40) Seidel, R.; Winter, B.; Bradforth, S. E. Valence Electronic Structure of Aqueous Solutions: Insights from Photoelectron Spectroscopy. *Annual Review of Physical Chemistry* **2016**, *67*, 283–305.

(41) Suzuki, T. Time-resolved photoelectron spectroscopy of non-adiabatic electronic dynamics in gas and liquid phases. *International Reviews in Physical Chemistry* **2012**, *31*, 265–318.

(42) Faubel, M.; Siefermann, K. R.; Liu, Y.; Abel, B. Ultrafast soft X-ray photoelectron spectroscopy at liquid water microjets. *Accounts of Chemical Research* **2012**, *45*, 120–130.

(43) Shreve, A. T.; Yen, T. A.; Neumark, D. M. Photoelectron spectroscopy of hydrated electrons. *Chemical Physics Letters* **2010**, *493*, 216–219.

(44) Shreve, A. T.; Elkins, M. H.; Neumark, D. M. Photoelectron spectroscopy of solvated electrons in alcohol and acetonitrile microjets. *Chemical Science* **2013**, *4*, 1633–1639.

(45) Elkins, M. H.; Williams, H. L.; Shreve, A. T.; Neumark, D. M. Relaxation mechanism of the hydrated electron. *Science* **2013**, *342*, 1496–1499.

(46) Elkins, M. H.; Williams, H. L.; Neumark, D. M. Dynamics of electron solvation in methanol: Excited state relaxation and generation by charge-transfer-to-solvent. *Journal of Chemical Physics* **2015**, *142*, 234501.

(47) Elkins, M. H.; Williams, H. L.; Neumark, D. M. Isotope effect on hydrated electron relaxation dynamics studied with time-resolved liquid jet photoelectron spectroscopy. *Journal of Chemical Physics* **2016**, *144*, 184503.

(48) Faubel, M.; Schlemmer, S.; Toennies, J. P. A molecular beam study of the evaporation of water from a liquid jet. *Zeitschrift für Physik D Atoms, Molecules and Clusters* **1988**, *10*, 269–277.

(49) Knutson, J. R.; Davenport, L.; Brand, L. Anisotropy Decay Associated Fluorescence Spectra and Analysis of Rotational Heterogeneity. 1. Theory and Applications. *Biochemistry* **1986**, *25*, 1805–1810.

(50) Van Stokkum, I. H.; Larsen, D. S.; Van Grondelle, R. Global and target analysis of time-resolved spectra. *Biochimica et Biophysica Acta - Bioenergetics* **2004**, *1657*, 82–104.

(51) Gustavsson, T.; Bányász, Á.; Lazzarotto, E.; Markovitsi, D.; Scalmani, G.; Frisch, M. J.; Barone, V.; Improta, R. Singlet excited-state behavior of uracil and thymine in aqueous solution: A combined experimental and computational study of 11 uracil derivatives. *Journal of the American Chemical Society* **2006**, *128*, 607–619.

(52) Pecourt, J. M. L.; Peon, J.; Kohler, B. Ultrafast internal conversion of electronically excited RNA and DNA nucleosides in water. *Journal of the American Chemical Society* **2000**, *122*, 9348–9349.

(53) Gustavsson, T.; Sharonov, A.; Onidas, D.; Markovitsi, D. Adenine, deoxyadenosine and deoxyadenosine 5-monophosphate studied by femtosecond fluorescence upconversion spectroscopy. *Chemical Physics Letters* **2002**, *356*, 49–54.

(54) Gustavsson, T.; Sarkar, N.; Vayá, I.; Jiménez, M. C.; Markovitsi, D.; Improta, R. A joint experimental/theoretical study of the ultrafast excited state deactivation of deoxyadenosine and 9-methyladenine in water and acetonitrile. *Photochemical and Photobiological Sciences* **2013**, *12*, 1375–1386.

(55) Tomasi, J.; Mennucci, B.; Cammi, R. Quantum mechanical continuum solvation models. *Chemical Reviews* **2005**, *105*, 2999–3093.

(56) Wu, Y.; Tepper, H. L.; Voth, G. A. Flexible simple point-charge water model with improved liquid-state properties. *Journal of Chemical Physics* **2006**, *124*.

(57) Cadet, J., *Bioorganic Photochemistry*; Morrison, H., Ed.; John Wiley & Sons, Ltd: 1990.

(58) Horio, T.; Spesyvtsev, R.; Nagashima, K.; Ingle, R. A.; Suzuki, Y.-i.; Suzuki, T. Full observation of ultrafast cascaded radiationless transitions from S2($\pi\pi$) state of pyrazine using vacuum ultraviolet photoelectron imaging. *The Journal of Chemical Physics* **2016**, *145*, 044306.

Chapter 4

Progress Using XUV Light and Future Outlooks

This chapter will describe the progress we have made generating harmonics and applying them to atomic and molecular systems. So far, pump-probe signal has been elusive but I will describe various systems that we have tried and some suggested systems for future experiments.

4.1 Static Spectra

The first system studied using XUV light was gaseous argon (Ar(g)). It was chosen due to its simplicity, featuring only one energetically accessible electronic state bound by 15.76 eV. This was first photoionized using harmonics driven at 800 nm, shown in Figure 4.1, giving a broad range of harmonics ranging from 20.15 to 32.55 eV (corresponding to odd harmonics of 13, 15, 17, 19, and 21). This was a useful test case to fine tune the conditions needed to optimize the alignment of the XUV light.

As mentioned in Chapter 2, we only want to use a single harmonic for our experiments. There are an abundance of harmonics shown in Figure 4.1 with a relatively tight spacing of only 3.1 eV. Driving our harmonics with 400 nm increased this spacing to 6.1 eV and only produced harmonics 5, 7, and 9. By using an Al foil filter and the multilayer mirror described in Chapter 2 we were able to produce solely the 7th harmonic of 400 nm at 21.7 eV. Figure 4.2 shows the photoionization of argon using this beam and features only one peak, confirming our energetic purity.

After optimizing our XUV beam parameters in an atomic system, we moved to studying liquid water. By aligning our XUV light into the vapor jacket surrounding the liquid jet we were able to take spectra of gaseous water and by aligning the beam onto the jet we mea-

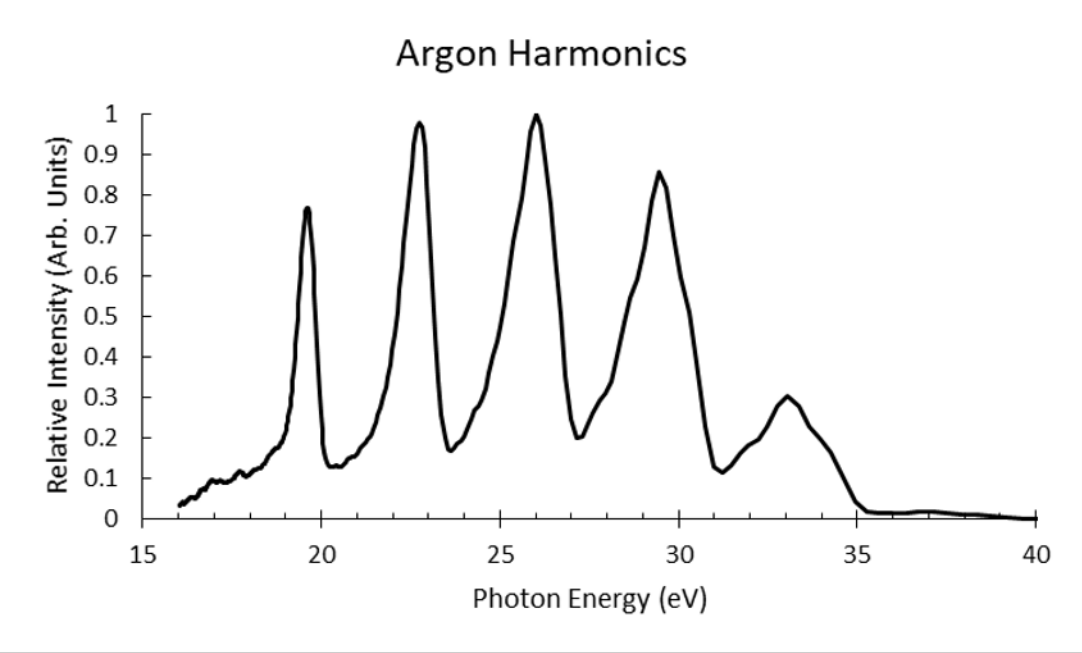

Figure 4.1: Harmonics generated in our SIGC in 5 torr of Ar using a 800 nm driving pulse. This spectrum is generated by using these harmonics to photoionize Ar(g).

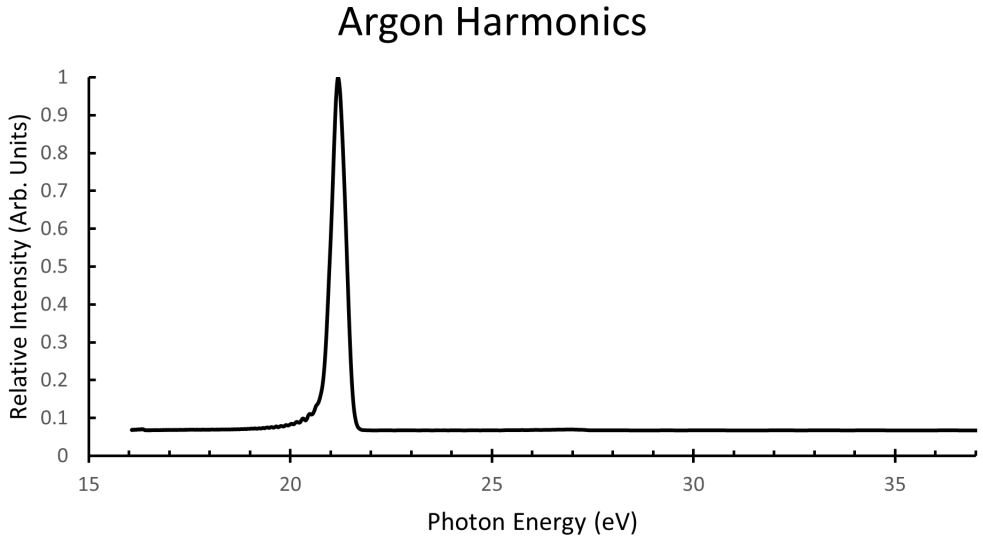

Figure 4.2: Harmonics generated in our SIGC in 5 torr of Ar using a 400 nm driving pulse after reflecting off of a multilayer mirror to select only the 7th harmonic. This spectrum is generated by using these harmonics to photoionize Ar(g).

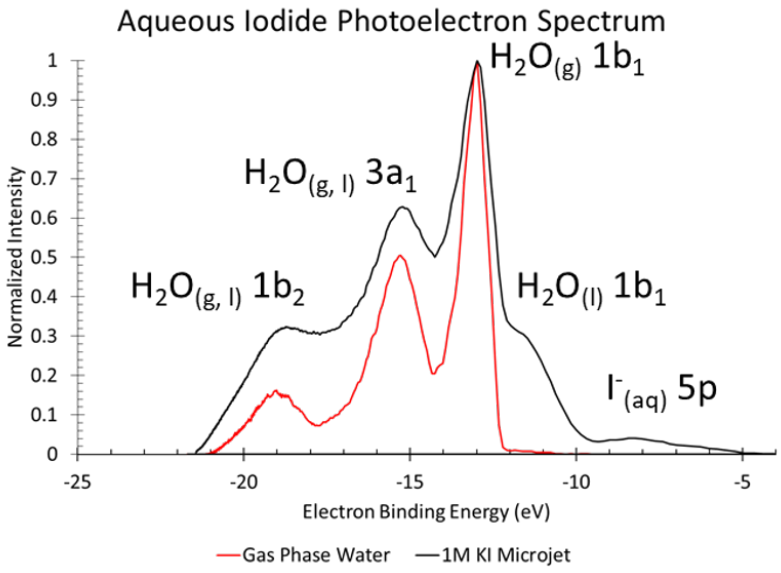

Figure 4.3: Comparison spectrum of a 1M KI solution in water vs. the gaseous water vapor jacket of the jet taken at a pulse energy of 21.7 eV.

sured the spectrum of liquid water. A comparison of the two is shown in Figure 4.3[1]. The gaseous spectrum features three main peaks corresponding to photoionization of the $1b_1$(g), $3a_1$(g), and $1b_2$(g) electronic states. When switching to liquid water we see a broadening of the $3a_1$ and $1b_2$ peaks due to the ionization of those states in liquid water.[2] All of the gas phase peaks are still present in this spectrum because the XUV spot size, measured as σ, is larger than the liquid jet (90 μm vs 30 μm), so there is still signal coming from the vapor jacket. The $1b_1$(l) peak is shifted towards lower binding energies and appears as a shoulder on the $1b_1$(g) peak. This provides a great guide for alignment and overall quality of the signal by optimizing the relative intensity of the $1b_1$(l) peak compared to the $1b_1$(g) peak.

Finally, various solutes were studied in liquid water. The first test was applying XUV light to a 1M potassium iodide (KI) jet, shown in Figure 4.3. This spectrum shows the same features as described above for liquid water, but it also features a new peak at lower binding energy. This peak corresponds to ionization of the 5p state of I^- at around 7 – 8 eV. The binding energy and relative intensity of this feature matches that seen by Winter et al. [1] showing the capability of this experiment to study solutes dissolved in liquid water.

[1]Note that this spectrum is not neat water, but a solution of KI, but it shows all of the water features clearly.

[2]Liquid phase signals are generally broader than their gas phase counterparts due to the multitude of energetically accessible microenvironments experienced by the molecules.

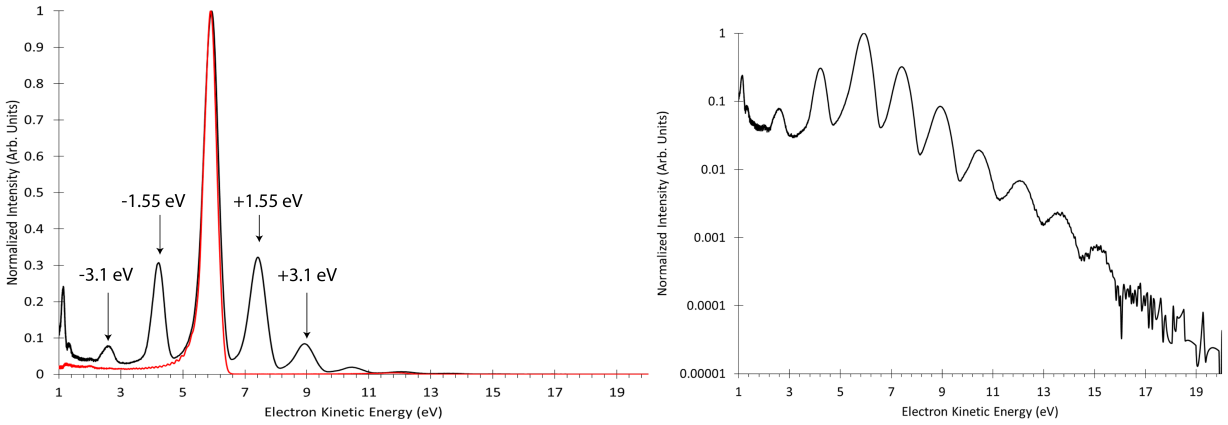

(a) (b)

Figure 4.4: LAPE data showing the emergence of sidebands when an 800 nm pulse is applied to the photoelectron spectrum of Ar(g). a) A comparison (normalized to the main photoionization peak) between 21.7 eV only (red) and 21.7 eV + 1.55 eV (black). b) 21.7 eV + 1.55 eV shows up to 6 orders of LAPE signal.

4.2 Laser-Assisted Photoelectric Effect

Moving from taking one color XUV data to two color time-resolved data proved to be fairly difficult. The first time-resolved data we were able to acquire was accomplished by using the laser-assisted photoelectric effect (LAPE) on the photoionization of Ar(g).

Ionization of Ar(g) with an XUV beam (probe) effectively creates a cloud of photoelectrons that are unbound with a kinetic energy dictated by Equation 1.1. When a second perturbative field (pump) interacts with these free electrons, sidebands appear in the photoelectron spectrum with kinetic energies of $\pm n\omega$ where ω is the frequency of the perturbing field and n is an integer [2–6]. This happens because the outgoing photoelectrons can be dressed by this pump field causing a redistribution of the observed electron kinetic energy distribution. Essentially, the electron can exchange photons with this field while it is in the continuum. Shown in Figure 4.4 is the comparison between an XUV only spectrum of Ar(g) and a spectrum where an 800 nm dressing field is also applied. The main photoionization peak is depleted to create sidebands spaced by integer multiples of $\pm$1.55 eV (800 nm).

LAPE can also be seen by using a 3.1 eV (400 nm) pump pulse as shown in Figure 4.5, however the intensity of the sidebands are much lower and fewer orders are observed. The amplitude of the nth sideband is given by

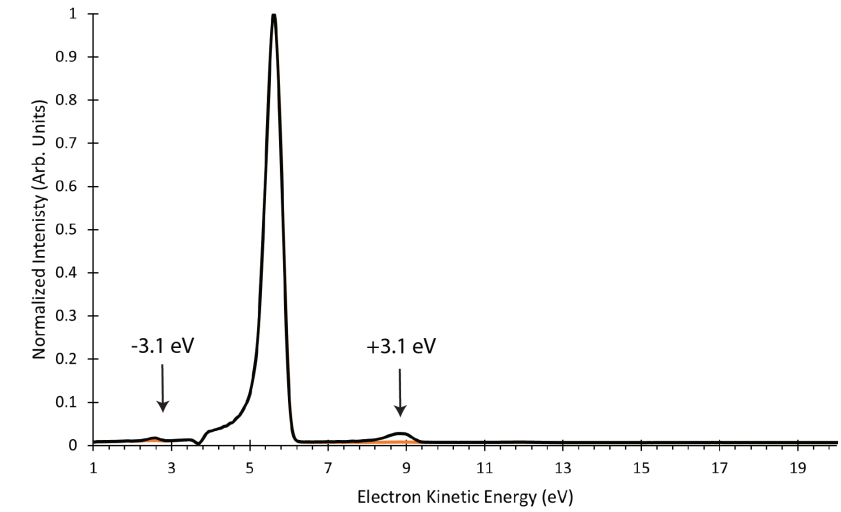

Figure 4.5: LAPE on Ar using pulse energies of 21.7 eV + 3.1 eV (400 nm)

$$a_n = J_n^2\left(\sqrt{\frac{16\pi\kappa I E_{kin}}{m_e \hbar \omega^4}}\right) \tag{4.1}$$

where J_n is a Bessel function of the first kind, n is the number of photons exchanged with the field, κ is the fine structure constant, I is the intensity of the pump pulse, and m_e is the mass of an electron [7]. This essentially says that there is a linear correlation between the amplitude of the peak to the intensity of the pump pulse and the kinetic energy of the electrons. There is also a wavelength scaling of λ^{-4} explaining why the sidebands are weaker for 3.1 eV (400 nm) compared to 1.55 eV (800 nm).

LAPE can also be performed on both liquid water and water vapor, as well [8]. If the steering of the beams drifts during an experiment, the jet can be moved to the side to allow LAPE on gaseous water to be performed providing an incredibly useful *in situ* diagnostic tool. After finding LAPE on gaseous water the jet can be put back into the beam and LAPE can be performed on liquid water. This is a trickier measurement as it shows up as a shift in the $1b_1$(l) peak rather than the emergence of a new, isolated feature, but it can be seen relatively easily with 1.55 eV (800 nm) + XUV and, with some work, 3.1 eV (400 nm) + XUV. All of the peaks in the water spectrum undergo LAPE leading to a complex spectra, shown in Figure 4.6, where different orders of LAPE overlap with each other making the spectrum difficult to assign. Despite this complexity, the spectra obtained matches very well with previous work on LAPE in liquid water[8].

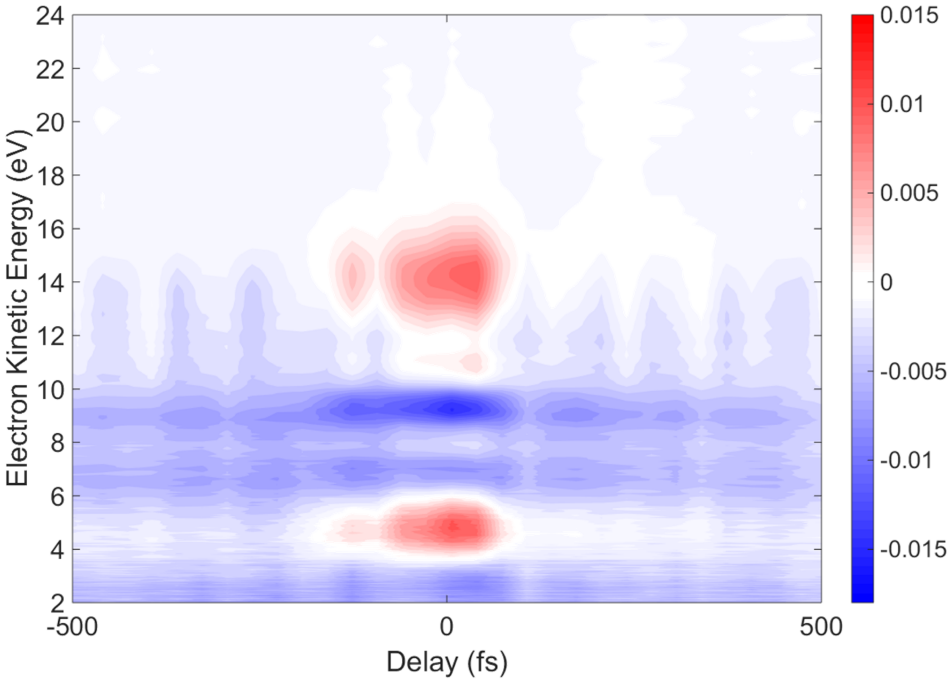

Figure 4.6: Contour plot of 21.7 eV + 1.55 eV LAPE spectrum of water.

Determination of Cross Correlation

LAPE on Ar(g) has served to be an excellent alignment tool as the sidebands are only seen when both the pump and probe pulse are spatially and temporally overlapped. The signals found here are spectrally well resolved and occur in a nearly background free region, making this a very sensitive measurement. Another useful piece of information that can be pulled out of these measurements is the cross correlation between the two pulses. The cross correlation is a convolution of the Gaussian temporal profiles of the two pulses used in the experiment, which is used in the fitting algorithm described in Chapter 2.[3] Previously, this parameter could not be directly measured; we had a close estimate for the number but it was fit during the GLA routine. In these experiments we can now directly measure the cross correlation, σ, by fitting the temporal profile of a side band to a Gaussian of the form:

$$g(x) = \frac{1}{\sigma\sqrt{2\pi}} exp\left(\frac{-(x-\mu)^2}{2\sigma^2}\right) \tag{4.2}$$

[3]Note that the the convolution of two Gaussians is simply another Gaussian.

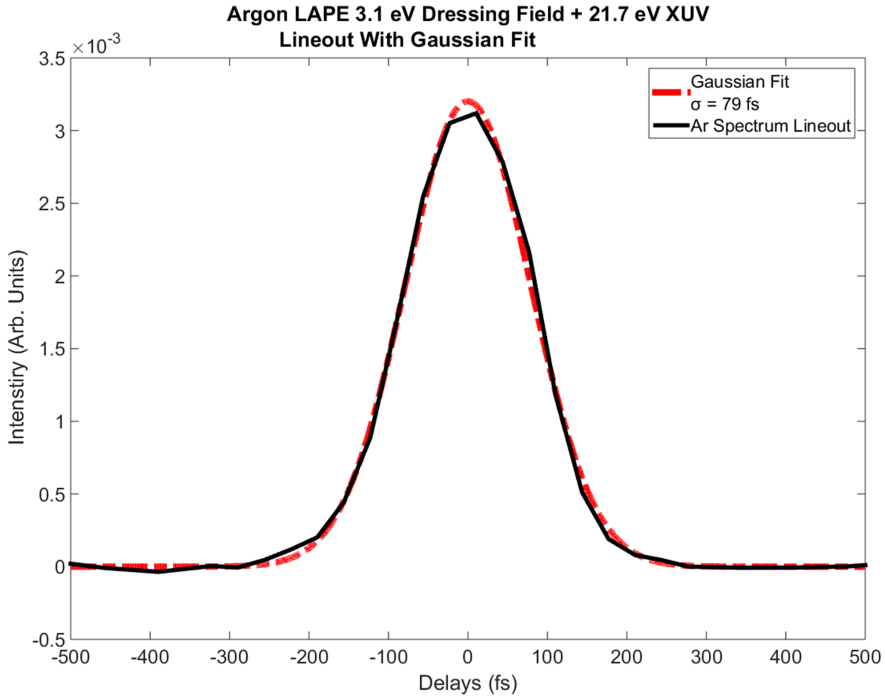

Figure 4.7: The integrated intensity of the first sideband of 21.7 eV + 3.1 eV LAPE in Ar(g) fit with a Gaussian profile.

This was done for 3.1 eV (400 nm) + XUV as shown in Figure 4.7 and yielded a σ of 89 fs.[4] This direct measurement should help increase our confidence in our fitting procedure in the future. One challenge will be finding LAPE signal using 4.66 eV (266 nm) or tunable UV light out of our TOPAS due to the wavelength scaling described above and thus may only work for future experiments done at longer wavelengths. Nevertheless, it is a useful number to have when performing experiments at these longer wavelengths.

4.3 Systems Studied, Successes and Failures

Thus far we have tried taking pump-probe data on a few systems that have been used for UV-pump XUV-probe experiments in the past, however our results have been largely unsuccessful. In this section I will discuss a couple of systems we have tried and some of the reasons why the experiments have not worked.

[4] 2.355σ = FWHM

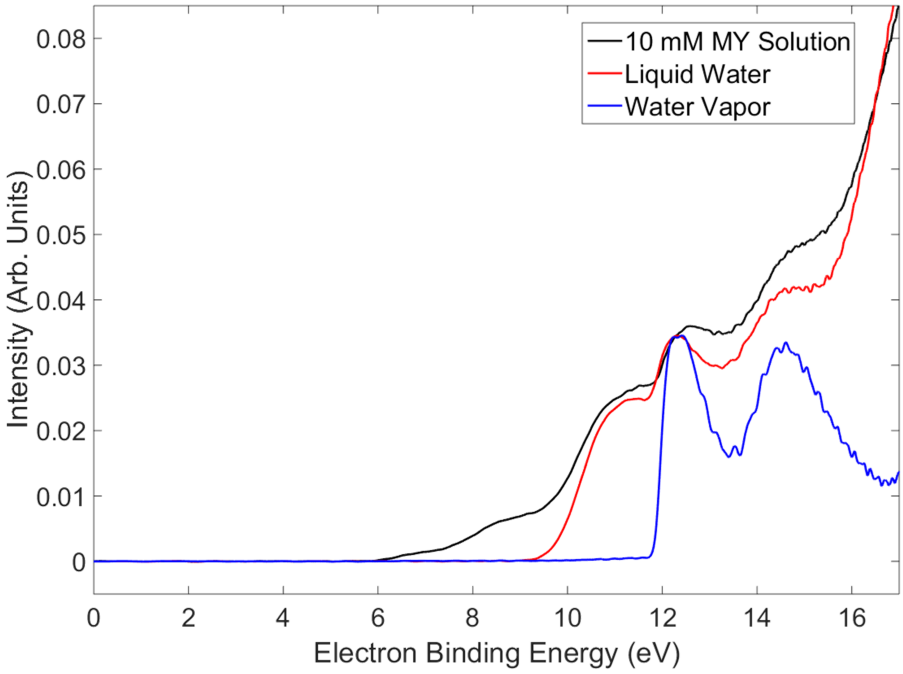

Figure 4.8: MY static spectrum (black) compared to liquid (red) and gaseous (blue) water.

Metanil Yellow

One of the first experiments we did was to try to replicate the experiments performed by Kornilov and coworkers [9] on the UV-induced dynamics of metanil yellow, an organic dye. While Kornilov studied three different dyes; metanil yellow (MY), metanil orange (MO), and quinoline yellow (QY), it was found that MY shows the largest number of counts per concentration so that is where we focused most of our efforts.

We first started by taking static spectra of the dye in liquid water, shown in Figure 4.8. The ground state spectrum features the liquid water spectrum and then, at lower binding energies, two new features attributed to ground state photoionization. Prior experiments found that when pumping the system at 400 nm, a new signal was found at lower binding energy ($\sim$2.5 – 5.5 eV) which was attributed to photoionization of an excited state generated by absorption of a 400 nm photon. This state was found to decay biexponentially on both fs and ps timescales.

Thus far we have been unable to observe this excited state signal with high certainty. Kornilov had to develop a “counting mode” algorithm to increase the signal to noise in the

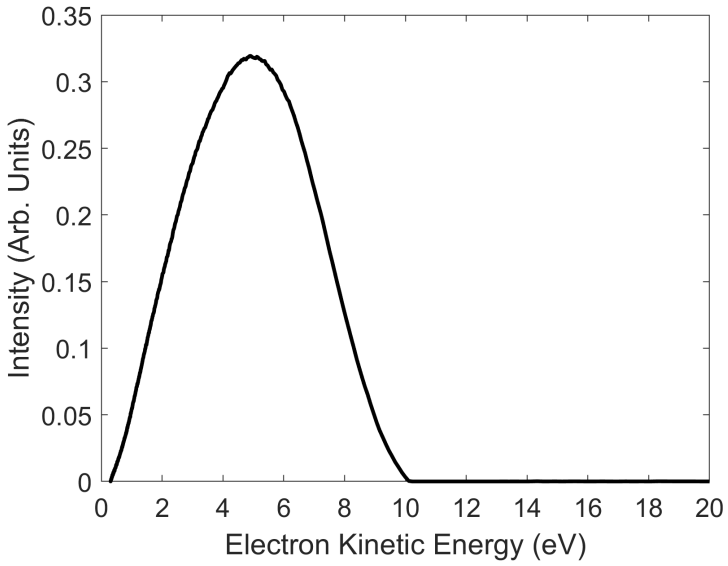

Figure 4.9: Multiphoton ionization signal taken of Metanil Yellow at 400 nm.

region and we have done similarly (See Appendix D for information on the code), but without much repeatable success.

One major difference between the two experiments is the probe energy used. Kornilov uses 26.5 eV light while we use 21.7 eV light. This should not be an issue in ionizing the excited state as it is bound by far less energy than either pulse, however it is a problem in achieving high enough pump energies. Spectra taken with only 400 nm, shown in Figure 4.9, feature a very broad peak due to multiphoton ionization (MPI) of the dye molecule. As the pump energy is increased this peak trends toward lower binding energy and eventually starts to overlap with the ground and excited state signals of MY. We must keep the flux of this beam low enough to measure the signal in a background free fashion, however since our probe pulse is lower in energy we have to use significantly less than was done by Kornilov et al. They use pump energies of $\sim$1 mJ/pulse while we are limited to $\sim$500 – 600 uJ/pulse. When trying to detect very weak signals, this could certainly make a difference.

Ferricyanide ion

The second system we have spent a reasonable amount of time studying is the ferricyanide ion. This ion features an Fe^{3+} core surrounded octohedrally with six CN^{-} ligands. Aziz and coworkers [10] performed pump probe photoelectron spectroscopy on this molecule studying the electronic relaxation after pumping the ligand-to-metal charge transfer (LMCT) process at 400 nm.

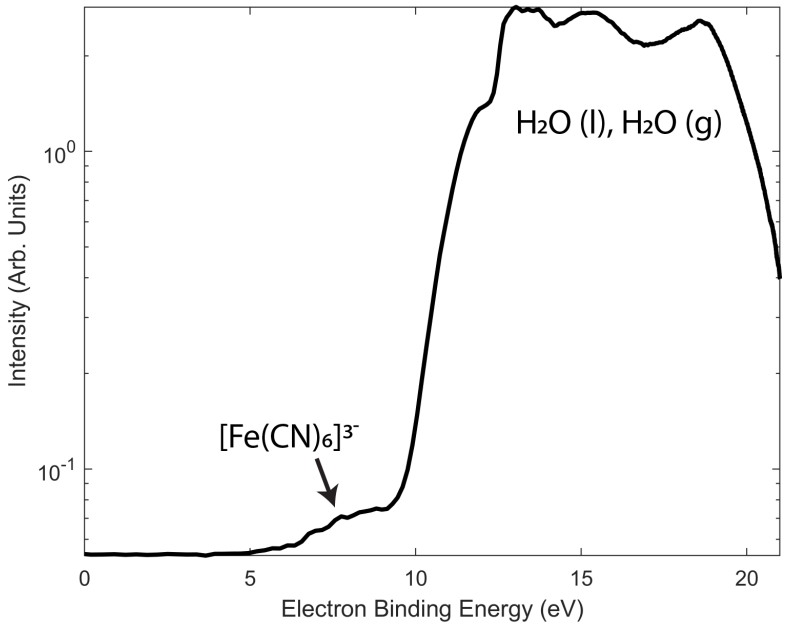

Figure 4.10: Photoelectron spectrum of the ferricyanide anion taken at a pulse energy of 21.7 eV in liquid water.

We started this experiment by taking a static spectra of a water solution with 500mM $K_3Fe(CN)_6$, shown in Figure 4.10. This spectrum shows the usual water orbitals as well as a new feature around 7 – 8 eBE corresponding to photoionization of the 3d electrons of Fe.

In the experiments of Aziz, it was found that upon excitation at 400 nm a new signal appeared at 6 – 7 eBE which decayed biexponentially in around 2 ps [10]. This signal appears to be quite a bit more pronounced than the signal from MY, however the jets formed of this solution are tremendously difficult to work with. Rapid freezing and spraying is found when working with these solutions which has preventing the accumulation of high quality data sets. One trick we have found to improving the stability of these jets is to remove the inline FRIT filter (described in Chapter 2). We are not certain as to why this works, but it tends to lower the necessary backing pressure to the point where we can run the jet for more than a few minutes. More work should be done on this system in the future.

4.4 Systems to try

Solvated Electron

The next system to try should be the solvated electron. It has been demonstrated in our lab [11–15] that solvated electrons can be readily generated by exciting a charge transfer to solvent (CTTS) state in I^- at 240 nm in liquid water[5]. Our TOPAS system is capable of generating around 6 mW of power at this wavelength (see section 2.5 of Chapter 2). By pumping the CTTS state, solvated electrons can be generated and will persist for multiple ns. These electrons are bound by 3.6 eV and can be photoejected in a nearly background free region of our spectrum. Additionally, the long lifetime of the solvated electron will allow the elimination of delay time as a variable in the alignment process. This can be done by setting the delay time such that the 240 nm pulse is a few hundred ps in front of the XUV pulse to ensure complete thermalization of the solvated electrons.

A novel feature of this experiment compared to our previous work is that we can now see photoemission from the 5p electrons in I^- using our higher probe energy (see Figure 4.3). In a time-resolved scan of this process we should observe a depletion of the population from this peak and the emergence of a new signal corresponding to neutral I. Additionally, a new peak at lower binding energy can be observed from the direct photoemission of the solvated electrons. Work is currently being done on this system.

Nucleic Acid Constituents

Finally, the experiment we built the XUV source to perform should be attempted in the near feature – tracking the UV-induced dynamics of electronically excited nucleobases. These experiments will be complementary to previous work we have done on Ado/AMP [16] and T/Thd/TMP [17], but the 21.7 eV probe pulse now has sufficient energy to ionize the ground state of the nucleic acid constituents (see Figure 4.11). This will allow for the simultaneous tracking of both the ground and any excited states that are populated, providing us a complete picture of the relaxation dynamics of these systems. We will likely want to pump these systems at 266 nm using frequency tripled light rather than using the tunable UV light from the TOPAS due it being more stable, at least for preliminary testing and optimization. Similar to the previous section on solvated electrons, a depletion of the ground state signal and a new feature at lower eBE should be observed when the pulses are overlapped.

[5]Note that solvated electrons can also be produced by a similar mechanism in $K_4Fe(CN)_6$ at 266 nm, but we have found these jets to be harder to work with than using I^-

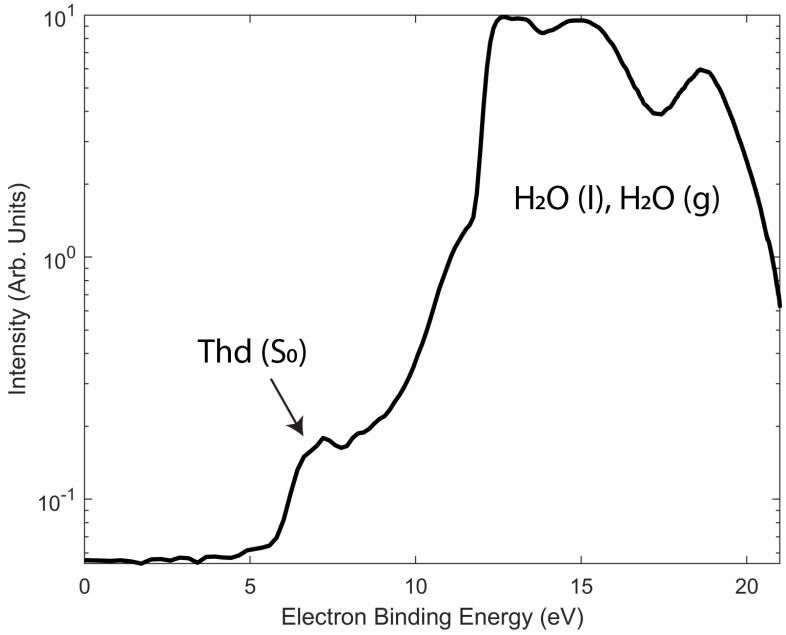

Figure 4.11: Photoelectron spectrum of Thd taken at a pulse energy of 21.7 eV in liquid water.

References

(1) Winter, B.; Weber, R.; Hertel, I. V.; Faubel, M.; Jungwirth, P.; Brown, E. C.; Bradforth, S. E. Electron binding energies of aqueous alkali and halide ions: EUV photoelectron spectroscopy of liquid solutions and combined Ab initio and molecular dynamics calculations. *Journal of the American Chemical Society* **2005**, *127*, 7203–7214.

(2) Schins, J. M.; Breger, P.; Agostini, P.; Constantinescu, R. C.; Muller, H. G.; Grillon, G.; Antonetti, A.; Mysyrowicz, A. Laser-assisted Auger decay as free-free transitions in a high-intensity laser field. *Physical Review A* **1995**, *2*.

(3) Schins, J. M.; Breger, P.; Agostini, P.; Sur ', G.; Ance, Y. F.; Constantinescu, R. C.; Muller, H. G.; Grillon, G.; Antonetti, A.; Mysyrowicz, A. Observation of Laser-Assisted Auger Decay in Argon. *Physical Review Letters* **1994**, *73*, 2180–2183.

(4) Glover, T. E.; Schoenlein, R. W.; Chin, A. H.; Shank, C. V. Observation of Laser Assisted Photoelectric Effect and Femtosecond High Order Harmonic Radiation. *Physical Review Letters* **1996**, *76*, 2468–2471.

(5) Miaja-Avila, L.; Lei, C.; Aeschlimann, M.; Gland, J. L.; Murnane, M. M.; Kapteyn, H. C.; Saathoff, G. Laser-Assisted Photoelectric Effect from Surfaces. *Physical Review Letters* **2006**, *97*, 113604.

(6) Wang, Y. H.; Steinberg, H.; Jarillo-Herrero, P.; Gedik, N. Observation of floquet-bloch states on the surface of a topological insulator. *Science* **2013**, *342*, 453–457.

(7) Saathoff, G.; Miaja-Avila, L.; Aeschlimann, M.; Murnane, M. M.; Kapteyn, H. C. Laser-assisted photoemission from surfaces. *Physical Review A* **2007**, *77*, 022903.

(8) Arrell, C. A.; Ojeda, J.; Mewes, L.; Grilj, J.; Frassetto, F.; Poletto, L.; Van Mourik, F.; Chergui, M. Laser-Assisted Photoelectric Effect from Liquids. *Physical Review Letters* **2016**, *117*, 143001.

(9) Hummert, J.; Reitsma, G.; Mayer, N.; Ikonnikov, E.; Eckstein, M.; Kornilov, O. Femtosecond Extreme Ultraviolet Photoelectron Spectroscopy of Organic Molecules in Aqueous Solution. *Journal of Physical Chemistry Letters* **2018**, *9*, 6649–6655.

(10) Engel, N.; Bokarev, S. I.; Moguilevski, A.; Raheem, A. A.; Al-Obaidi, R.; Möhle, T.; Grell, G.; Siefermann, K. R.; Abel, B.; Aziz, S. G.; Kühn, O.; Borgwardt, M.; Kiyan, I. Y.; Aziz, E. F. Light-induced relaxation dynamics of the ferricyanide ion revisited by ultrafast XUV photoelectron spectroscopy. *Physical Chemistry Chemical Physics* **2017**, *19*.

(11) Shreve, A. T.; Yen, T. A.; Neumark, D. M. Photoelectron spectroscopy of hydrated electrons. *Chemical Physics Letters* **2010**, *493*, 216–219.

(12) Shreve, A. T.; Elkins, M. H.; Neumark, D. M. Photoelectron spectroscopy of solvated electrons in alcohol and acetonitrile microjets. *Chemical Science* **2013**, *4*, 1633–1639.

(13) Elkins, M. H.; Williams, H. L.; Shreve, A. T.; Neumark, D. M. Relaxation mechanism of the hydrated electron. *Science* **2013**, *342*, 1496–1499.

(14) Elkins, M. H.; Williams, H. L.; Neumark, D. M. Dynamics of electron solvation in methanol: Excited state relaxation and generation by charge-transfer-to-solvent. *Journal of Chemical Physics* **2015**, *142*, 234501.

(15) Elkins, M. H.; Williams, H. L.; Neumark, D. M. Isotope effect on hydrated electron relaxation dynamics studied with time-resolved liquid jet photoelectron spectroscopy. *Journal of Chemical Physics* **2016**, *144*, 184503.

(16) Williams, H. L.; Erickson, B. A.; Neumark, D. M. Time-resolved photoelectron spectroscopy of adenosine and adenosine monophosphate photodeactivation dynamics in water microjets. *Journal of Chemical Physics* **2018**, *148*, 194303.

(17) Erickson, B. A.; Heim, Z. N.; Pieri, E.; Liu, E.; Martinez, T. J.; Neumark, D. M. Relaxation Dynamics of Hydrated Thymine, Thymidine, and Thymidine Monophosphate Probed by Liquid Jet Time-Resolved Photoelectron Spectroscopy. *J. Phys. Chem. A* **2019**, *123*, 32.

Appendix A

Supplementary Information for "Relaxation Dynamics of Hydrated Thymine, Thymidine, and Thymidine Monophosphate Probed by Liquid Jet Time-Resolved Photoelectron Spectroscopy"

Blake A. Erickson, Zachary N. Heim, Elisa Pieri, Erica Liu, Todd J. Martinez, and Daniel M. Neumark. J. Phys. Chem. A 2019, 123, 50, 10676–10684.

A.1 Experimental Data

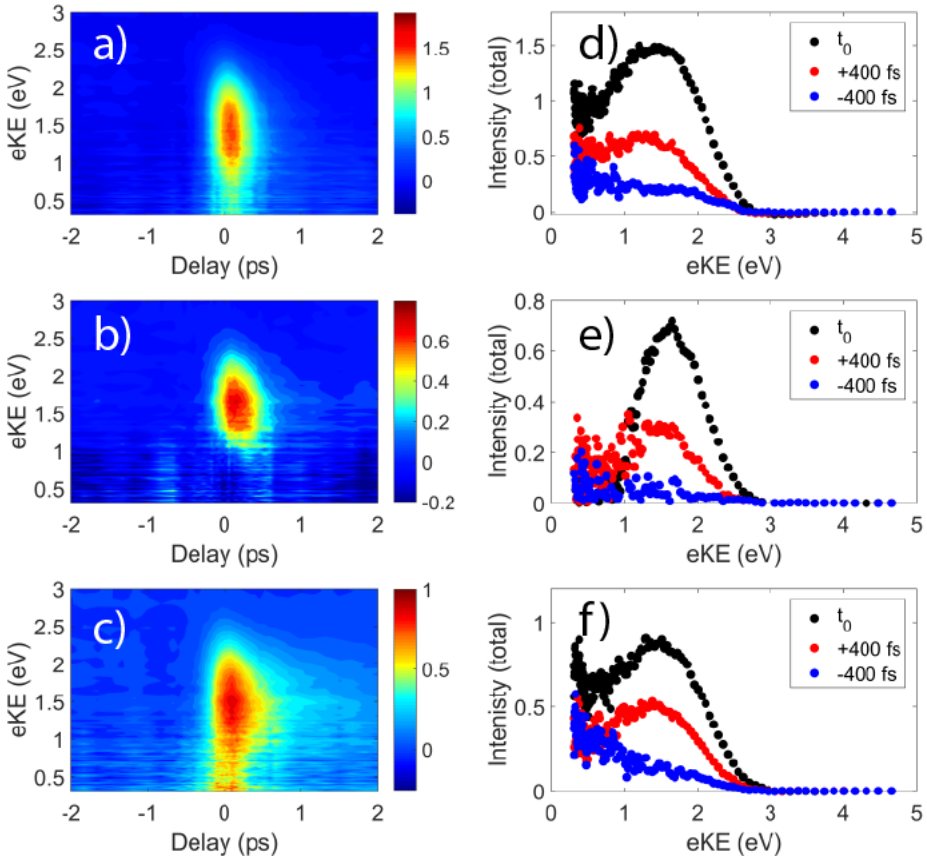

Figure A.1: Processed data for 4.74/6.20 eV (positive delays) and 6.20/4.74 eV (negative delays) experiments. (a-c) Filled contour plots for T, Thd, and TMP. (d-f) Select lineouts to show the two features. Peak A is in red and peak B is in blue. The black trace shows when the two pulses are overlapped in time.

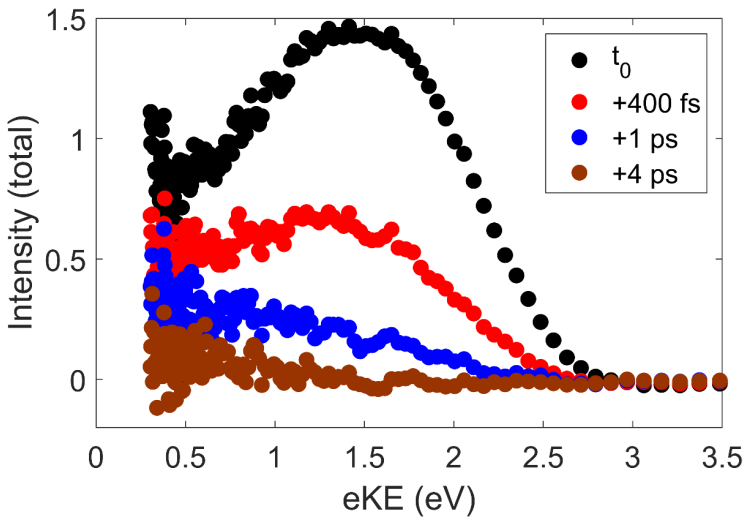

Figure A.2: Select lineouts shown for the 4.74/6.20 eV experiment in T. The signal is found to decay completely within a few ps with no emergence of a new signal at long times.

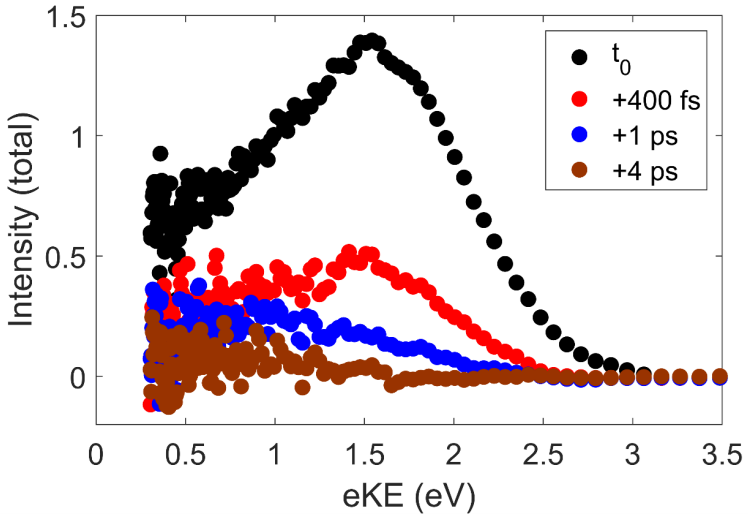

Figure A.3: Select lineouts shown for the 4.74/6.20 eV experiment in Thd. The signal is found to decay completely within a few ps with no emergence of a new signal at long times.

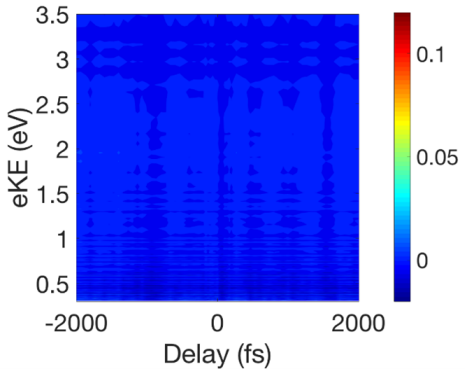

Figure A.4: Raw data for Trizma HCl buffered (2 mM) NaCl (100 mM) solution with a 4.67 eV pump and 6.20 eV probe.

A.2 Computational Methods

The molecular structures of T, Thd, and TMP have been optimized at the PBE0/6-31G* level of theory; for TMP, both the singly deprotonated and the doubly deprotonated forms have been initially studied, but after careful examination of the computational results on $TMP^{(-2)}$, the latter has been discarded due to maximal similarity to the $TMP^{(-1)}$ results. The force field parameters have been retrieved from the Amber FF14SB forcefield [1, 2] and, in the case of phosphate molecules, slightly adapted with RESP [3] fitting to match the correct total charge and adjusted for accurately modeling the behavior of the terminal anionic oxygen atoms [4].

The molecules have been solvated with a cubic box (dimensions of 70 Å) using a flexible SPC water model [5]. After an initial minimization with restraints on the solute to release bad contacts with water molecules, the density was equilibrated at low temperature (10 K) by slowly lifting the restraints, using the SHAKE algorithm [6], periodic boundary conditions, anisotropic pressure scaling and a cutoff for the non-bonding interactions of 8 Å. The system is then heated to 300 K using the weak-coupling algorithm [7] and restoring constraints of the solute; finally, the constraints are lifted again during another density equilibration, prior to running a classical molecular dynamics trajectory for 100 ns.

The 100,000 snapshots extracted from each trajectory have been clustered using the Hierarchical Agglomerative Algorithm [8] with the RMSD as the distance criterion; this procedure yielded 5 clusters per molecule, whose RMSD distance ranged between 0.6 Å and 2.5 Å.

The absorption spectra have been calculated at the SA3-CASSCF(8/6)/6-31G* level of theory choosing 1000 snapshots from the respective MM simulation, according to the

distribution obtained from the cluster analysis; the active space includes a n orbital on O_4, reflecting the work by Hudock et al. [9]; the QM region contains only the solute molecule, while water molecules within a 15 Å radius are treated classically. The absorbance I is calculated as a function of the energy ω with a gaussian fitting:

$$I(\omega) = \frac{1}{N} \sum_{i}^{N} \left| \hat{T}_l \right| e^{-\frac{(\omega - \Delta E_i)^2}{2\sigma^2}} \tag{A.1}$$

where N is the number of points, $\hat{T}_i$ and ΔE_i are respectively the oscillator strength and the vertical excitation energy of point i and σ, the broadening parameter, has been set to 0.2.

XMS-CASPT2(8/7)/6-31G* single point energy calculations on 5 states have been performed on the 100 geometries whose excitation energy is closest to the calculated absorption maximum at the CASSCF level of theory. An average shift between the XMS-CASPT2 and the CASSCF values has been calculated as:

$$\omega_{shift} = \frac{1}{N} \sum_{i}^{N} \Delta E_i^{XMS-CASPT2} - \Delta E_i^{CASSCF} \tag{A.2}$$

The shift has been applied to the CASSCF spectrum using the equation:

$$I(\omega)^{XMS-CASPT2} = I(\omega - \omega_{shift})^{CASSCF} \tag{A.3}$$

The MM calculations and analysis have been performed with Amber18 [10], while TeraChem [11, 12] has been employed for the QM and QM/MM calculations, where for the latter an interface with OpenMM [13] is used. For the XMS-CASPT2 [14] calculations, we employed Bagel [15].

A.3 Charge Distribution Analysis

The differences evidenced in the calculated absorption spectra are reflected by the changes in the charge distribution induced on the thymine ring when linked to deoxyribose and (indirectly) to the phosphate group. A Natural Bond Orbital analysis of the thymine ring ground state charges reveals small changes for C_6 and H_3, which decrease slightly their positive charge going from T to TMP (from 0.12 to 0.07 e in C_6 and from 0.31 to 0.24 e in H_3), and for N_1 and O_2, which decrease their negative charge (respectively, from -0.16 to -0.06 and

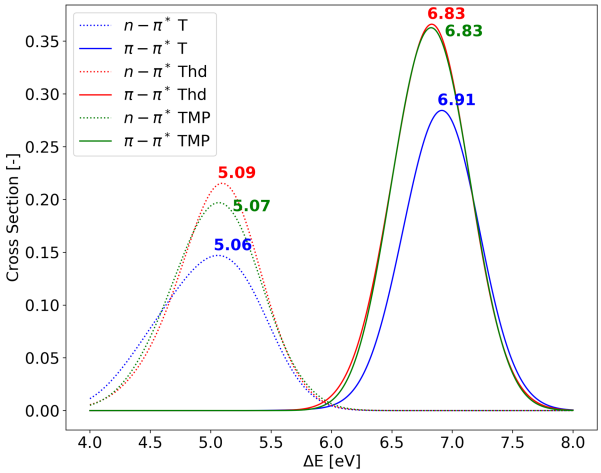

Figure A.5: Absorption spectrum of Thy (in blue), Thd (in red) and $TMP^{(-1)}$ (in green) calculated at the CASSCF(8/6)/6-31G* level of theory in a QM/MM framework. The spectrum was obtained with a Gaussian fitting of the excitation energies and oscillator strengths of the first two excited states over 1000 geometries as described in the Computational Methods section; since the $n\pi^*$ oscillator strength is close to zero, it has been multiplied by 500 in order to compare the two excited states energies.

Solvent	**Thd**	**TMP**
water	1.9	-7.2
acetonitrile	2.0	-7.7
chloroform	2.3	-14.2

Table A.1: Ground state energy difference ($E_{anti} - E_{syn}$) in Kcal/mol between the two individuated conformations calculated at the PBE0/6-31G* level of theory using various solvents.

from -0.77 to -0.73 e).

A.4 Analysis

The functional form of an individual kinetic component is a single exponential decay convolved with the Gaussian IRF and a Heaviside function, and is described by Eq. A.4.

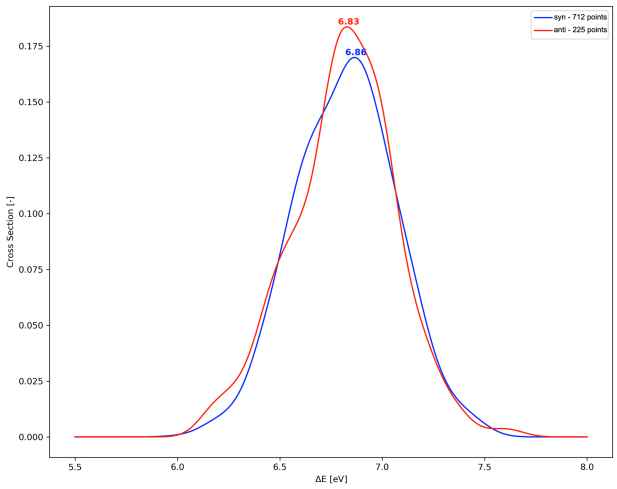

Figure A.6: Absorption spectrum of the two main conformations of Thd calculated at the CASSCF(8/6)/6-31G* level of theory in a QM/MM framework. The spectrum was obtained with a Gaussian fitting of the excitation energies and oscillator strengths of the first two excited states over snapshots belonging to a given conformation.

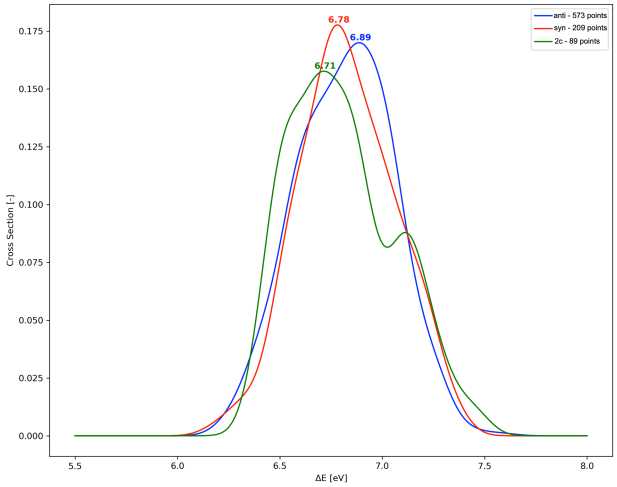

Figure A.7: Absorption spectrum of the three main conformations of TMP calculated at the CASSCF(8/6)/6-31G* level of theory in a QM/MM framework. The spectrum was obtained with a Gaussian fitting of the excitation energies and oscillator strengths of the first two excited states over snapshots belonging to a given conformation. Green corresponds to 2c in Figure 3.2.

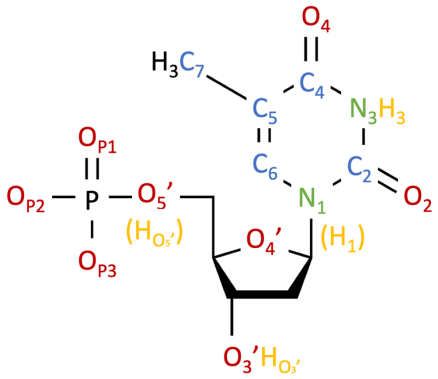

Figure A.8: Atom names for notable atoms (colored) in Thy, Thd and TMP.

	Thd	**TMP**
syn → anti	21.6 ± 14.7	41.9 ± 24.4
anti → syn	20.3 ± 12.0	33.5 ± 21.6

Table A.2: Timescale for transitions between the syn and anti conformations in Thd and TMP (in ps) expressed as the average value calculated along 100 ns long classical trajectories. The values are calculated using the C_6-N_1-C_1'-C_2' dihedral angle. For each of the two main conformations, we calculated the average value μ of this dihedral and the relative standard deviation σ; then we measured the number of MD steps spent to go from $\mu_{syn} - \sigma_{syn}$ to $\mu_{anti} + \sigma_{anti}$ (and viceversa).

$$f(t-t_0) = \frac{I_0}{2} e^{(\sigma^2/(2\tau^2)-(t-t_0)/\tau)} \left[erf\left(\frac{t-t_0}{\sigma\sqrt{2}} - \frac{\sigma}{\tau\sqrt{2}}\right) + 1 \right] \tag{A.4}$$

References

(1) Zgarbov, M.; Otyepka, M.; Rí Sponer, J.; St Ml, A.; Ban, P.; Cheatham, T. E.; Jure, P. Refinement of the Cornell et al. Nucleic Acids Force Field Based on Reference Quantum Chemical Calculations of Glycosidic Torsion Profiles. *J. Chem. Theory Comput* **2011**, *7*, 2886–2902.

(2) Maier, J. A.; Martinez, C.; Kasavajhala, K.; Wickstrom, L.; Hauser, K. E.; Simmerling, C. ff14SB: Improving the Accuracy of Protein Side Chain and Backbone Parameters from ff99SB. *J. Chem. Theory Comput* **2015**, *11*, 3713.

(3) Singh, U. C.; Kollman, P. A. An approach to computing electrostatic charges for molecules. *Journal of Computational Chemistry* **1984**, *5*, 129–145.

(4) Meagher, K. L.; Redman, L. T.; Carlson, H. A. Development of polyphosphate parameters for use with the AMBER force field. *Journal of Computational Chemistry* **2003**, *24*, 1016–1025.

(5) Wu, Y.; Tepper, H. L.; Voth, G. A. Flexible simple point-charge water model with improved liquid-state properties. *Journal of Chemical Physics* **2006**, *124*.

(6) Ryckaert, J. P.; Ciccotti, G.; Berendsen, H. J. Numerical integration of the cartesian equations of motion of a system with constraints: molecular dynamics of n-alkanes. *Journal of Computational Physics* **1977**, *23*, 327–341.

(7) Berendsen, H. J.; Postma, J. P.; Van Gunsteren, W. F.; Dinola, A.; Haak, J. R. Molecular dynamics with coupling to an external bath. *The Journal of Chemical Physics* **1998**, *81*, 3684.

(8) Zepeda-Mendoza, M. L.; Resendis-Antonio, O. In *Encyclopedia of Systems Biology*; Springer New York: New York, NY, 2013, pp 886–887.

(9) Hudock, H. R.; Levine, B. G.; Thompson, A. L.; Satzger, H.; Townsend, D.; Gador, N.; Ullrich, S.; Stolow, A.; Martínez, T. J. Ab Initio molecular dynamics and time-resolved photoelectron spectroscopy of electronically excited uracil and thymine. *Journal of Physical Chemistry A* **2007**, *111*, 8500–8508.

(10) Case, D.; V.B.J.T.B.R.M.B.Q.C.D.S.C.T.E.C.I.I.I.T.A. The Amber Molecular Dynamics Package, in AMBER 18, University of California, San Francisco, 2018.

(11) Titov, A. V.; Ufimtsev, I. S.; Luehr, N.; Martinez, T. J. Generating Efficient Quantum Chemistry Codes for Novel Architectures. *Journal of Chemical Theory and Computation* **2013**, *9*, 213–221.

(12) Ufimtsev, I. S.; Martinez, T. J. Quantum Chemistry on Graphical Processing Units. 3. Analytical Energy Gradients, Geometry Optimization, and First Principles Molecular Dynamics. *Journal of Chemical Theory and Computation* **2009**, *5*, 2619–2628.

(13) Eastman, P. et al. OpenMM 4: A Reusable, Extensible, Hardware Independent Library for High Performance Molecular Simulation. *Journal of Chemical Theory and Computation* **2013**, *9*, 461–469.

(14) Shiozaki, T.; Győrffy, W.; Celani, P.; Werner, H.-J. Communication: Extended multi-state complete active space second-order perturbation theory: Energy and nuclear gradients. *The Journal of Chemical Physics* **2011**, *135*, 081106.

(15) Shiozaki, T. BAGEL: Brilliantly Advanced General Electronic-structure Library. *WIREs Computational Molecular Science* **2018**, *8*, p. e1331.

Appendix B

Machine Drawings

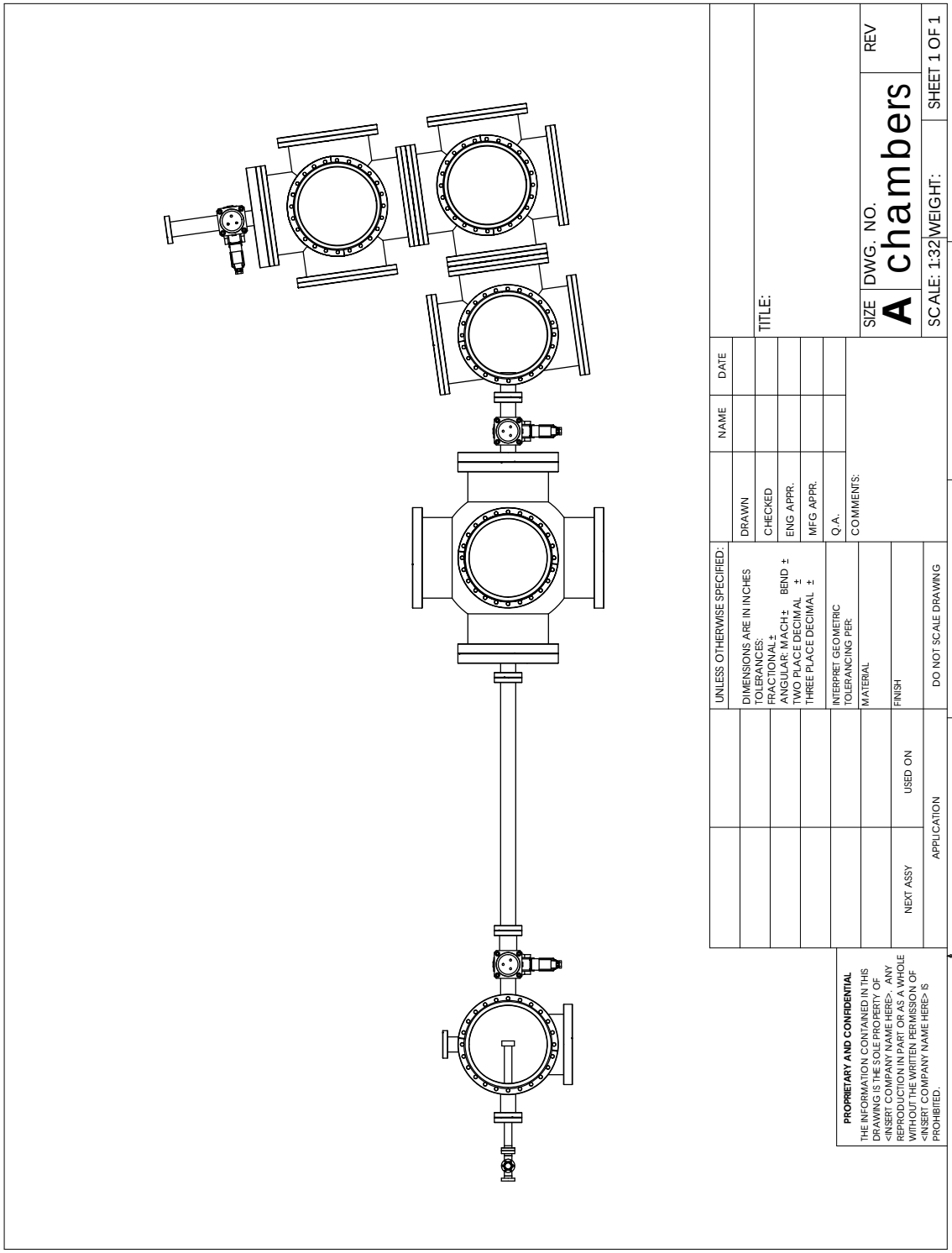

Figure B.1: The complete HHG line chamber assembly.

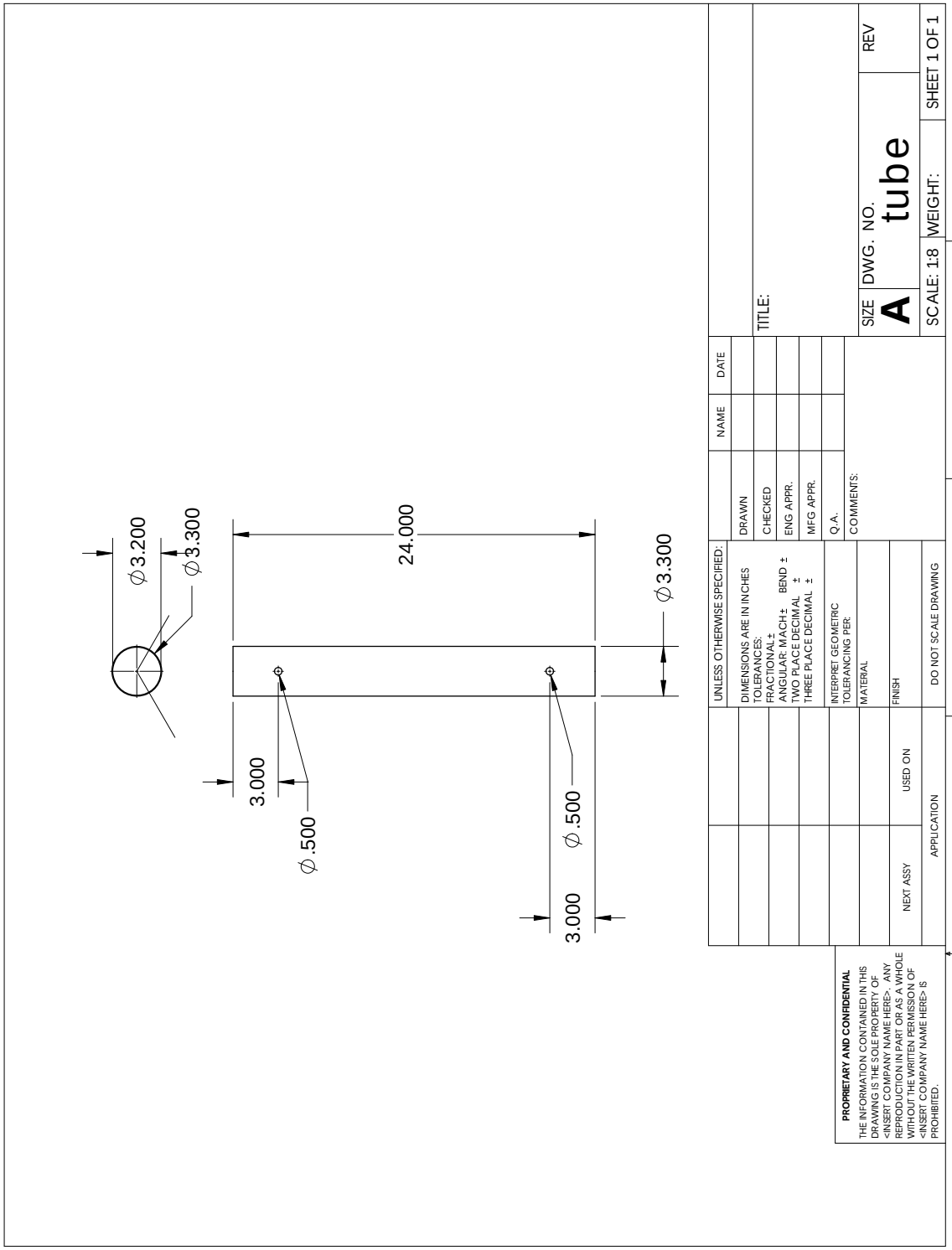

Figure B.2: Decelerator tube to be inserted into the detector and held at a floating voltage to slow down fast photoelectrons.

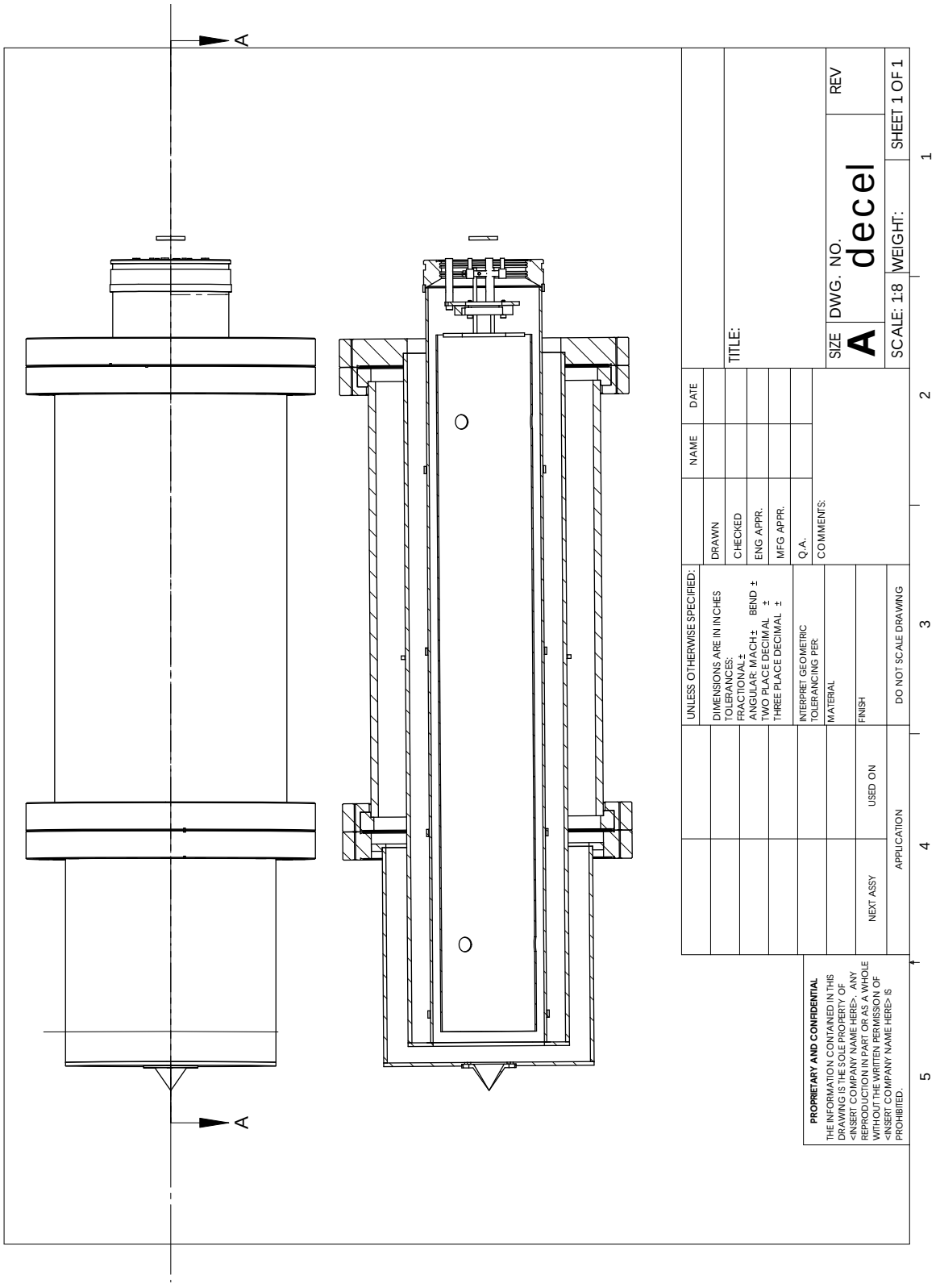

Figure B.3: The decelerator tube in the detector chamber.

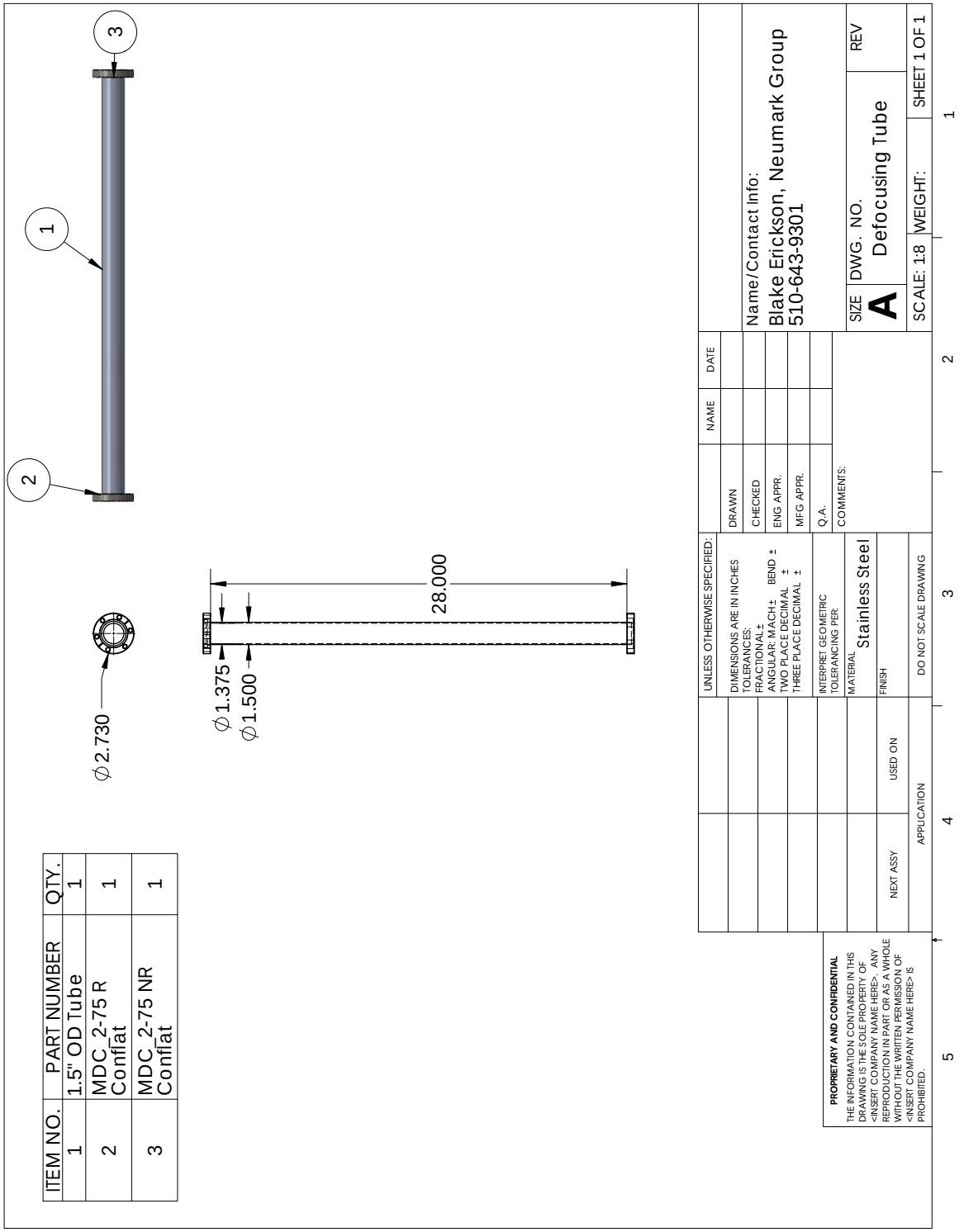

Figure B.4: The tube between the SIGC and the beam analyzer to allow the beam expand before going through the foils.

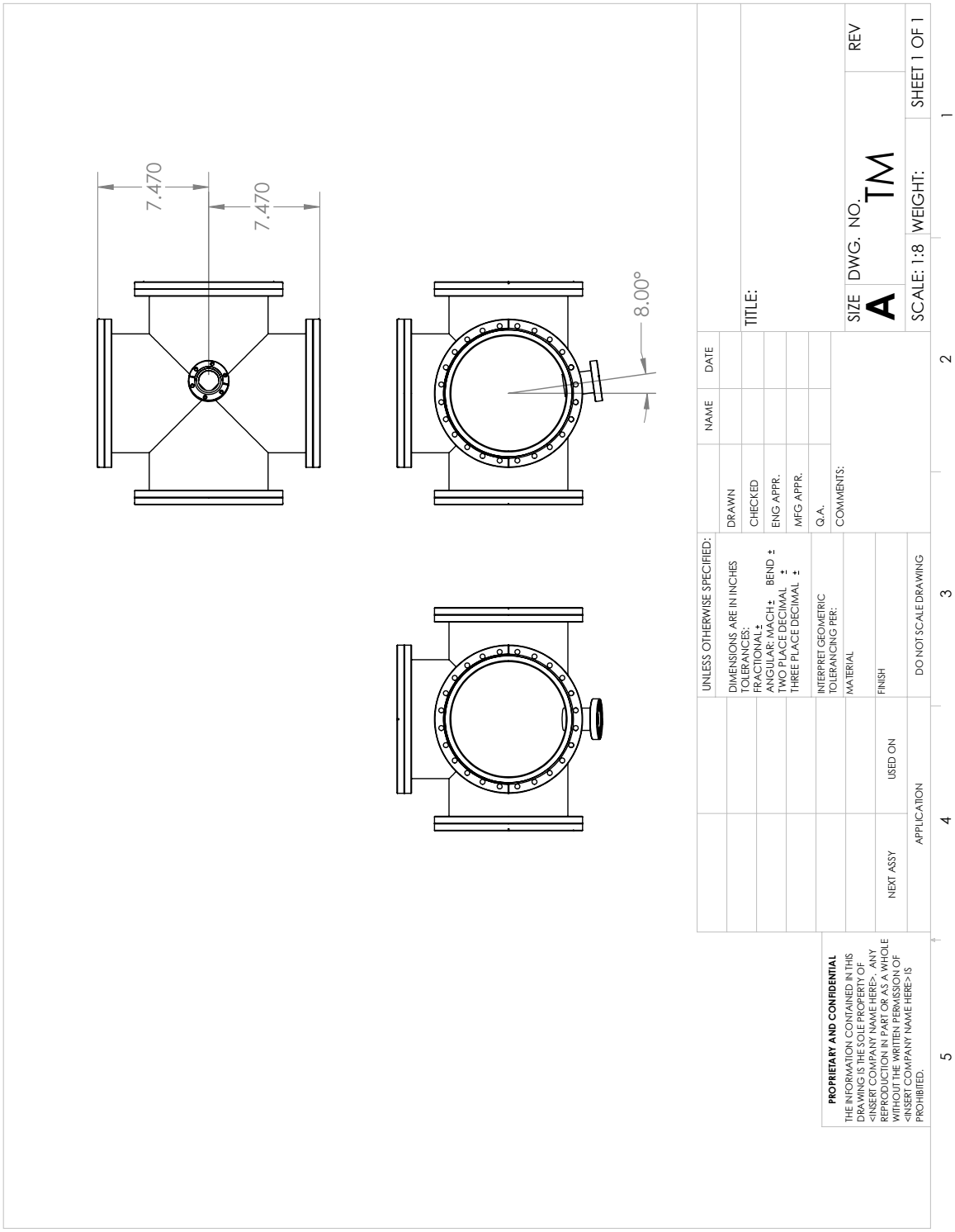

Figure B.5: The custom designed chamber for the toroidal mirror. A 2-3/4" CF is welded at 8 degrees onto a 5-way cross.

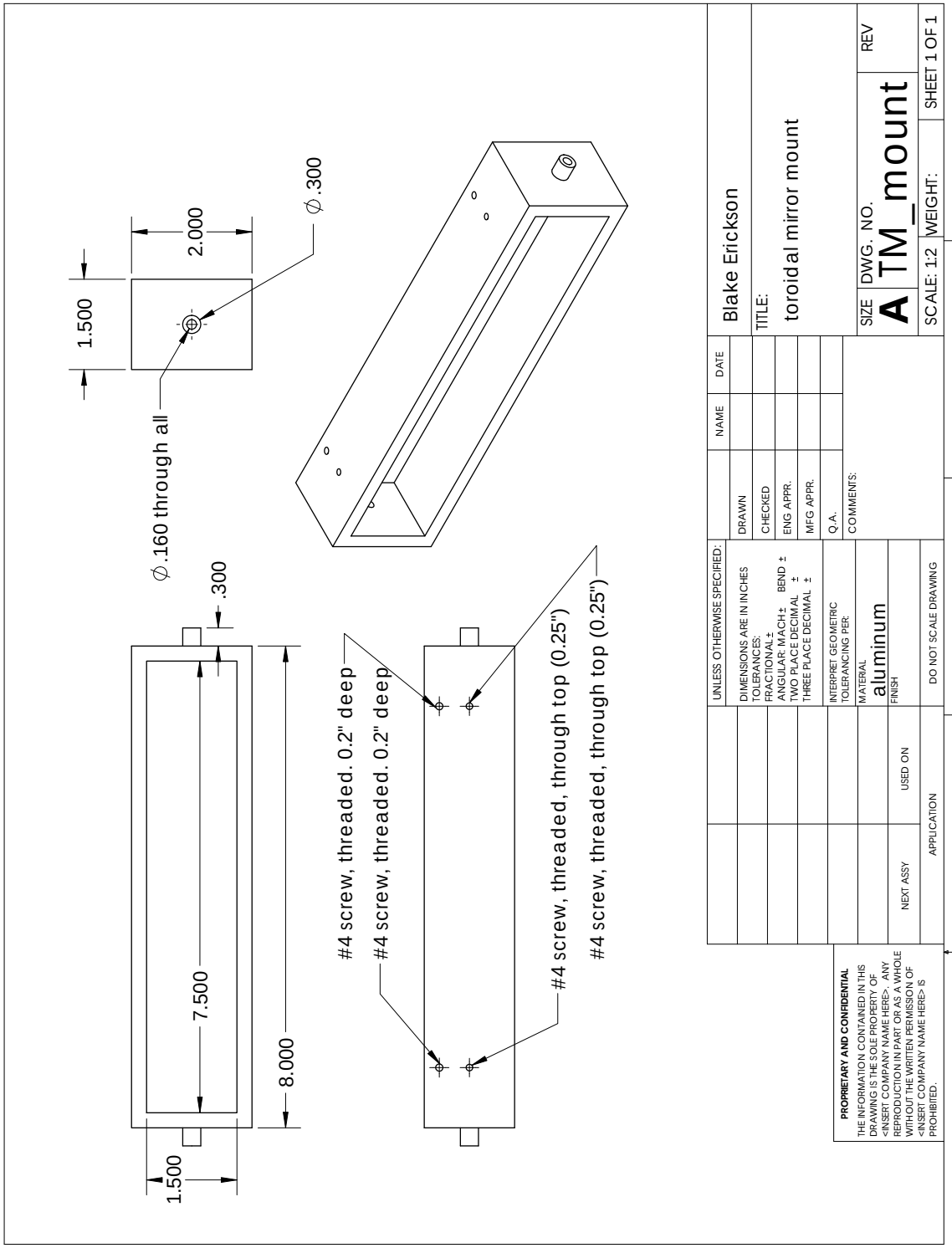

Figure B.6: The mount used to hold the toroidal mirror.

Appendix C

List of Publications

1. H.L. Williams, **B.A. Erickson**, D.M. Neumark. Time-resolved photoelectron spectroscopy of adenosine and adenosine monophosphate photodeactivation mechanisms in water microjets. *J. Chem. Phys.* 148, 194303 (2018).

2. **B.A. Erickson**, Z.N. Heim, E. Pieri, E. Liu, T.J. Martinez, D.M. Neumark. Relaxation Dynamics of Hydrated Thymine, Thymidine, and Thymidine Monophosphate Probed by Liquid Jet Time-Resolved Photoelectron Spectroscopy. *J. Phys. Chem. A* 123, 10676 (2019).

3. C.J Easley*, **B.A. Erickson***, K.M. Hunter*. Viewpoints on the 2020 Pacific Conference on Spectroscopy and Dynamics. *J. Phys. Chem. A* 124, 2731 (2020).
   * = authors contributed equally to this work

Appendix D

List of Abbreviations

- ADC - Analog-to-Digital Converter
- Ado - Adenosine
- AMP - Adenosine-5'-Monophosphate
- BBO - β-Barium Borate
- CASSCF - Complete Active Space Self Consistent Field
- CF - ConFlat®
- CI - Conical Intersection
- CMOS - Complementary Metal-Oxide-Semiconductor
- CTTS - Charge Transfer to Solvent
- DAS - Decay Associated Spectrum
- DC - Direct Current
- DNA - Deoxyribonucleic Acid
- eBE - Electron Binding Energy
- eKE - Electron Kinetic Energy
- eV - Electron Volt
- FU - Fluorescence Upconversion
- FWHM - Full width at half maximum
- GLA - Global Lifetime Analysis

- HHG - High Harmonic Generation
- HOMO - Highest Occupied Molecular Orbital
- HPLC - High Performance Liquid Chromatography
- IR - Infrared
- IRF - Instrument Response Function
- LAPE - Laser-Assisted Photoelectric Effect
- LBNL - Lawrence Berkeley National Labs
- LMCT - Ligand-to-Metal Charge-Transfer
- LPES - Liquid Microjet Photoelectron Spectroscopy
- LUMO - Lowest Unoccupied Molecular Orbital
- MCP - Microchannel Plate
- MO - Metanil Orange
- MPI - Multiphoton Ionization
- MY - Metanil Yellow
- NA - Nucleic Acid
- NB - Nucleobase
- OPA - Optical Parametric Amplifier
- PCM - Polarizable Continuum Model
- PES - Potential Energy Surface
- QM/MM - Quantum Mechanics/Molecular Mechanics
- QY - Quinoline Yellow
- RNA - Ribonucleic Acid
- SFG - Sum Frequency Generation
- SHG - Second Harmonic Generation
- SIGC - Semi-Infinite Gas Cell

- T - Thymine
- TA - Transient Absorption
- TMP - Thymidine-5'-Monophosphate
- TOPAS - Traveling-Wave Optical Parametric Amplification System
- TRPES - Time-Resolved Photoelectron Spectroscopy
- Thd - Thymidine
- Ti:Sapph - Titanium Sapphire
- ToF - Time-of-Flight
- TpT - Thymidine-Phosphate-Thymidine Dimer
- UV - Ultraviolet
- UVVIS - Ultraviolet/Visible
- VDE - Vertical Detachment Energy
- XUV - Extreme Ultraviolet

Appendix E

Code for Data Acquisition and Data Analysis

All of our data acquisition code is written in LabView. As mentioned in Chapter 2, a lot of the source code was lost at some point so it was rewritten. This new code was designed to work on our new ADC card rather than the oscilloscope used in the past theses. Static programs were also written with the help of Acqiris's prewritten code. Below I give the most up to date versions of each program.

The post processing code, written in MATLAB, used in the prior two theses is still largely relevant, but some major changes have been made to facilitate the switch to our new XUV probe. Although a lot of it is still the same, the complete working code is replicated for ease of use.

E.1 Static Data Acquisition Code

This section describes four different data collection processes used in LPES: Averager, Single Shot, Threshold, and Peak Detection. Each program has two variants: one which only displays the data and one that displays and prompts the user to save the data. The front panels and a brief description of each method of data collection is given below. Current file names are presented as well, but those will almost certainly change over time.

Averager

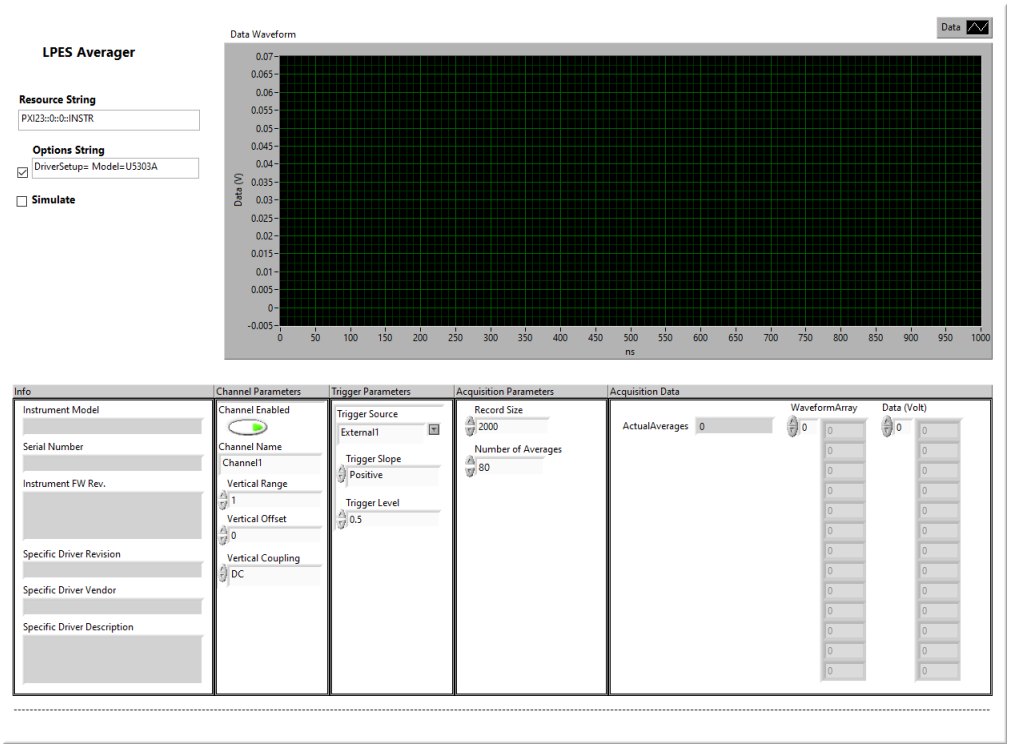

Figure E.1: Front panel for the static averager code. Current code file names: "Averager_LPES" and "Averager_LPES_save"

The first and most often used program is the averager. This code averages a set number of shots ("Number of Averages" on the front panel) over a set number of points (Record Size on the front panel). The points are 0.5 ns each, so the maximum ToF measured is half of this value. This data is saved as two columns. The first column is the ToF (in 0.5 ns intervals) and the second column is the averaged data.

Single Shot

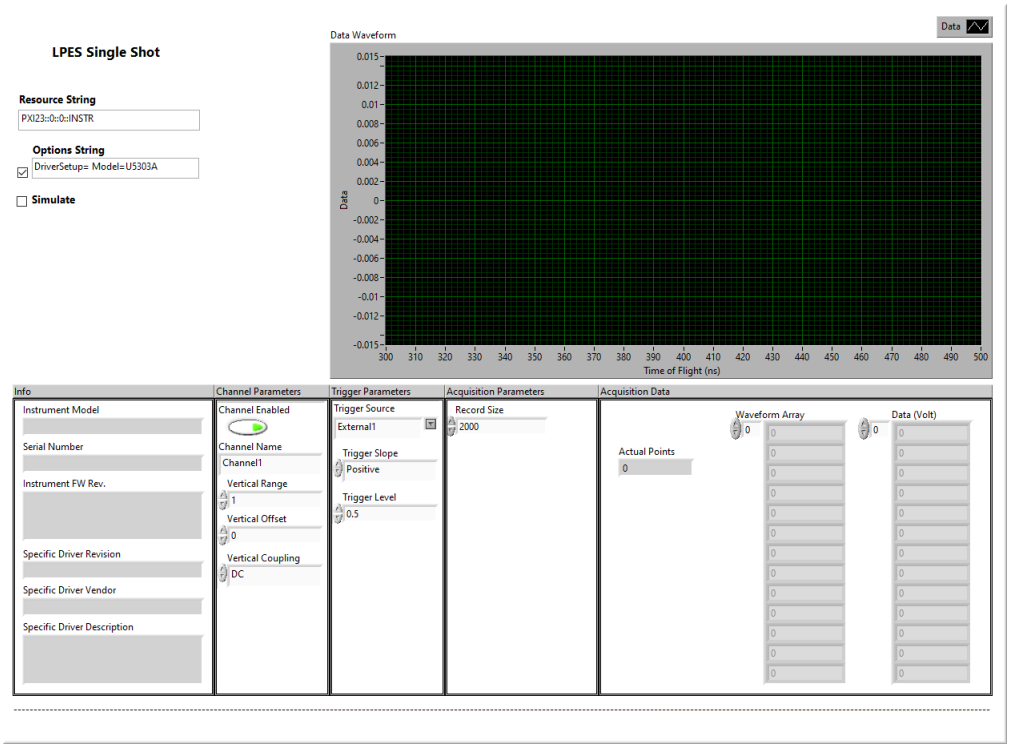

Figure E.2: Front panel for the static single shot code. Current code file names: "SingleShot_LPES" and "SingleShot_LPES_save"

The second program is used to take a single shot spectrum. This program operates the same way as the averager code except only takes one shot and displays it.

Threshold

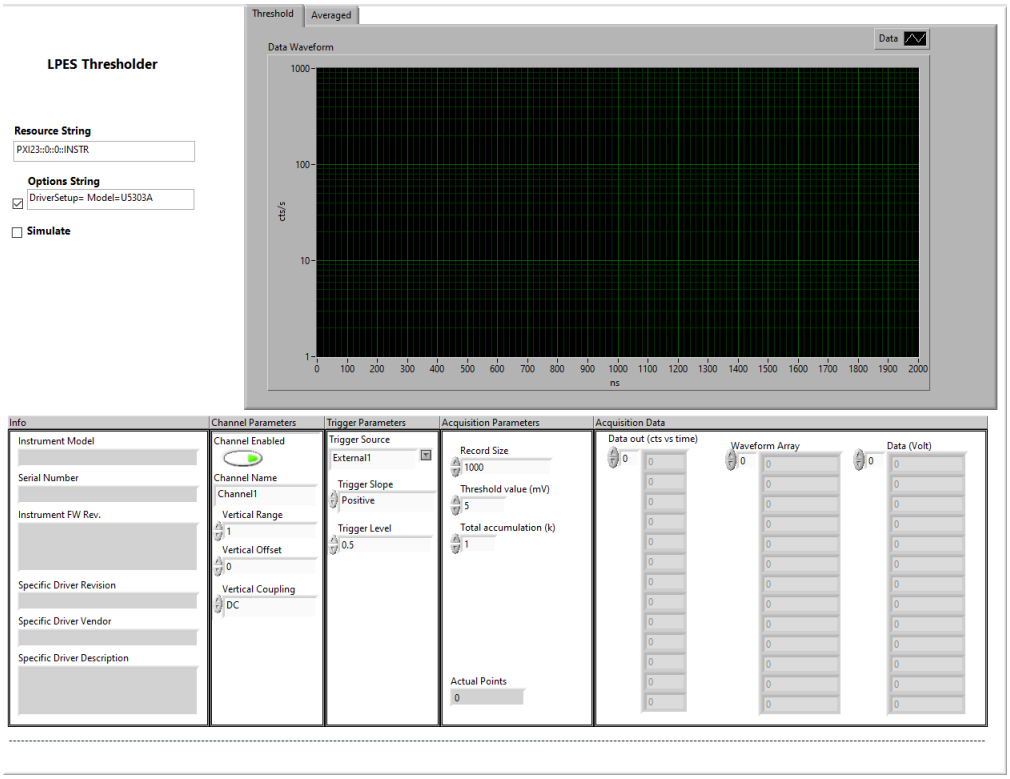

Figure E.3: Front panel for the static thresholding code. Current code file names: "Threshold_LPES" and "Threshold_LPES_save"

The third program is the thresholder. This program takes single shot spectrum and then converts any time bins above a set value (Threshold Value on the front panel) to 1 and every other bin to 0. It does this process over many shots (Total accumulation (k) on the front panel) and sums them together. This code simultaneously takes the single shot output and averages it, functionally acting as both an event counter and an averager. This data is saved in three columns. The first column is the ToF (in 0.5 ns intervals), the second column is the thresholded sum, and the third column is the averaged data. This program is especially useful when trying to measure events that are rare, i.e. each laser shot produces $0 - 1$ event in that kinetic energy range.

Peak Detection

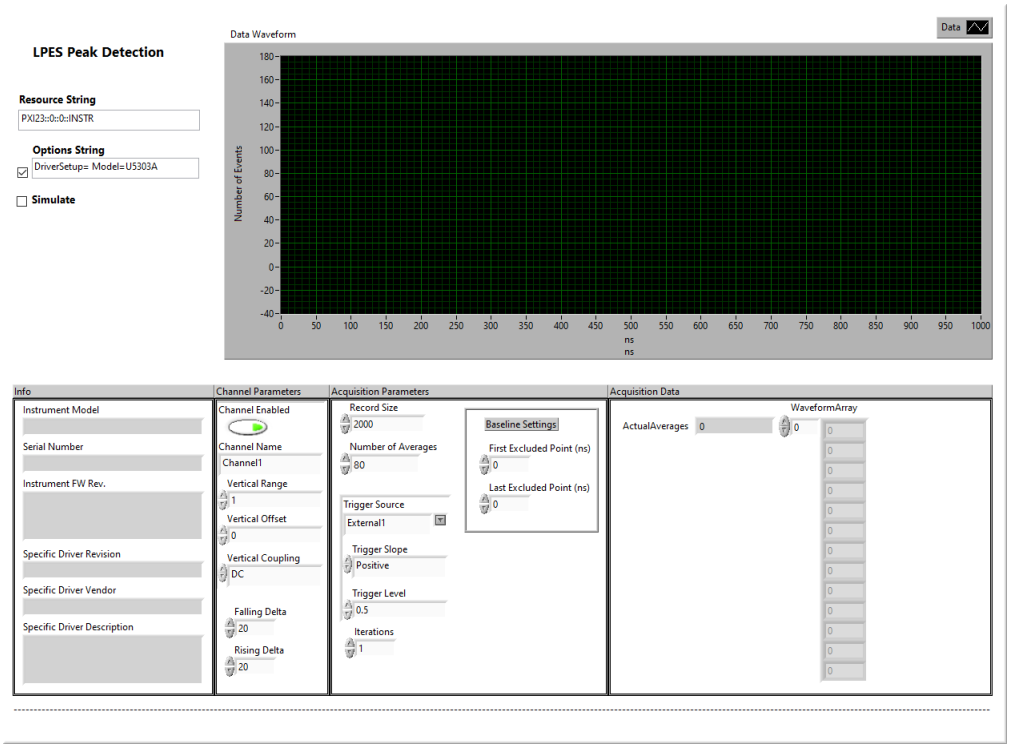

Figure E.4: Front panel for the static peak detection code. Current code file names: "PeakDetection_LPES_v2" and "PeakDetection_LPES_save_v2"

The final static program used is the peak detector. This program works by taking an averaged spectrum and then trying to fit individual peaks in that spectrum. The width of the fitted peak can be controlled by changing the "Rising Delta" and "Falling Delta" options on the front panel. When the width of the peaks gets relatively small, an artificial background appears in the data. This can be offset by using the "Baseline Settings" box. This works by averaging a portion of the data that is expected to be free of signal and subtracting it from the rest of the data before displaying it.

E.2 Time-Resolved Programs

Three time-resolved programs are used in LPES, each corresponding to the static programs listed above (with the exception of the Single Shot mode). These programs work as described in the thesis of Madeline Elkins, featured nested while loops that collect data at various stage delays. All of these codes have the same basic structure, but a few changes have been made.

1. The stage delays have now been automatically randomized. This ensures that drifting in the overall signal intensity doesn't cause the appearance of time-dependent signal.

2. Backgrounds can now be taken at every stage delay for either or both of the two pulses used in the experiment. Additionally, a timer is now built in to delay data collection after a background scan to allow the signal to stabilize. This is especially important after blocking the XUV line as it takes up to 5 seconds for the harmonic intensity to stabilize.

3. The total intensity averager has been removed. This was not present in the starting code after the data loss and was not rewritten as the randomized stage delays rendered it useless.

The current version of the time-resolved averager code is shown in Figure E.5. This code is visually the same as the threshold and peak detection code, so those are not reproduced here.

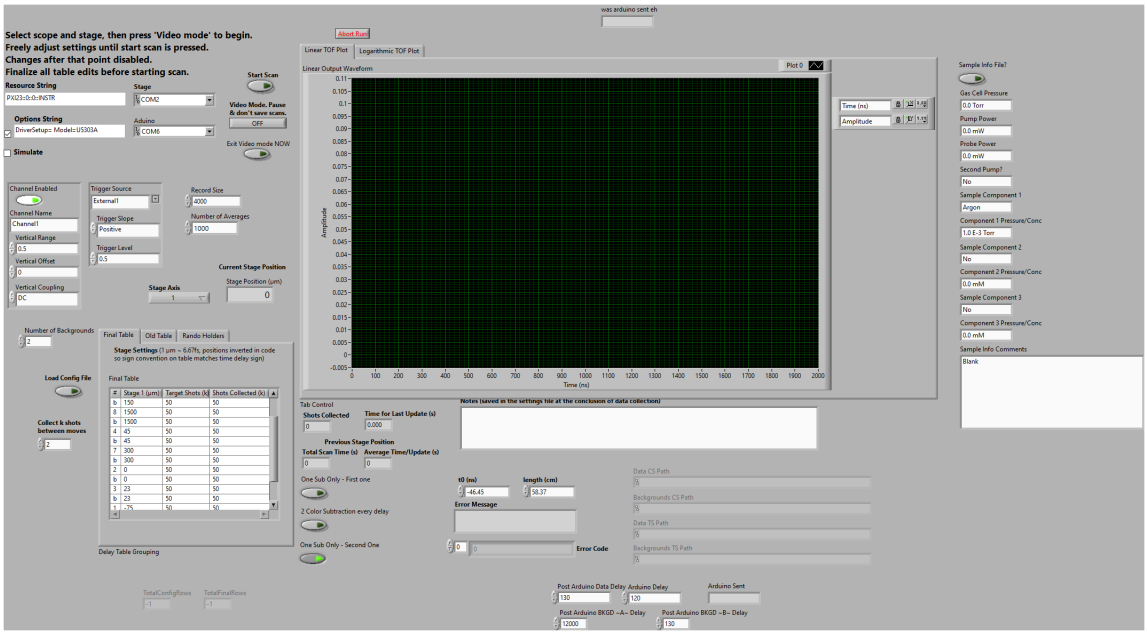

Figure E.5: Front panel for the time-resolved averager code. Current code file name: "LPES_alpha08.5_AVG"

The current versions of the code are:

- Averager: LPES_alpha08.5_AVG
- Threshold: LPES_alpha08.5_THR

- Peak Detection: LPES_alpha08.5_PKD

E.3 Post Processing Matlab Code

This code is largely the same as what is found in the thesis of Madeline Elkins, but several changes were made. This code is presented in completeness for ease of use. The major changes made to the code are listed below.

1. This code now allows for the input of backgrounds taken at every delay for 0, 1, or 2 beams and differentiates between them automatically (see lines 56 – 89).
2. This code produces a TRPES matrix which is the tTRPES matrix subtracted from the most negative delay point (see lines 169 – 172).
3. This code now allows the viewing of larger kinetic energies which is important when working with our new XUV source. To change the energy range, change the number in lines 165 and 167 from "422" to a different number.
4. The binning into 10 ns bins has been commented out (see lines 149 – 156). This has been done to prevent averaging out high kinetic energy features that are narrow in ToF space.

```
1  %post processor - faster KE, 2 ns binning
2
3  %directions:
4  %MUST CHANGE # OF BACKGROUND SCANS BASED ON TYPE OF DATA
5  %You will be asked which delay scan number should be used to find a ...
       flat base line
6  %You will be asked which region is non-flat in that delay
7
8  %% set-up, import
9  tau=[125,400];
10 IRFFWHM=100;
11 fig=1;
12 numbkgd = 2;
13
14 t0=-16;
15 len=66;
16
17 ekeEfile='CombinedSums_Data.csv';
18 backgroundfile='CombinedSums_BKGD.csv';
19 configfile='ConfigTable.csv';
20
21 datmat=csvread(ekeEfile,1,0);
```

```
22 datmatl=datmat(2:end,:);
23 datorder=datmat(1,:);
24 backmatl=csvread(backgroundfile,1,0);
25
26 numeKE=length(datmatl);
27 backmatsize=min(size(backmatl));
28 numdelays=size(datmatl,2);
29 %delayorder=csvread(ekeEfile,1,1,40,1);
30
31 %deletes all background scans from confmat
32 confmat=readmatrix(configfile);
33 for l=length(confmat):-1:1
34     if isnan(confmat(l,1))
35         confmat(l,:)=[];
36     end
37 end
38
39 binstof = linspace(0.5, 2000, 4000);
40
41 %create column of eKE values
42 E=284.3174 .*(len^2./(binstof-t0).^2);
43 eeKE=E';
44
45 %create delays matrix
46 sortconfmat=sort(confmat);
47 delays=(20/3*sortconfmat(1:numdelays,2))';
48
49 %generate weights for jacobian transformation
50 datE=zeros(4000,numdelays);
51 dataE=zeros(4000,numdelays);
52
53 escale=eeKE.^(3/2);
54
55 %% Background subtraction - different cases for different methods of ...
       bkgd subtraction
56
57 %delay dependent bkgd for one beam, but not the other
58 if min(size(datmatl)) == min(size(backmatl)) - 1
59     bkgd=zeros(numeKE,numdelays);
60     bkgd=backmatl(:,1:numdelays);
61     bkgdsingle = backmatl(:,numdelays+1);
62     Bkgd=[];
63     for l=1:numdelays
64         Bkgd=[Bkgd,bkgd(:,l)+bkgdsingle];
65     end
66 end
67
68 %delay dependent bkgd for both beams
69 if 2*min(size(datmatl)) == min(size(backmatl))
70     bkgd=zeros(numeKE,numdelays);
```

```
71      bkgd1=backmatl(:,1:2:end);
72      bkgd2=backmatl(:,2:2:end);
73      bkgdtot = bkgd1 + bkgd2;
74      Bkgd=bkgdtot;
75  end
76
77  %no delay dependent bkgd scans
78  if min(size(backmatl)) == numbkgd
79      bkgd=zeros(numeKE,1);
80      for r=1:numbkgd
81          bkgd=datmatl(:,numdelays+r)+bkgd;
82      end
83
84      Bkgd=[];
85      for l=1:numdelays
86          Bkgd=[Bkgd,bkgd];
87      end
88  end
89
90  %subd=datmatl;
91  subdpre=datmatl(:,1:numdelays)-Bkgd;
92
93  subdconc=[datorder;subdpre];
94
95  subdconcT=transpose(subdconc);
96  subdconcTsorted=sortrows(subdconcT);
97  subdsorted=transpose(subdconcTsorted);
98
99  subd=subdsorted(2:end,:);
100
101 %% Baseline Flattening
102 %user select delay for eKE lane
103 prompt = 'Enter number of delay to use for baseline correction';
104 lanes=inputdlg(prompt);
105 lane=str2double(lanes);
106
107 eKElane=subd(:,lane);
108
109 figure(20000135)
110
111 plot(binstof,eKElane)
112
113 excludes = inputdlg({'start ToF range to exlcude','end Tof range to ...
        exclude'},'Info');
114 vals1=excludes{1};
115 val1=str2double(vals1);
116 vals2=excludes{2};
117 val2=str2double(vals2);
118 exclude=(2*val1:1:2*val2);
119
```

```
b=-.004;

[xData, yData] = prepareCurveData( binstof, eKElane' );

% Set up fittype and options.
ft = fittype( 'linefit(x,b)', 'independent', 'x', 'dependent', 'y' );
excludedPoints = excludedata( xData, yData, 'Indices', exclude);
opts = fitoptions( 'Method', 'NonlinearLeastSquares' );
opts.Display = 'Off';
opts.StartPoint = b;
opts.Exclude = excludedPoints;

% Fit model to data.
[fitresult, gof] = fit( xData, yData, ft, opts );

fitresult

bs = coeffvalues(fitresult);
dataavg=subd-bs;

%% Jacobian Transformation

for n=1:numdelays
    dataE(:,n)= dataavg(:,n)./escale;
end

datmat=dataE;

%% Rebin to 10ns tof lanes

%rusbd=[];
%for l = 1: numdelays;
%    for n = 1: numeKE/5
%            rsubd(n,l) = datmat(5*n,l) + datmat(5*n-1,l) + ...
   datmat(5*n-2,l)+ datmat(5*n-3,l) + datmat(5*n-4,l);
%    end
%end

%% Write Mat File
%create column of eKE values
nE=284.3174 .*(len^2./(binstof-t0).^2);
neKE=nE';

newnumeKE=length(datmat);

eKE=flipud(neKE(422:2000));
ldelay=length(delays);
tTRPES=flipud(datmat(422:2000,1:ldelay));

TR1=tTRPES(:,1);
```

```
169 REP=repmat(TR1,1);
170 base=REP([1:length(TR1)],:);
171 TRPES=tTRPES-base;
172
173 filenamefitmat='BkgdBaselineJacScaleRebin.mat';
174 save(filenamefitmat,'IRFFWHM','tau','fig','delays','eKE','tTRPES');
```